The Pennsylvania State University

The Graduate School

Department of Geosciences

OBSERVATION AND ANALYSIS OF REPEATING EARTHQUAKES BENEATH THE ACEH BASIN, NORTHERN SUMATRA

A Thesis in

Geosciences

by

Sarah Anne Barrett

Submitted in Partial Fulfillment
of the Requirements
for the Degree of

Master of Science

August 2010

The thesis of Sarah Anne Barrett was reviewed and approved* by the following:

Charles Ammon
Professor of Geosciences
Thesis Advisor

Kevin Furlong
Professor of Geosciences

Chris Marone
Professor of Geosciences

Katherine Freeman
Professor of Geosciences
Associate Department Head of Geosciences Graduate Program

*Signatures are on file in the Graduate School

ABSTRACT

Repeating earthquakes are observed across a variety of tectonic settings. In this study we discuss observations of numerous repeating earthquakes that occurred beneath the Aceh Basin following The Great 2004 Sumatra-Andaman Earthquake. The Aceh Basin is the northernmost in a series of forearc basins located along the Sunda Trench (~94° E, 5° N). The plate boundary beneath the basin was relatively aseismic prior to the 2004 megathrust earthquake. An analysis of the moderate-size earthquakes occurring beneath the Aceh Basin in response to the 2004 megathrust provides interesting and important observations of stick-slip faulting near the deep within the seismogenic zone. We use teleseismic and distant regional observations to identify repeating earthquakes that we infer to be located along the plate boundary 30-50 km beneath the seafloor. Analysis of the short-period coda following teleseismic and regional P and regional S waves is used to estimate the distance between repeating events in the same sequence. The coda analysis indicates that in most instances the same asperity is failing in the sequence of repeating events. Despite incredibly consistent coda coherence, events within each sequence show resolvable amplitude differences, which suggest changes in frictional strength occurring throughout the duration of the repeating earthquake sequence. This rapid change (over a few seismic cycles) in strength may be a function of the erosion of the asperity or a change in intrinsic strength. Additional studies of large aftershock sequences, such as the 2010 Chile earthquake, may provide more insight into these questions.

TABLE OF CONTENTS

LIST OF FIGURES

.

LIST OF TABLES

ACKNOWLEDGEMENTS

I would like to thank my advisor, Dr. Charles Ammon, for his insight and contributions to my research, this thesis and my career. I would also like to thank the members of my committee, Dr. Kevin Furlong and Dr. Chris Marone for their guidance and contributions to this thesis. Without the assistance of my committee, this work would not exist.

I thank the staff at IRIS for archiving and maintaining the seismic data used in this study. I also acknowledge the use of data from seismic station PSI (Prapat, Indonesia) of the PACIFIC21 seismic network, operated by the University of Tokyo, Japan. I also thank Tom Owens and Philip Crotwell for their work on the data access client SOD, and P. Wessel and W.H.F. Smith for the GMT package that was used to prepare the maps in this work. I also used SAC, developed at Lawrence Livermore National Laboratory, to complete some of the seismogram analysis.

This thesis was completed under the intent to submit to a peer-reviewed publication. As a result, my advisor, Dr. Charles Ammon, contributed to this work and will be a co-author of that publication.

I would like to express gratitude to the members of the Penn State faculty who encouraged me to pursue a higher degree as well as to my peers for their constant encouragement. I also thank my family, my siblings, and especially my parents for being my “Bridge Over Troubled Water.”

Chapter 1

Introduction

Repeating earthquakes are observed across a variety of tectonic settings (e.g. Nadeau and Johnson, 1998; Igarishi et al., 2003; Kimura et al., 2006). In this study we discuss our observations of repeating earthquakes that occurred beneath the Aceh Basin following The Great 2004 Sumatra-Andaman Earthquake. The Aceh Basin is the northernmost in a series of forearc basins located along the Sunda Trench. The megathrust beneath the basin (Figure 1-1) was relatively aseismic prior to the 2004 megathrust earthquake. An analysis of the moderate-size earthquakes occurring beneath the Aceh Basin in response to the 2004 earthquake provides interesting and important observations of stick-slip faulting near the deep within the seismogenic zone. In this section we review earlier observations of repeating earthquakes, describe the tectonic setting and review the seismicity of the Sunda Trench and Aceh Basin.

Observations of Repeating Earthquakes

Repeating earthquakes have been observed and studied within many fault systems such as the San Andreas Fault (Nadeau and Johnson, 1998) as well as along the subduction plate boundary off the coast of Japan (Igarashi et al., 2003; Kimura et al., 2006). Historically, the idea of repeating events is derived from the elastic rebound theory of Reid (1910) and time predictable earthquake modes such as that of Shimasaki and Nakata (1980). Repeating events (REs) are the recurrence of slip on the same seismic asperity and have been identified using seismograms or spectra using the assumption each event produces nearly identical seismic wavefields, including primary seismic phases and coda. For the purposes of this study, we define asperities as regions

capable of seismic event nucleation and seismic slip, surrounded by regions experiencing aseismic creep. Most examples of repeating events are small (M_w >~3) although a number of similar events have been observed near Parkfield (Bakun and McEvilly, 1984), and some moderate-size repeaters have been observed off the coast of Japan (Igarashi et al., 2003).

Nadeau and Johnson (1998) discussed clusters of 3 to 13 microseismic events with similar focal mechanisms and seismograms observed near Parkfield, CA. The authors identified similar events using a cross correlation technique. The Parkfield repeaters are ±0.1 magnitude units different and occur quasi-periodically (Nadeau and Johnson, 1998). Peng et al. (2005) studied repeating earthquakes in the Calaveras fault system following the 1984 Mw 6.2 Morgan Hill earthquake and identified an intriguing relationship between recurrence interval between repeating aftershocks and their relative moment.

Widely accepted views of fault friction include a presumption that stick-slip regions of the fault (asperities) strengthen with increasing hold time (Marone, 1998). A stronger contact can support and eventually release more strain energy than a weaker contact. Peng et al. (2005) observed many events that fit this usual pattern. However, they also observed a number of repeating earthquake sequences that suggested an increase in fault strength following the first event. They speculated that the increase in strain rate following the mainshock may have strengthened the faults through a process known as transient embrittlement.

Igarashi et al. (2003) observed numerous repeating events (M~4.5) off the coast of Japan, along the boundary with the subducting Pacific plate. The authors identified two varieties of repeaters that they called continuous and burst type repeaters. Continuous type repeating events occur at regular intervals with focal mechanisms indicative of the plate boundary geometry. They used these events to infer plate motion rates. The strain release associated with these events is produced steadily by asesimic motion at the plate motion rate in the region surrounding the repeater. Burst type repeating events occur sporadically and are attributed to be swarms or

aftershocks (Igarashi et al., 2003). These events can vary in focal mechanism and are generally inconsistent with the plate boundary geometry. Burst types of event are expanded upon by Kimura et al. (2006), and hypothesized to occur on pre-existing fault planes.

Kimura et al. (2006), observe repeating earthquakes associated with the subduction of the Philippine Sea Plate beneath central Japan. The authors show the majority of the events occur with regular recurrence intervals (continuous type repeaters) that occur in the plate boundary region. They used these events to establish the subducting plate geometry and plate velocity. The slip continuous-type repeating events accounts for 25-126% of the observed GPS motion (Kimura et al., 2006). This apparent slip-rate discrepancy was resolved by Sagiya (2004) to be less than 10 mm/yr difference for more recent years (1996-2000) and within the margin of error for both GPS and seismic slip determination methods.

Tectonic Setting of the Aceh Basin Region

Although subduction in the Indonesian region has occurred since the Permian, the present geometry probably did not form until the Mesozoic. Subduction along the Sunda trench is thought to have initiated either during the Triassic-Jurassic, 251-150 Ma (Katili, 1975) or the early Cretaceous, 146-112 Ma, (Scotese et al., 1988). Peak subduction rates were reached in the Paleocene (66-59 Ma), ~150 mm/yr (Molnar and Tapponnier, 1975) but slowed significantly (~30 mm/yr), as a consequence of renewed extension in the Indian Ocean. The current convergence rate (~60±10 mm/yr; DeMets, 1990) was in place by the Oligocene (34-28 Ma). The current trench geometry is thought to have formed during the Miocene (23-7 Ma), possibly as late as the Pleistocene, ~2-1 Ma, (Susilohad et al., 2005). Presently, Eocene aged (50-60 Ma) lithosphere subducts at the trench in the region of Northern Sumatra (Cande and Kent, 1995). The subducting lithosphere dips ~10-12° and steepens to approximately ~15-20° beneath the forearc (Araki et al.,

2006). The volcanism in region is intermediate to silicic, suggesting the interaction of the subducting plate late with thicker, older continental lithosphere of primarily island arc material (Katili, 1973).

The convergence of the Indo-Australian plate with the Eurasian plate governs the tectonics of the Indonesian region (Figure 1-2). Relative to the Eurasian plate, the Indo-Australian plate advances 50-70 mm/yr NNE (NUEVEL-1A; DeMets et al., 1994). Plate-motion models that include a separate Sunda block (e.g. Bock et al., 2003; Socquet et al., 2006) or additional separate Capricorn plate (DeMets et al., 2010) do not substantially change the convergence rate between the two plates (less than ~10 mm/yr). The plate convergence is substantially oblique to the trend of the trench north of 3°N. In northern Sumatra, the convergence accommodated on the trench is ~50 mm/yr (Vita-Finzi, 2007); the trench parallel (shear) component manifests as the Sumatra Fault System, a group of dextral transform faults. Currently, the most active is the Great Sumatran fault which runs the length of Sumatra and accounts for ~20 mm/yr (Vita-Finzi, 2007). In the northernmost region, subduction processes are more strongly affected by the large influx of sediments in the Bay of Bengal (Engdahl, et al., 2007). A chain of forearc basins spans the length of the arc from Java to northern Sumatra, the Aceh Basin (Figure 1-2) is the northernmost.

The Aceh Basin is located about 13 km off the coast of northern Sumatra and about 150 km from the trench. The 20,000 km^2 basin is bounded in the west by the West Andaman fault, an active dextral northern splay of the Mentawai fault (Seeber et al., 2007). The Aceh Basin is the deepest of the forearc basins with a water depth of 2.7 km (Seeber et al., 2007). The timing of basin sediment filling is unknown, however, forearc basins further south are thought to have accumulated sediments during the Pleistocene (Berglar et al., 2008). The seismic structure of the upper kilometer of basin sediments is well resolved and shows relatively flat lying sediments (Mosher et al., 2008). Barrett (2009) modeled teleseismic body wave depth phases from earthquakes beneath the basin and found that the basin was underlain by a thick sequence of slow

sediments. Matching the depth-phase observations also required a strong contrast at the basin's base.

Seismicity of the Sunda Trench Region

In the last 250 years four earthquakes larger than magnitude eight have struck the Sunda region: 1797 (M~8.4), 1833 (M~9), 1861 (M~8.5), and 2004 (M 9.2) (Lay et al., 2005). The earliest three events occurred prior to the development of sophisticated geophysical instrumentation. The majority of information on the 1979, 1833, and 1861 earthquakes is based on the historic and seismologic estimates of their rupture areas (Billham et al., 2005). Earlier events have been identified from coral-based geodetic observations (e.g. Sieh et al., 2008; Natawidjaja, et al., 2006). Sieh et al., (2008) analyzed shallow-water microatolls to estimate the long term seismic history for the Sunda trench region. The corals provide a 700-year history of the region, including nine additional large earthquakes in the Mentawai segment alone (approximately 900 km southeast of the Aceh Basin). In that region, a 200-year seismic cycle culminates with a large rupture followed by observed rapid sea level fall on the order of 100-200 cm (Sieh et al., 2008).

The megathrust event on 26 December 2004 (M_w 9.2) was one of the largest earthquakes in recorded human history; the resulting tsunami devastated the region (Bilek, et al., 2007). The mainshock initiated at 3.3°N, 96.0°E (Figure 1-2) at a depth of 30 km, at 00:58:53 GMT (Lay, et al., 2005). The total rupture is estimated to be as long as 1600 km and last over 600 seconds in duration (Bilek, et al., 2007). The rupture propagated northward at about 2.5 km/s with strong releases of energy at latitudes near 2-4°N, 8-10°N, and 12-13.75°N (Ammon, et al., 2005). These loci of strong seismic energy release are interpreted to be the "failure of relatively strong section[s] of the megathrust," (Ammon, et al., 2005). The plate boundary beneath the Aceh Basin

slipped in large amounts during the 2004 rupture. We show slip estimates from Chlieh et al. (2007) in Figure 1-3; the boundary beneath the Aceh Basin likely experienced more than 15 m of coseismic slip.

The Great 2004 Sumatra-Andaman event provided insight into the mechanics of large earthquakes in subduction zones, and also raised some questions about what we know of the seismogenic potential of subduction zones (Lay et al., 2004; Subarya et al., 2006). The 2004 earthquake aftershock sequence is comprised of many thousands of events along and adjacent to the segment(s) that failed during the earthquake. The most significant of the thousands of aftershocks is the 29 March 2005 (M_w 8.6) Nias-Simeulue earthquake (e.g. Engdahl et al., 2007). Konca et al. (2007) suggest that the Nias event, located just south of the 2004 rupture, included large slip on two asperities (one beneath Nias, the other beneath Simeulue) divided by a geologic feature in the forearc. Part of the Mentawai region failed on 12 September 2007 in a pair of earthquakes, an M_w 8.5 near the southern edge of the 1833 rupture, and a M_w 7.9 aftershock nucleated farther north. This pair of events released only a portion of the accumulated strain; a portion of the locked fault patch still may be capable of 4-7 m of slip (Megawati and Pan, 2009).

The recent pre-2004 seismicity rate of the Aceh Basin (Figure 1-1) was lower than at present. Using seismicity data starting in the early 1970s, we estimate a pre-2004 seismicity rate of about one moderate-sized event ($M_w < 5$) per year. Although the numbers are few, events prior to 2004 appear to occur in different locations beneath the Aceh Basin than post 2004 events, in a roughly even distribution around the basin perimeter. Aftershocks beneath the Aceh Basin have been numerous; however, this study is primarily concerned with those $\sim m_b \geq 4.5$. These aftershocks have followed a characteristic Omori-Law decay, decreasing in frequency hyperbolically with time since the mainshock (Figure 1-4a). The magnitude distribution of the events shows an approximate Gutenberg-Richter distribution (Figure 1-4b), albeit with a rather large negative slope (~1.9) across the magnitude range of 4.5 to 6.0. Events smaller than M 4.5

and those larger than M 6 were not included in the linear fit due to uncertainty associated with catalog completeness outside the moderate-size range.

Although we examine events both before and following the 2004 earthquake, our emphasis is on the post-megathrust activity. The Aceh Basin expressed a great increase in seismicity following the mainshock, producing more than one hundred moderate-size earthquakes that predominantly show low-angle thrust fault geometries (Figure 1-1; Appendix A). Our particular focus is on clusters of repeating, or very closely co-located, earthquakes that make up about 20% of the sub-basin activity. We analyze these events under the assumption that they are created when isolated stick-slip regions surrounded by aseismically deforming regions are loaded to the point of failure.

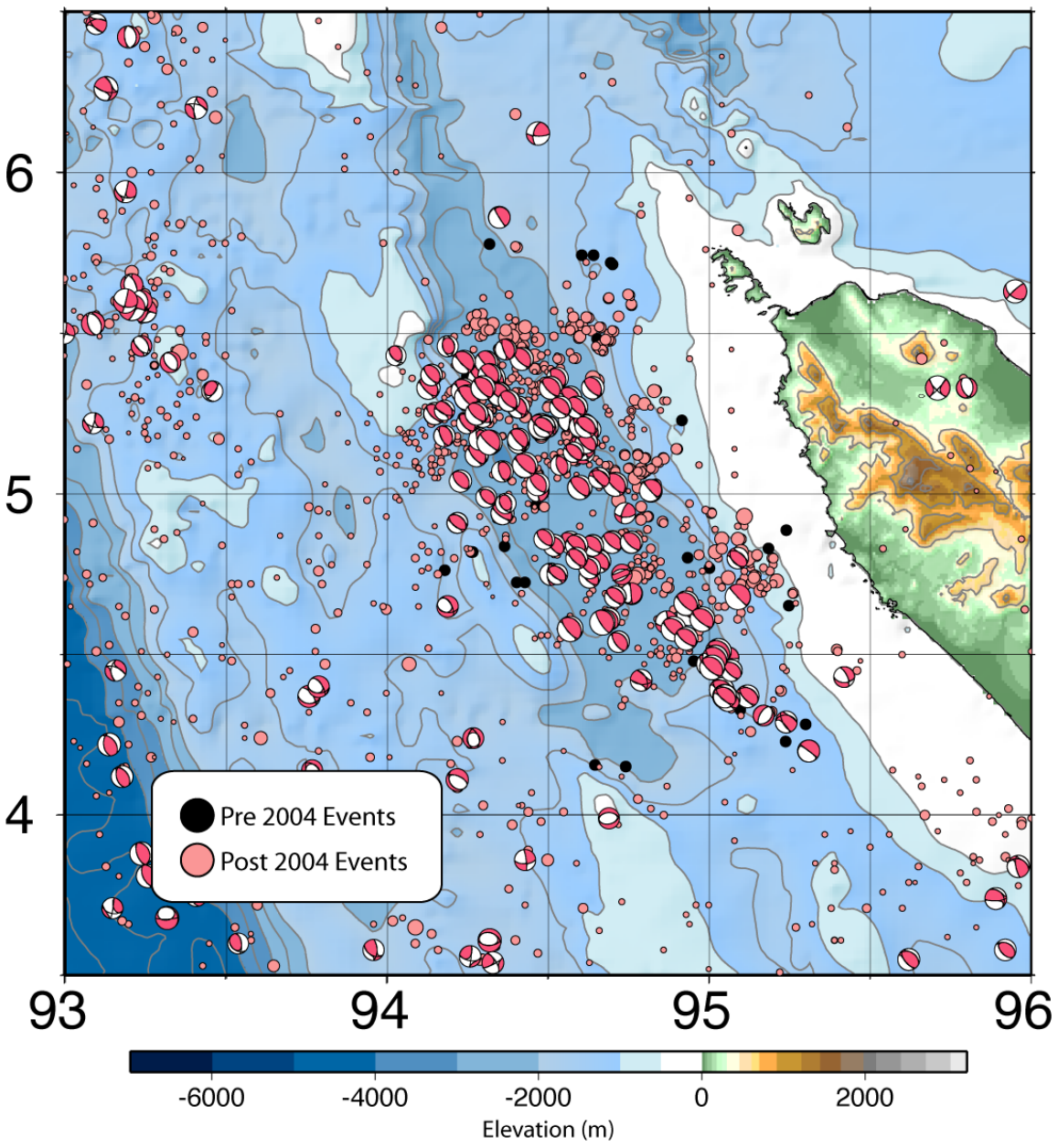

Figure **1-1**: The seismicity of the Aceh Basin. Events use the NEIC locations, those prior to 2004 are plotted in black, those since (aftershocks) are in red. GCMT locations are used to plot centroids for moderate sized aftershocks.

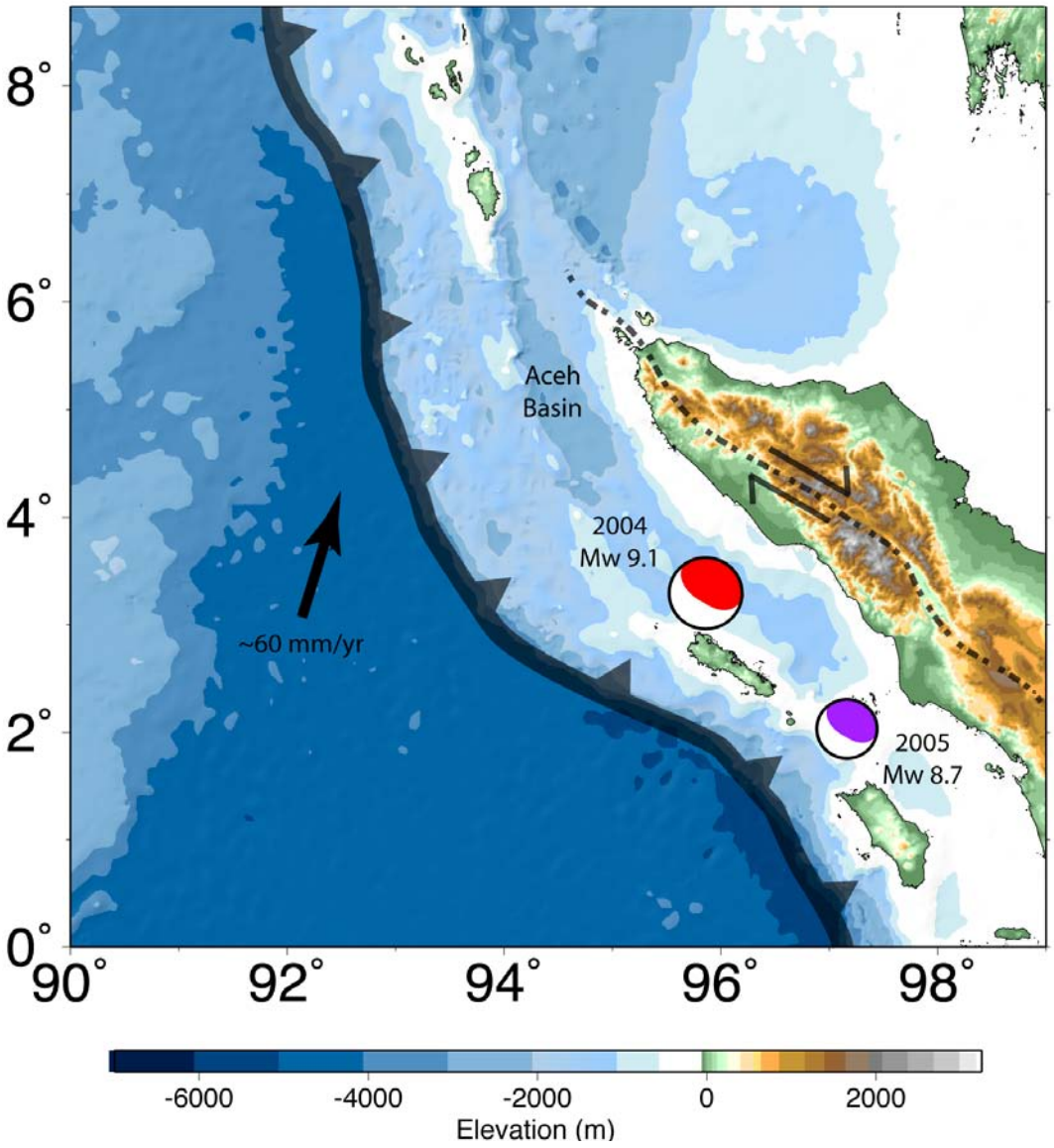

Figure **1-2**: The tectonic setting in the Sunda Trench Region. The Indo-Australian plate subducts at the Sunda trench (solid line), while the rest of the convergence is accommodated on the Great Sumatra Fault (dashed line), a right-lateral strike slip fault. The GCMT focal mechanism for the 2004 Great Sumatra Andaman earthquake (M_w 9.1, red) and 2005 (M_w 8.7, violet) are plotted at their EHB epicenters (centroid locations differ slightly).

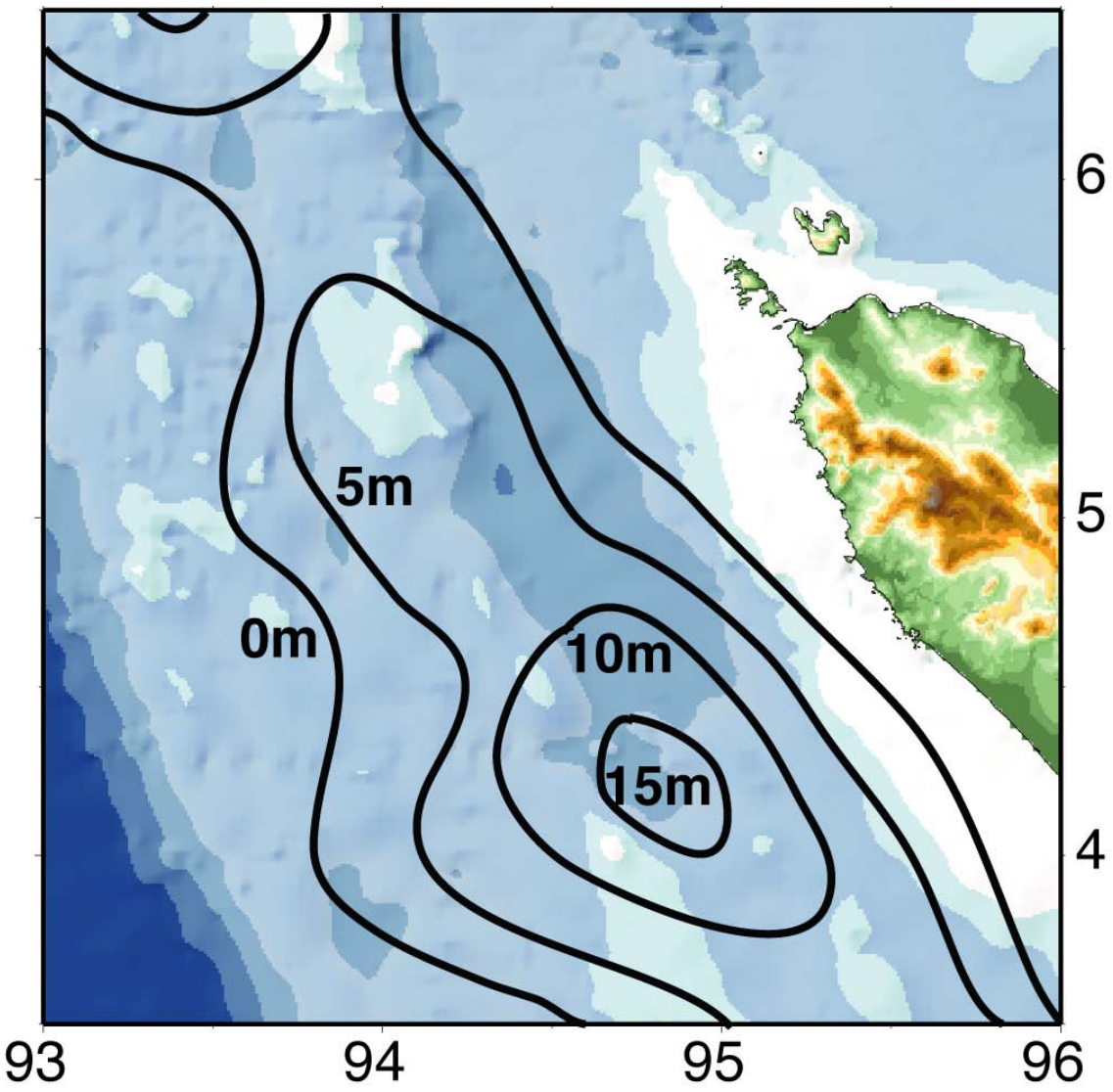

Figure **1-3**: Figure adapted from Chlieh *et al.*, 2007. Coseismic slip contours of the 2004 megathrust on the fault plane beneath the Aceh Basin. Contours are 5 m of slip.

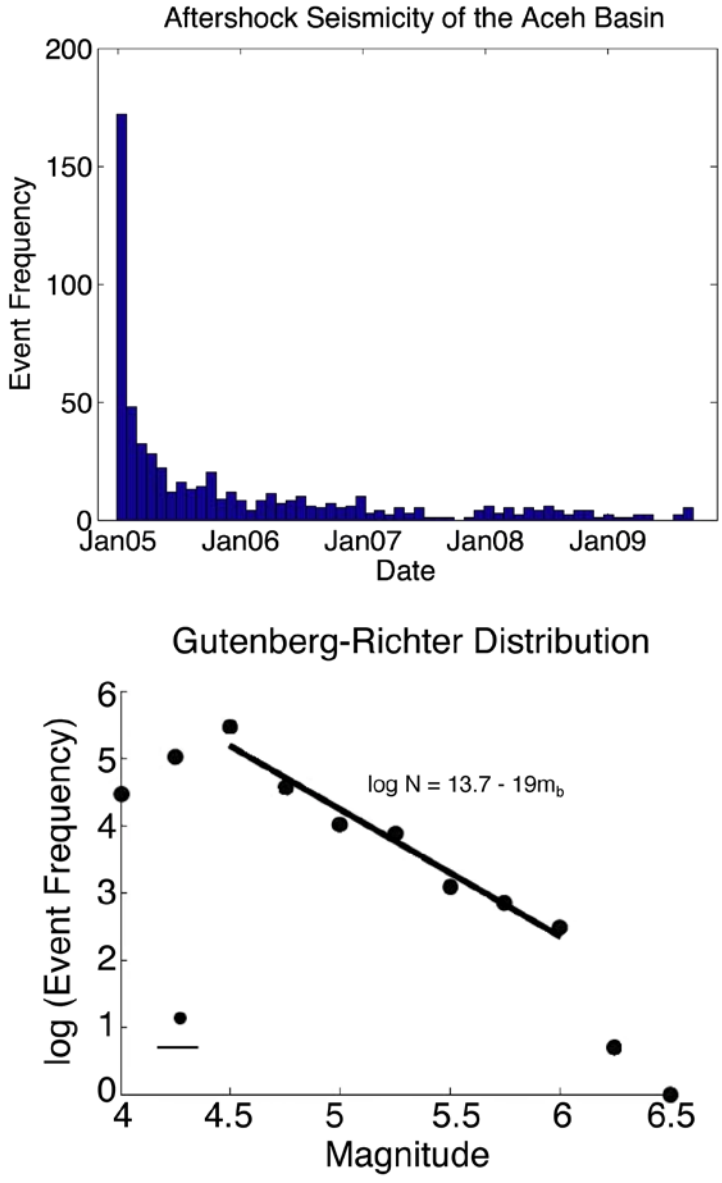

Figure **1-4**: Top: The aftershock decay pattern of the Aceh Basin approximately follows an Omori type decay pattern. Bottom: A Gutenberg-Richter distribution of aftershocks beneath the Aceh Basin. Events smaller than M 4.5 and larger than M 6 are eliminated from this plot due to avoid errors associated with catalog completeness. The *b* value of this relationship is rather high (1.9), compared to the expected *b*~1. The basin clusters may behave similarly to a swarm, as *b* values for swarms often approach 2.

Chapter 2

Seismological Analysis of Moderate-Magnitude Repeating Earthquakes Located Beneath the Aceh Basin

Of the thousands of earthquakes that occurred following the M_w 9.1 26 December 2004 megathrust earthquake, we investigated several hundred moderate-sized events ($m_b \geq 4.5$) that nucleated beneath or near the periphery of the Aceh Basin. For simplicity, we refer to all events since the 2004 megathrust earthquake as "aftershocks". For our event selection purposes, the Aceh Basin region was defined by the region bounded by vertices 93.6°E, 5.75°N; 95.0°E, 3.75°N; 95.7°E, 4.25°N; 94.5°E, 6.00°N. We investigated all events that have occurred between after the earthquake and the present. Thus the aftershocks span of six years, and exhibit typical Omori decay patterns with time. Most of the larger aftershocks beneath the Basin are consistent with low-angle thrusting, which suggests they are located within the plate boundary region (near the megathrust). Appendix A contains a summary of focal mechanisms by earthquake cluster. The focal mechanisms from the GCMT catalog are shown in Figure 1-1. The moderate size event depths have been estimated with travel times and body waveforms (USGS, Engdahl et al. 2007; Barrett, 2009) and are consistent with depths ranging from 30 to 50 km beneath the ocean floor.

Our event search used the US Geological Survey, National Earthquake Information Center hypocentral catalog. Earthquakes in any catalog may show bias, but this catalog is relatively complete in this region to a body-wave magnitude threshold of about 4.5. At this point, completeness is more important than location accuracy because we identified events beneath a broad region. We did not scan continuous waveforms to identify events not in the catalog, so it is possible that some events remain hidden, but our focus on events with sizes above the catalog completeness threshold, so these are likely few in number.

We acquired seismograms from 584 aftershocks and 140 older events (01 January, 1971 to 26 December, 2004) beneath the Aceh Basin from the IRIS waveform archive. Seismic instrument effects were deconvolved from the signal using functions built into the Standing Order for Data (SOD) data access tool (Owens et al., 2004). Before removing the instrument response described by the poles and zeros, removed a linear trend and the mean from the signal and applied a time-domain cosine observations, smoothly reducing the seismogram to zero over the first and last 20% of the time series. To stabilize the instrument deconvolutions, we applied a frequency-domain zero-phase cosine-taper high-pass filter with a cutoff at 0.005 Hz (200 s period) and a transition to full pass for frequencies higher than 0.008 Hz (125 s period). The procedure is similar to the standard functions implemented in SAC and commonly used in earthquake analyses. This low-frequency spectral taper is well outside the range of our analyses described below.

For our initial analysis of the entire suite of events, we selected signals from a large collection of teleseismic P-wave observations recorded at distance ranges between 30° and 95° to minimize wave propagation effects incurred from sampling the mantle transition zone or core-mantle boundary. After examining these data, we selected three high-quality stations, KURK (Kurchatov, Kazakhstan), WMQ (Ürümqi, Xinjiang, China), and BJT (Baijiantuan, Beijing, China) to use in a teleseismic P waveform event cluster analysis. All three stations were operating at the time of the 2004 mainshock, and all recorded at least 80% of the moderate-size earthquakes occurring beneath the Aceh Basin region since their installation. For our more detailed analyses of selected events within the teleseismically identified earthquake clusters, we also examined vertical-component signals from three regional stations PALK (Pallekele, Sri Lanka), CHTO (Chiang Mai, Thailand), and PSI (Prapat, Sumatera, Indonesia) to investigate the spectral properties of repeating events following their identification. We focused on the vertical

components regional signals because they are generally lower-noise than the horizontals, although the analysis could proceed with horizontals.

The station locations are show in Figure 2-1 and details of each of the stations are summarized in Table 2-1. Station BJT is located at 40.0183° N, 116.1679° E, 197 m and has been operational since 25 May 1994. The station recorded 518 of 633 target events (82%) and captured 473 of 584 aftershocks (81%). Station KURK is located at 50.7154° N, 78.6202° E, 184 m and began operation on 26 March 1995. The KURK data set contains 603 of a possible 628 events (96%) and captured 98% of the aftershocks. Station WMQ, is located 43.8138° N, 87.7049° E, 850 m and began operation on 19 October 1986. WMQ recorded 603 of 679 events (89%), and captured 90% of the aftershocks. The teleseismic stations are primarily to the NNW-NNE relative to the Aceh Basin, due to the higher density of available stations in that direction; there are few low-noise level stations in the southern oceans. We trust the station distribution does not significantly bias the results of the cross-correlation results.

The regional stations were used to compare events already clustered using the teleseismic stations. Station PSI, located at 02.6938° N, 98.9237°, E, 987 m, became operational 29 March 1993 (as part of the POSEIDEN Network). Station PALK, located at 7.2728° N, 80.7022° E, 460 m, became operational on 22 August 2000; and station CHTO, located at 18.8141° N, 98.9443° E, 420 m, began operations on 31 August 1992. We used the broadband signals from these stations, which are sampled at 20 samples per second, which limits the high-frequency range available to compare events. But the stations are located approximately 500 km (PSI) and 1500 km (PALK and CHTO) so most of the very high frequencies are attenuated by propagation. Several of the later events of interest were also recorded on the Malaysian Seismic Network, but we focused our efforts on the signals from PSI, which is closer and operating for the entire aftershock sequence (and earlier).

Teleseismic Waveform Cluster Analysis

A waveform from a seismic event at a given station has a characteristic signature based on the source characteristics and the regions of the Earth it samples between the source and the station. We systematically compared the waveforms of each event using an amplitude-normalized cross correlation to measure similarity (identical waveforms have a correlation coefficient of one; perfectly dissimilar waveforms zero). Cross-correlation based similarity metrics are sensitive to noise. Small events that produce relatively low signal-to-noise ratios are difficult to pair in a simple cluster analysis, such signals are best searched for using methods that extract characteristics from known events of interest and then search noisier signals for those characteristics are more robust with noisy data (e.g. Maceira et al., 2010). Our focus on moderate-size earthquakes and the selected signal bandwidth reduces our susceptibility to background noise issues. However, events whose signals interfere with other events would produce a relatively low cross-correlation value.

We performed a simple cluster analysis using the teleseismic body waves from each of the three stations (independently). Before inter-event comparison, the P waveforms were filtered using a fourth order, Butterworth bandpass filter with corners at 0.5 and 4 Hz. To isolate the relevant portion of the waveform, the signal was windowed to include 10 seconds before the initial P wave arrival and 60 seconds after. The P-wave signal in each waveform is relatively short, and we include a full minute to insure that the coda of the signals contributes to the measure of waveform similarity. Before cross correlating the signals, we removed the mean and taper the signal 1/20 on each side. P wave arrival times were identified using the *iasp91* travel times built into SOD. Although accurate only to within a few seconds, the theoretical travel times are adequate to identify the P arrival time needed to window the signals.

We use the single-linkage (shortest distance) cluster analysis implemented in MATLAB to form a hierarchical tree of P-waveform similarity. The cluster trees are displayed as dendrograms for BJT (Figure 2-3), KURK (Figure 2-4), and WMQ (Figure 2-5). Of the 150 waveforms compared in the analysis, about 36 signals correlated with at least one other signal at a level of 0.95 or higher. In other words, roughly 20% of the moderate-size earthquakes used in the teleseismic analysis were produced from earthquakes close enough and similar enough to another event to suggest that the event may have repeated.

To identify repeating-earthquake candidates, we must choose a similarity tolerance that identifies signals from events that are either repeating or at the threshold of resolution. Following earlier investigators (Igarishi et al., 2003), we identified waveforms with correlation coefficients greater than 0.95 to be considered candidates for repeating earthquakes. Although we have only P waves in the correlation, the coherence of the P coda is an important part of the correlation measure, so we assume that two events with a strong correlation are indeed at least nearly co-located. Since our data set is not very large, we can examine and track events that have similar, but not 0.95 correlation tolerance. We discuss those later. Pairs of related events are termed "doublets" while groups of three or more events are referred to as "clusters". Our doublets and clusters are consistent with those that might be inferred from using the relocations estimated by Engdahl et al., (2006), when available.

Repeating Earthquake Characterization

Before presenting a detailed analysis of the repeating earthquake patterns illuminated by the cluster analysis, as well as exploring what the strong correlations may mean in terms of repeating or nearly co-located events, it will be helpful to consider simple models of moderate-size earthquakes. The events of interest are occurred deep within the seismogenic zone, at depths

ranging from 30 to 50 km (e.g. Barrett, 2009). Pressures at these depths are in the range are in the range from 0.75 to 1.25 GPa (assuming a mean density of about 2,600 kg/m^3). Temperatures in the region at a depth of about 40 km were estimated by Subarya et al. (2006) to be in the range of 350°C, close to the value often assumed to produce an onset of aseismic creep near the base of subduction zone seismogenic zones (e.g. Hyndman et al., 1997). In fact, assuming no unusual characteristics, the megathrust beneath the Aceh Basin may span the region from seismogenic to aseismic, including the entire range of conditional slip. Since earthquakes nucleate across the entire basin, at least parts of the plate boundary region remain frictionally unstable to depths near 50 km.

To discuss the meaning of correlations of the seismic wavefield, it will be helpful to have some idea of the size of the repeating earthquakes. Empirical relationships are often used to estimate slip values of repeating earthquakes (*e.g.* Nadeau and Johnson, 1998; Nadeau and McEvilly, 1999; Templeton *et al.*, 2008); however, these relations may better model smaller repeating events. To get a rough idea of the dimensions and slip occurring during these moderate-size earthquakes, we must make some simple assumptions. To interpret the observed seismic amplitudes, we need seismic moment, which is the product of the rupture area (A), the shear modulus of the surrounding geology (μ), and the average slip during an earthquake (d)

$$M_o = \mu A d \quad . \tag{2.1}$$

We assume the asperities beneath the Aceh Basin have shapes that can to first order be approximated as circular cracks with radius r. Using the seismic moment estimates from the GCMT solutions, an assumed shear modulus, and a typical earthquake stress drop ($\Delta\sigma$), we can estimate the area of an earthquake from an empirical relation for radius (Kanamori and Anderson; 1975)

$$r \approx \left(\frac{7}{16} \frac{M_o}{\Delta\sigma} \right)^{1/3} \tag{2.2}$$

Once we know *A*, we can estimate the slip from (2.1). If we assume that the stress drop associated with the events is in the range from 1 to 10 MPa, then for seismic moment ranging from 4.0 to 8.0 x 10^{16} Nm, we estimate crack radii in the range from 1 to 3 km. Assuming a shear modulus of 32 GPa suggests that the displacement across the fault would be on roughly 5 to 25 cm (lower stress drops correspond to larger areas and lower slips).

Quantifying Event Similarity Using Seismic Waveforms and Spectra

To explore whether each of our highly correlated events does in fact represent the repeated failure of a single asperity, or two closely spaced features, we explored teleseismic (Δ ~5,000 km), far-regional (Δ ~1,500 km) and near-regional (Δ ~500 km) regional seismic signals. We illustrate our analyses using signals from stations KURK, CHTO, and PSI (Figure 2-1) and events from cluster G, which had the most events (discussed in detail in the next chapter). Station PSI (roughly 500 km distant) naturally had signals with the shortest periods, but recorded only four of the seven repeating events in this cluster. Figure 2-6 is a plot of the vertical component of velocity observed at PSI for those four events. The signals are visibly coherent, although several seconds of time shift are apparent when using the USGS origin times to align the signals. The P-wave train begins near 80 s and the S-wave train begins at about 120 s, and the coda following each is rich in detail. Despite the strong visual correlation, we note the obvious variation in amplitudes of the signals – the events appear to radiate nearly identical waveforms of different amplitudes.

We selected 60-second time windows starting near the P and the S wave arrivals for spectral analysis. To create the windows, we picked a distinct feature (a peak in acceleration) in each signal, and then selected 60 seconds of the signal starting 5 seconds before the features. The first distinct feature is one or two cycles after the P wave, the second feature was near the start of

the S-wave train, so we refer to these as the P and S wave trains respectively. We computed the amplitude spectrum of each signal by windowing the signal, removing the mean, applying a three-second wide cosine taper to each end of the signal, applying a Bartlett window to the resulting time series and estimating the power spectral density (PSD) using the periodogram. To stabilize the PSD estimate, we smoothed the power spectral values using an 11-point moving average applied to the values in both forward and backward frequency directions (effectively producing a triangular weighted averages centered on each spectral data point). The frequency-sampling interval was 0.0098 Hz, so the triangular smoothing window is roughly 0.1 Hz wide.

The resulting ground-acceleration spectra (square root of the PSD) are shown in Figure 2-7 (P-wave train) and Figure 2-8 (S-wave train). The thick lines identify the spectra of the seismic signals, the pre-P-wave arrival background noise spectra are shown using the thin lines. Signal-to-noise ratios are generally high out to roughly 5 Hz for P waves and 4 Hz for S waves. For a standard Brune-type source model, the high-frequency fall off proportional to the square of frequency in displacement is equivalent to a flat acceleration spectrum. We have not corrected for attenuation and we are not simply looking at a direct P or S wave, so interpretation of the spectra in light of simple models is not straightforward. Our interest is in how similar the spectra are, not in a simple mechanical interpretation of the observations. At low frequencies (0.5 to 1.5 Hz) the signals from the four events cluster into two pairs, two larger, and two smaller events, compatible with the observation of varying time-domain amplitudes. S-wave spectra are generally consistent out to at least 3 Hz, which corresponds to wavelengths of roughly 2-3 km for a P wave and 1-2 km for an S wave. The events are almost certainly few km of each other (if not co-located) so the along-path effects are almost certainly stationary. Differences in the spectra result from noise, variation in the source (rupture or location), and near-source scattering, which may change if the source position is shifted. We examined spectral ratios that would equalize attenuation and geometric spreading effects to see if we could identify subtle changes corresponding to variations

in the source time functions. The ratios showed little evidence for a simple change such as expected from a variation in a corner frequency. Some of the high frequency coherence could reflect variations in the signal coherence that varies with time, which is expected if the events were not co-located.

To explore the time-dependence of signal coherence, we used the method of Snieder and Vrijlandt (2004), who considered the effects of small changes in source location on the seismic coda. The method is simple and elegant – assuming that the sources are surrounded by a randomly distributed collection of isotropic seismic wave scatterers that produce the observed seismic coda, Snieder and Vrijlandt (2005) developed relatively simple relationships that relate the coherence of the seismic coda for two events to a bound on the difference in location between the events. The method accounts for double-couple radiation but assumes similar source time functions for the two events. One expects that differences in source time functions or lack of ideal scattering locations to inflate the estimate of distance between the events, so we employ the method to estimate the distance between events in our clusters. A small distance would suggest that the events were in fact repeating events, not simply nearby events. We assumed events in our cluster occur on the same fault surface.

We performed the analysis on vertical component velocity seismograms recorded at all three distance ranges and present example results for stations KURK, CHTO, and PSI, again using events from cluster G. We aligned the waveforms on a distinct arrival near the P wave before measuring the maximum cross correlation in non-overlapping 10 s wide windows beginning before the P wave and continuing well into the coda (and past the S wave for station PSI). To bound the distance between the events, we must compute the peak of the normalized cross-correlation, the average frequency, and assume a P and S-wave speed for the source region. The results are relatively insensitive to the assumed seismic wave speeds and we used values of 6.7 km/s and 3.9 km/s for the P and S wave speeds. For the teleseismic station, we used velocity

seismograms high-pass filtered with a corner at 0.5 Hz. For the regional stations we used velocity seismograms high-pass filtered with a corner at 1 Hz. We did not correct the maximum cross-correlation values for noise as suggested in Snieder and Vrijlandt (2005) since our signals generally have rather strong signal to noise ratio.

The coda-wave interferometry method of Snieder and Virjlandt (2005) is elegant and straightforward. We use the cross correlation to estimate the variance of the scattered wavefield travel times using

$$R = 1 - \frac{1}{2}\omega^2 \sigma_T^2$$

where R is the maximum normalized value of the cross correlation, ω is the average radial frequency in the signal (estimated from the observations), and σ_T is the desired scattered-wave travel time variance. Then we use a relation between the travel time variance and the distance between sources to estimate the inter-event distance. For two events on the same fault surface

$$\delta^2 = 7\frac{\left(\frac{2}{V_P^6} + \frac{3}{V_S^6}\right)}{\left(\frac{6}{V_P^8} + \frac{7}{V_S^8}\right)}\sigma_T^2$$

where V_P and V_S are the P and S-wave speeds respectively and delta is the source separation distance. The material property terms are a result of integrals including P and S wave radiation pattern, but assume a uniform faulting geometry and source time functions. Before applying the method to our data, we note that for a given bandwidth, the maximum square distance you can estimate from this formula (for R = 0.5, equivalent to noise) is

$$\delta_{\max} \approx \left\{ 7\frac{\left(\frac{2}{V_P^6} + \frac{3}{V_S^6}\right)}{\left(\frac{6}{V_P^8} + \frac{7}{V_S^8}\right)}\omega^{-2} \right\}^{1/2} .$$

For our values and assuming a 1 Hz mean frequency, the result is 1 km. The method is more robust with a broad bandwidth that includes higher frequencies.

We present the results for the first and last event (chronologically), which also show the largest change in amplitude. Figure 2-9 shows the calculation using the KURK teleseismic P waveforms for the first and fourth events available at all the stations. The top panel shows the filtered velocity seismograms (on the same scale). The difference in amplitude is clear. The second panel shows the normalized cross correlation estimated in non-overlapping, 10 s wide windows sliding sequentially along the seismograms. The inter-event signal correlation is very high for the first 50 seconds and stays relatively high for about two minutes. The third panel shows the relative size of the two signals measured from the cross correlation, which is between 0.75 and 0.50 for most of the strongly correlated segments of the waveforms. The average frequency for each window is shown in the fourth panel, this value is generally around 1 Hz for the teleseismic waveforms. The final panel shows the estimated bound on the distance between the two events. The initial estimate is generally below 300 m, and for the first two minutes the bound remains below 500 m.

The results for CHTO are shown in Figure 2-10. The figure format is the same. The CHTO record is an interesting test of the method in that another signal interferes with the first Aceh Basin as can be seen clearly just after 120 s. The first minute of the signal is high quality and has substantial complexity to locate the two events. When the correlation is high, the estimated distance between the two events is 400 m or less. The relative amplitude of the signals in the first minute is just under 0.75. In general, the results are consistent with the results of KURK. Note that when the two different signals are compared, the difference in location does not increase much, which suggests caution is required when using this method with distant observations. A comparable analysis of other events in the cluster shows strong coherence for two minutes of the regional signal, and again suggests that the events are less than 0.5 km apart.

Results of the analysis applied to signals from station PSI are shown in Figure 2-11. In many ways these are the most meaningful in that they include both P and S arrivals recorded much closer to the source (but still ~500 km). As before the signals were aligned on a distinct feature in the P waveform. Any substantial difference in distance would affect the S-P arrival time as well as the coda. The cross correlation begins relatively low near the reference time, but the frequency is higher at the same time. The correlation then increases P coda to values above 0.9 when the S waves arrive. Although not shown, the optimal lag for the cross correlations (in all cases discussed) is generally ±1 time sample. The amplitude ratio of the signals is fairly steady between 0.5 and 0.75. The estimated maximum distance between the events is again less than 500 m. Comparisons of the other events are generally better than those shown in these examples. We note that comparisons with other available events in this cluster suggest event closer sources, less than 300 and as low as 200 m.

Data from all three distances are consistent and suggest that the events all the events in this cluster are likely less that 500 m apart. Given that the range in diameters of events of these sizes are from 2 to 6 km, we feel that the analysis has verified that are observations correspond to the repeated failure of the same asperity. The amplitude fluctuations also suggest that the asperity is evolving with time since the main shock. As discussed in the next chapter, this cluster and others show an overall decrease in moment with time after the mainshock. Perhaps more interesting is the decrease in moment with increasing time between events, the opposite of what we expect from accepted views of fault friction.

Table **2-1**: Information on Stations Used in the Cross Correlation Analyses

Station	**Network**	**Distance(°)**	**Azimuth(°)**	**Operational**	**% Events Recorded**
BJT	IC	39.7	26.7	25/05/1994	82%
KURK	II	47.0	346.5	26/03/1995	96%
WMQ	IC	38.7	352.5	19/10/1986	89%

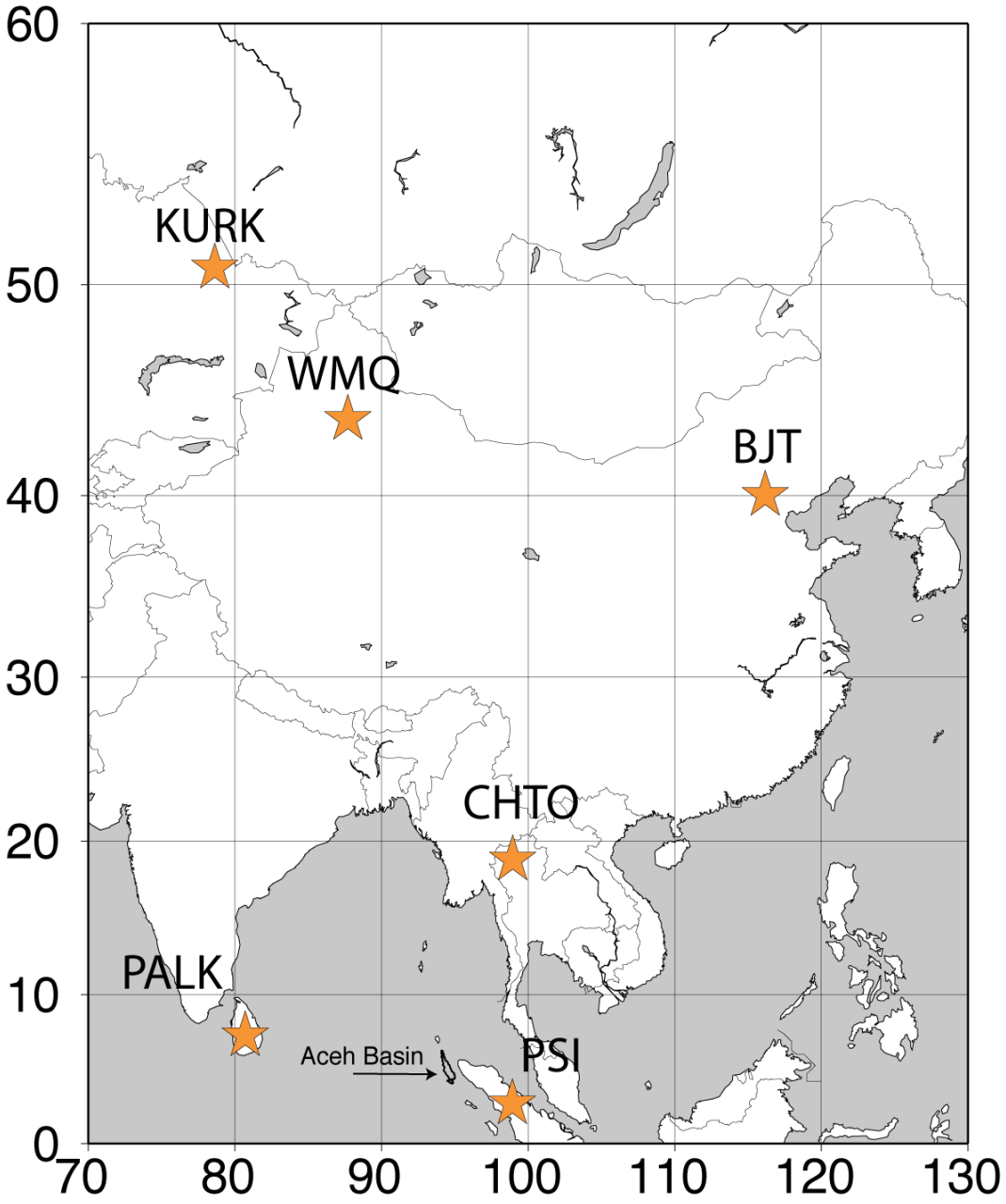

Figure **2-1**: Locations (stars) for seismic stations used to identify and analyze repeating events beneath the Aceh Basin. Source-to-station distances range from about 500 to 5,000 km. Stations KURK, WMQ, and BJT were used to identify repeating earthquakes, the regional stations CHTO, PALK, and PSI were used to estimate the possible differences between events that look similar at teleseismic distances.

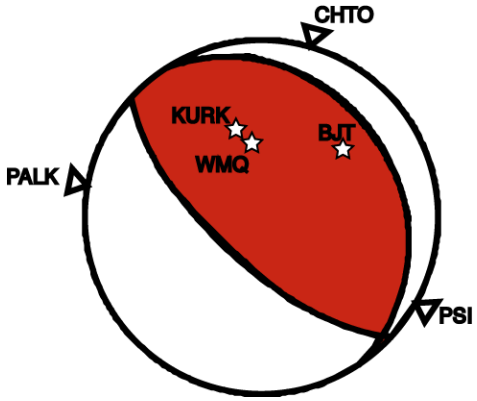

Figure **2-2**: Teleseismic and regional station locations used in asperity analysis on an average aftershock GCMT focal mechanism. For teleseismic stations, we plot the direct arrival of the P-wave-shown at the appropriate azimuth and distance on the focal mechanism. Regional stations are plotted from P and S arrivals and reflections at their azimuth relative to the Aceh Basin.

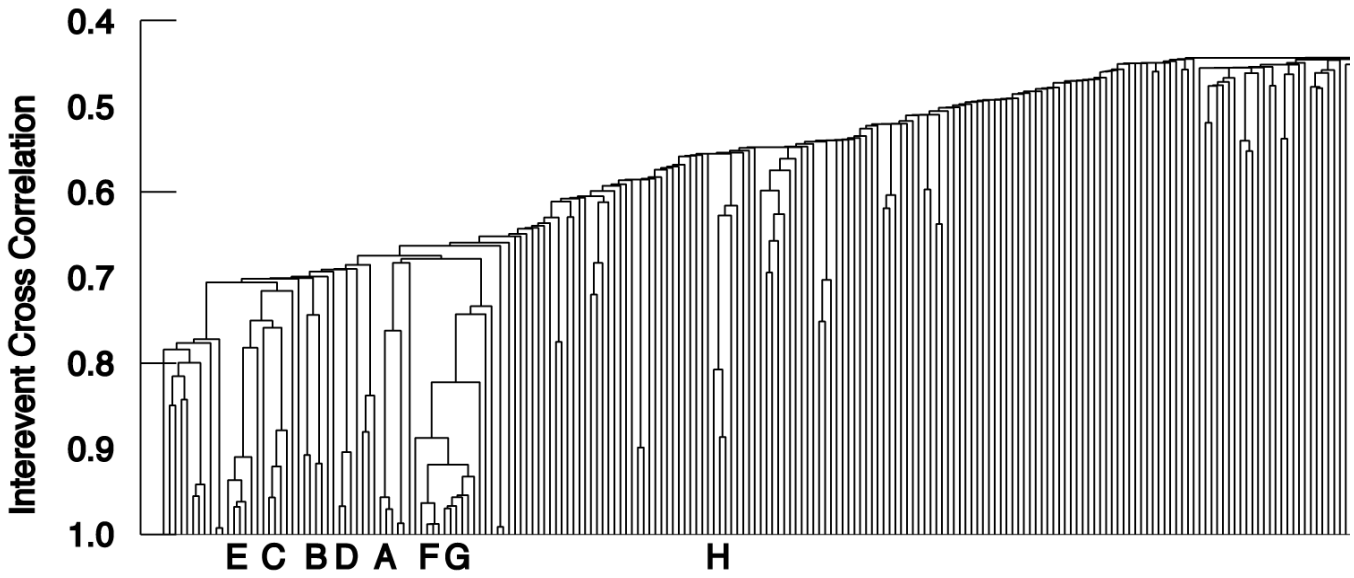

Figure **2-3**: Dendrogram of the cross-correlation coefficients for each of the 518 events as recorded at station BJT. Events correlating at greater than 0.95 are deemed part of a similar asperity

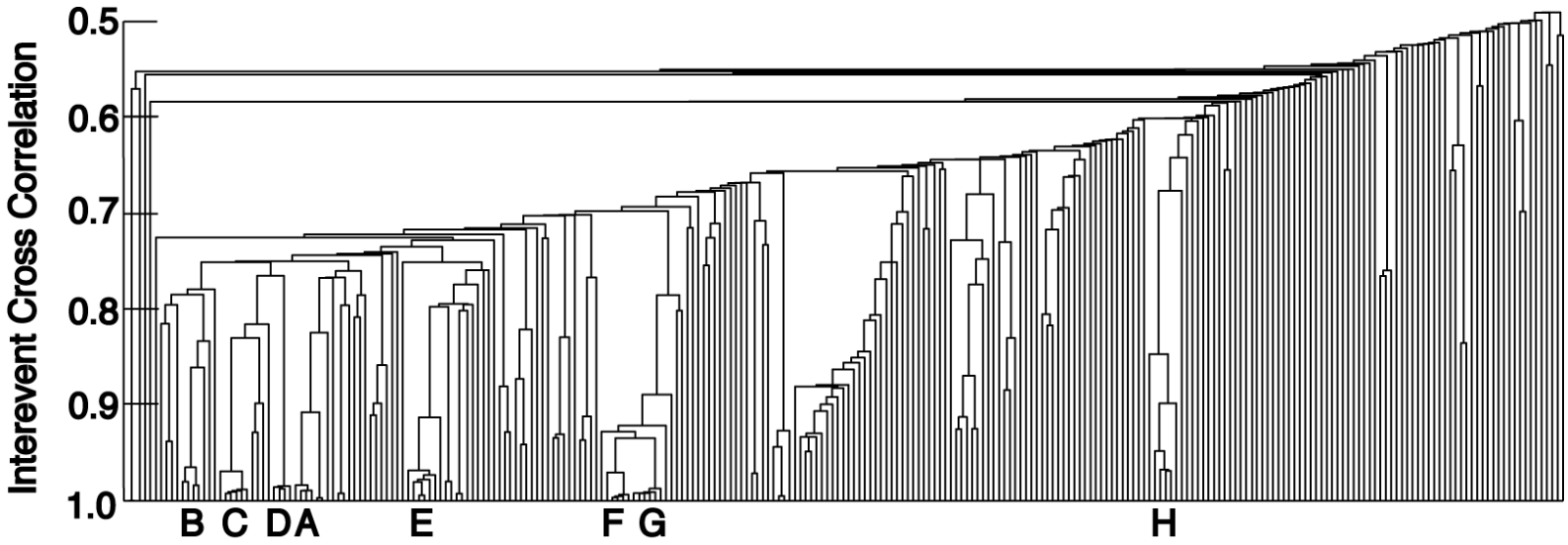

Figure **2-4**: Dendrogram of the cross-correlation coefficients for each of the 603 events as recorded at station KURK. Events correlating at greater than 0.95 are deemed part of a similar asperity

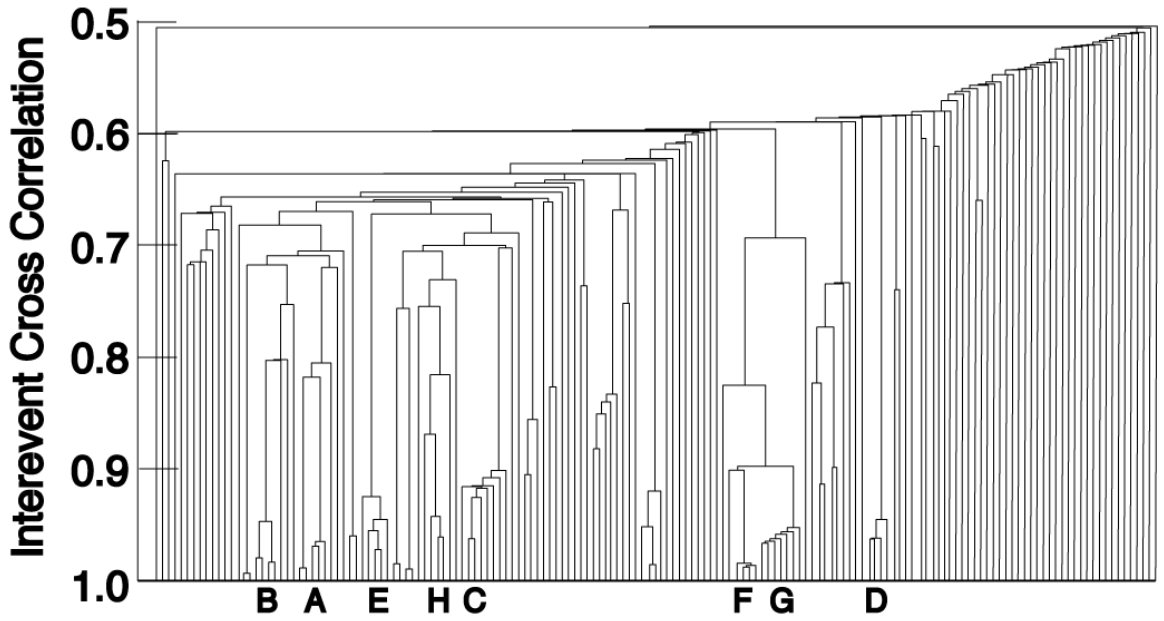

Figure **2-5**: Dendrogram of the cross-correlation coefficients for each of the 603 events as recorded at station WMQ. Events correlating at greater than 0.95 are deemed part of a similar asperity

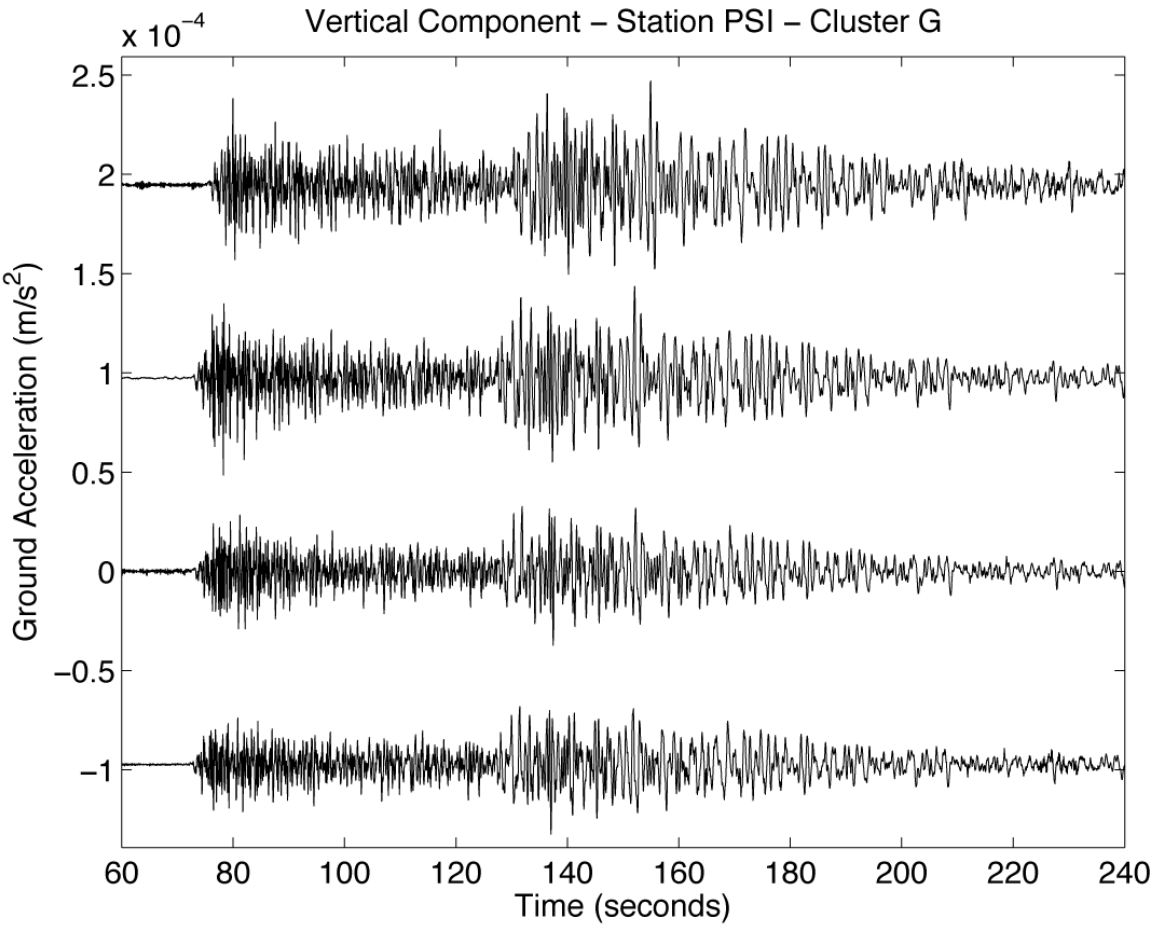

Figure **2-6**: Vertical component accelerations observed at station PSI for four events in cluster G. The reference times are the USGS origin times, so the events are not optimally aligned. These data are aligned and used to compare the spectral amplitudes of signals radiated by the four events.

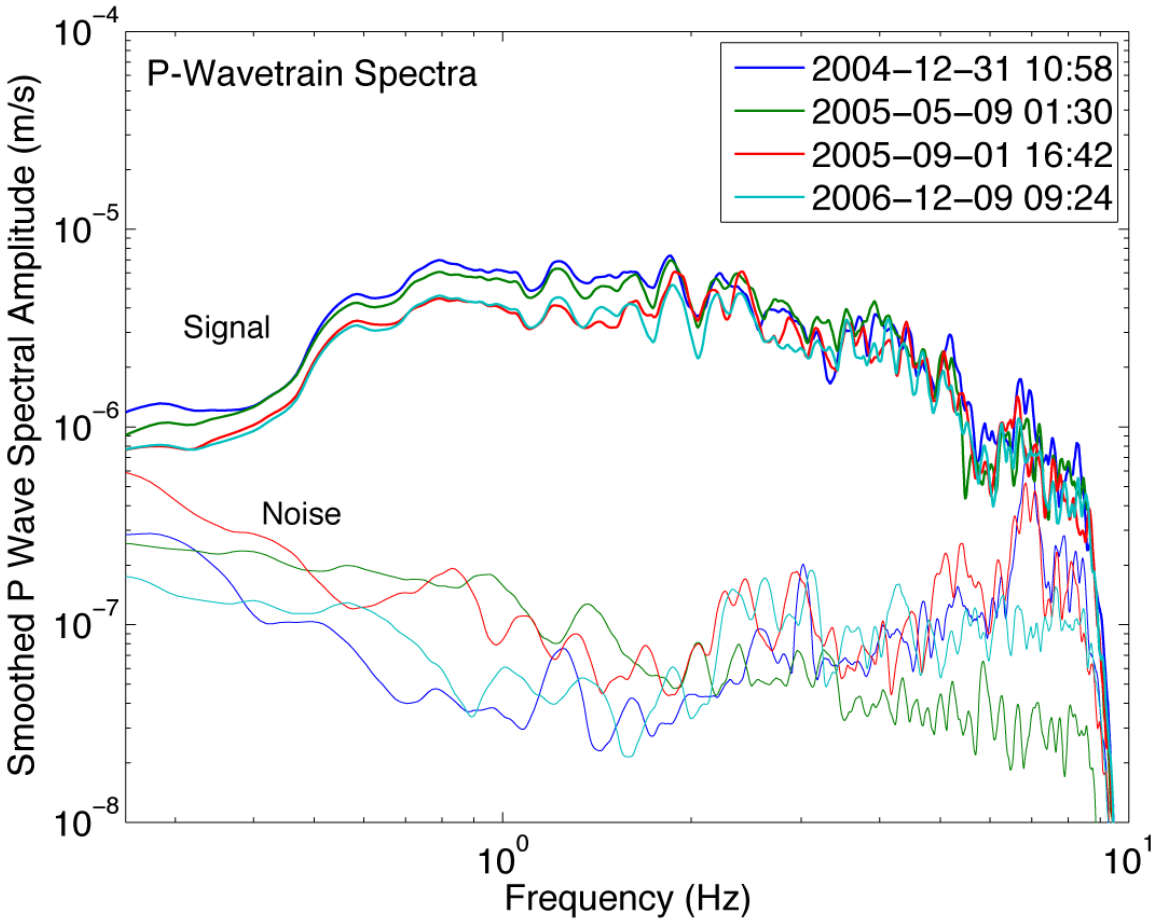

Figure **2-7**: P-wavetrain ground acceleration spectra estimated for the four vertical component signals observed at station PSI, about 500 km from the sources. The thin lines identify pre-signal noise amplitude spectra, the thick lines identify to the P wavetrain spectra. Colors identify four events of cluster G for which signals were observed at station PSI.

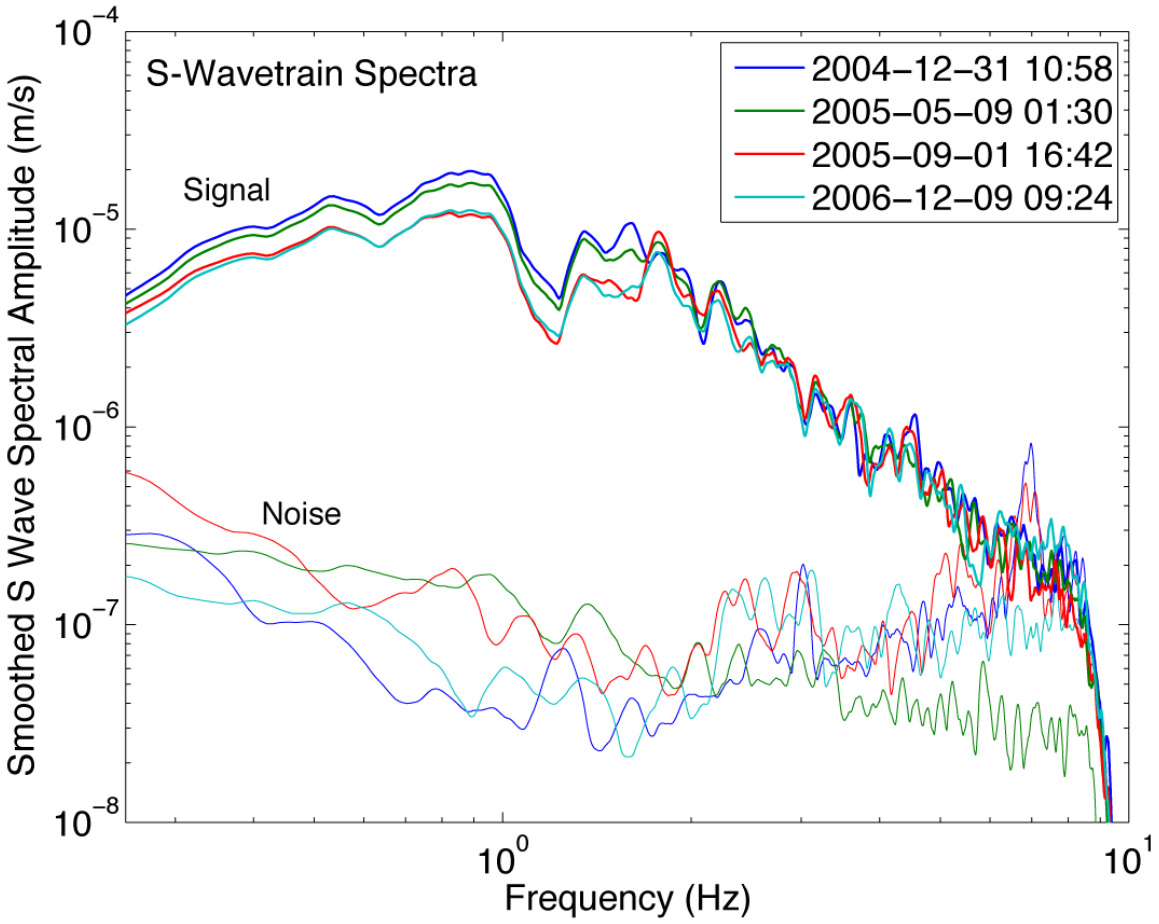

Figure **2-8**: S-wavetrain ground acceleration spectra estimated for the four vertical component signals observed at station PSI, about 500 km from the sources. The thin lines identify pre-signal noise amplitude spectra, the thick lines identify to the S wavetrain spectra. Colors identify four events of cluster G for which signals were observed at station PSI.

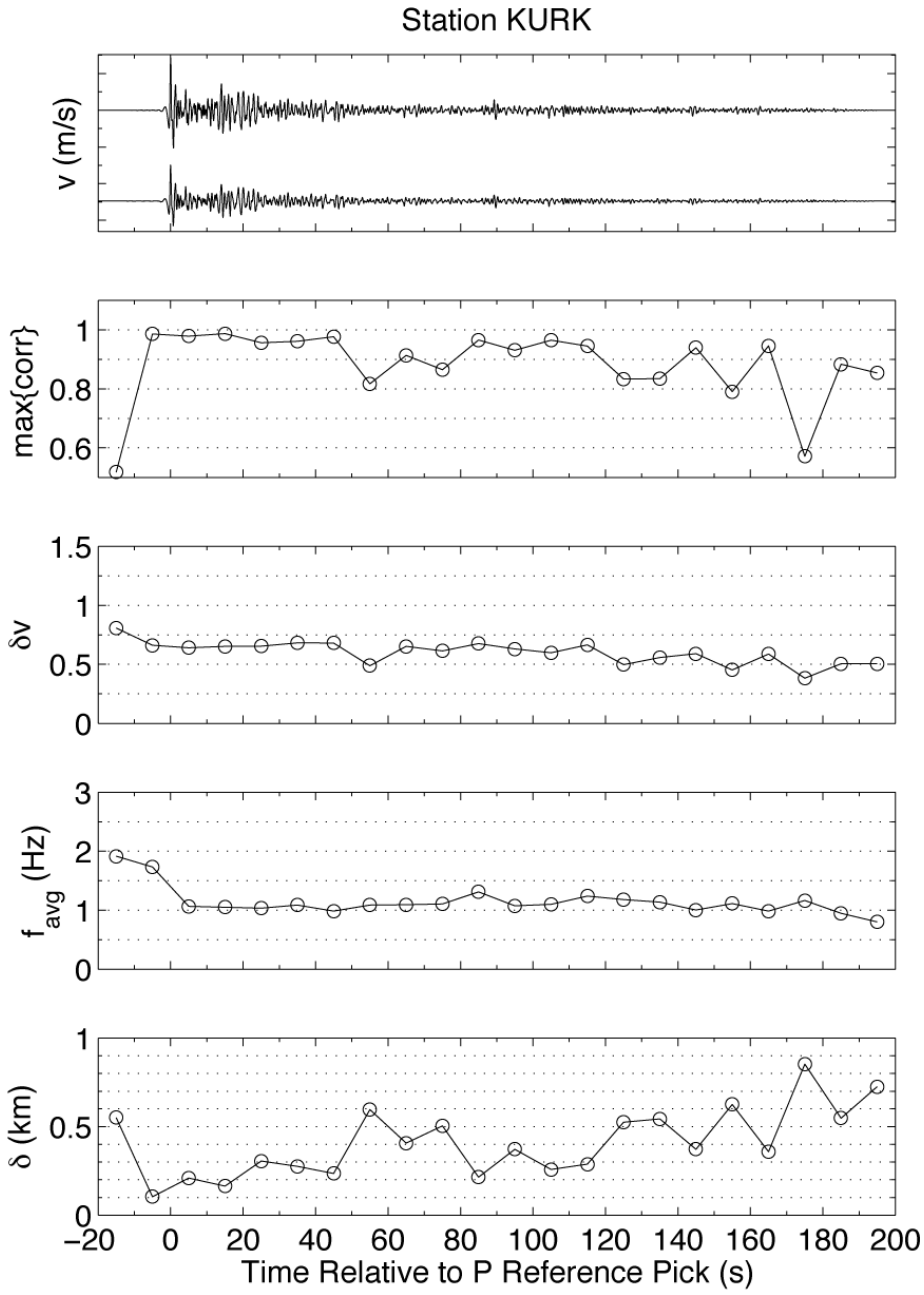

Figure **2-9**: Coda wave interferometry analysis of teleseismic P waveform signals observed from two events in cluster G at station KURK. The top panel shows the filtered ground velocity signals used in the analysis. The second panel shows the maximum cross correlation of the signals in non-overlapping windows along the time series. The third panel shows the relative amplitudes of the two signals in each 10-second window. The fourth panel shows the average frequency in each window, and the last panel shows the inter-source distance estimated from the maximum correlations and the average frequency values.

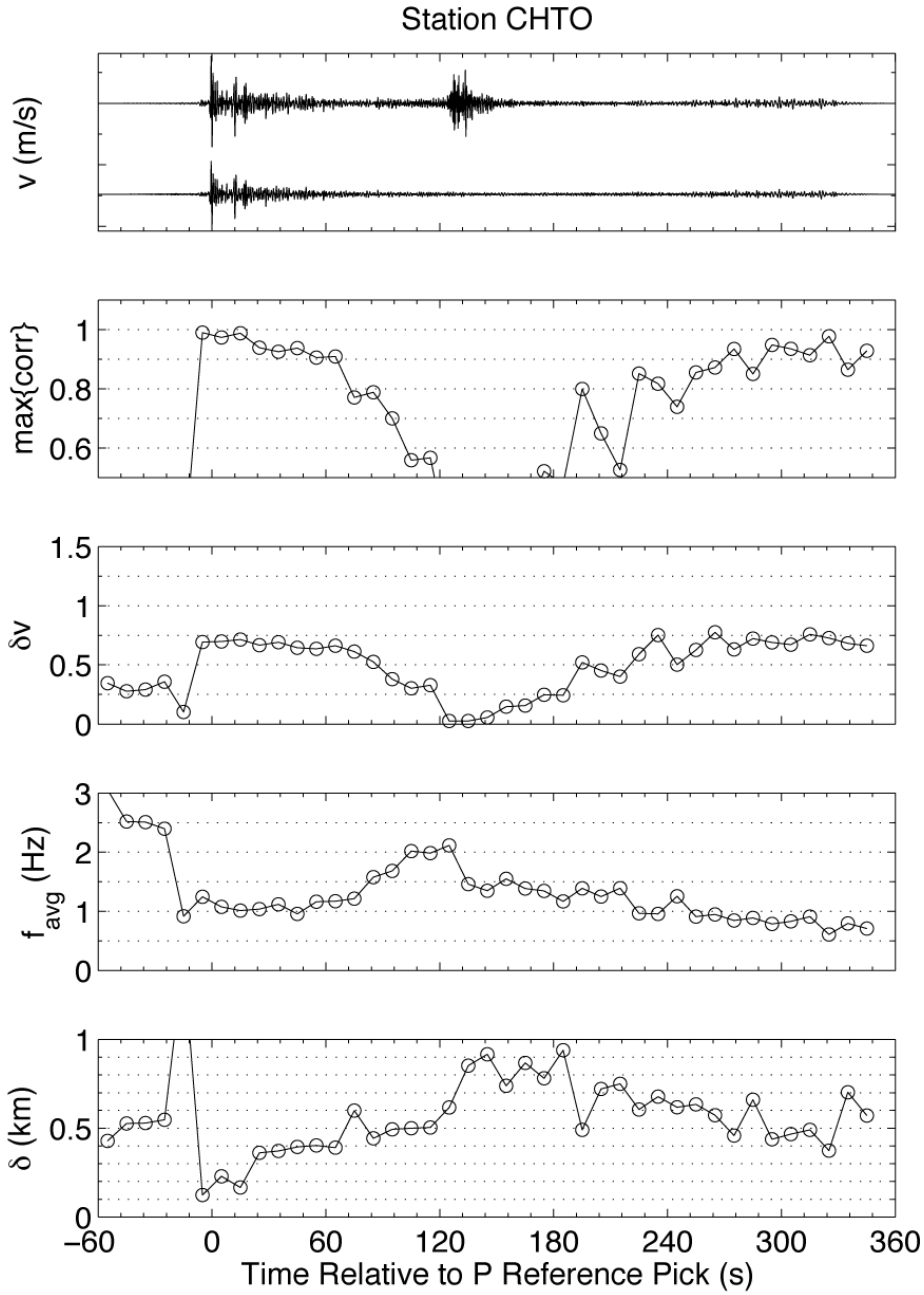

Figure **2-10**: Coda wave interferometry analysis of teleseismic P waveform signals observed from two events in cluster G at station CHTO. The top panel shows the filtered ground velocity signals used in the analysis. The second panel shows the maximum cross correlation of the signals in non-overlapping windows along the time series. The third panel shows the relative amplitudes of the two signals in each 10-second window. The fourth panel shows the average frequency in each window, and the last panel shows the inter-source distance estimated from the maximum correlations and the average frequency values.

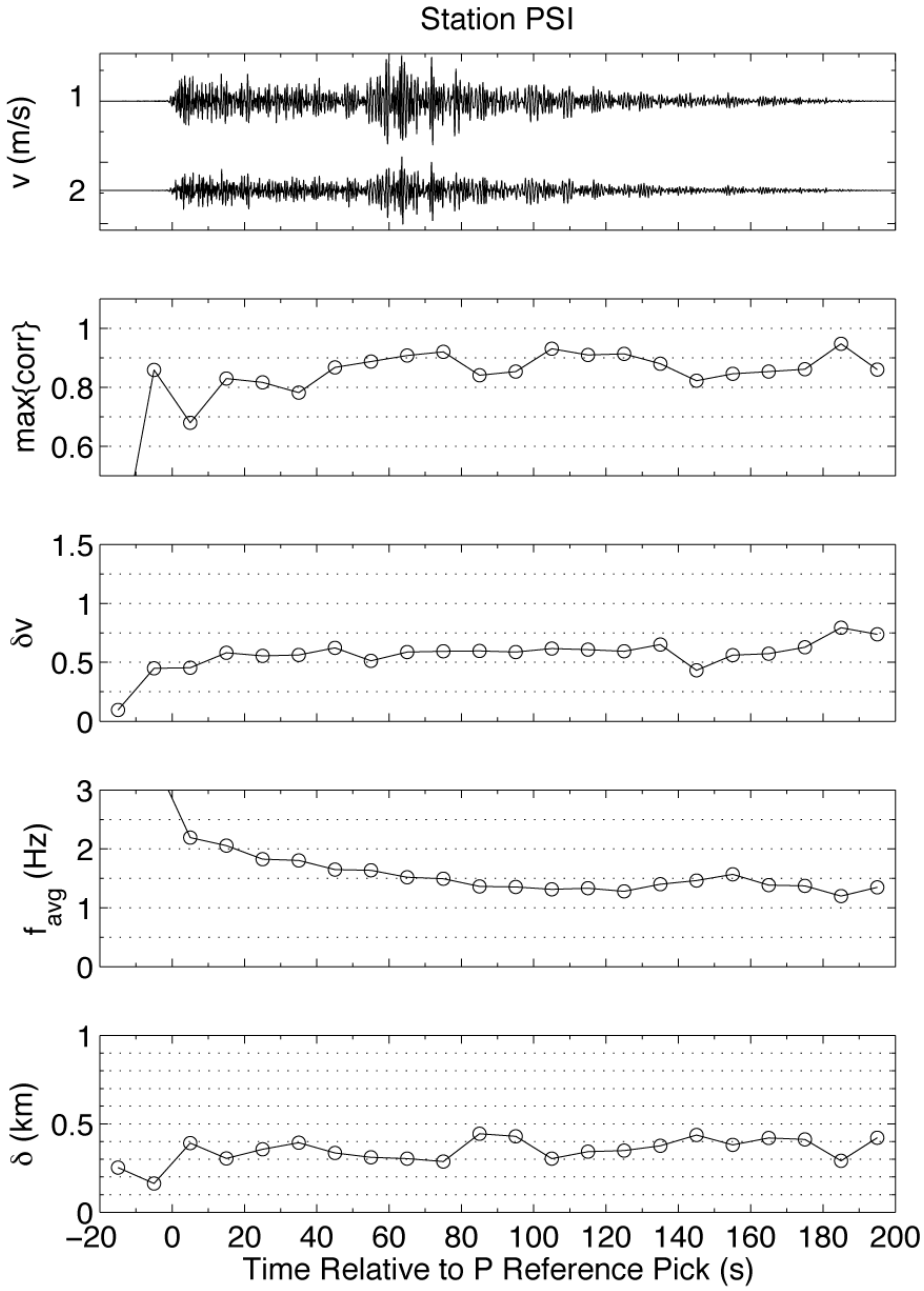

Figure **2-11**: Coda wave interferometry analysis of teleseismic P waveform signals observed from two events in cluster G at station PSI. The top panel shows the filtered ground velocity signals used in the analysis. The second panel shows the maximum cross correlation of the signals in non-overlapping windows along the time series. The third panel shows the relative amplitudes of the two signals in each 10-second window. The fourth panel shows the average frequency in each window, and the last panel shows the inter-source distance estimated from the maximum correlations and the average frequency values.

Chapter 3

Characteristics of Repeating Earthquakes Beneath the Aceh Basin

The cross-correlation cluster analysis identified eight groups of similar events, which we refer to using the letters A-H. The clusters are primarily located around the edges of the Aceh Basin (Figure 3-1), but show no systematic temporal pattern (e.g. migration along strike or dip). Clusters A-D and H are located near the northern end of the Basin, clusters F and G are located to the south. Clusters A,B, and H are up dip of the others. The aftershocks beneath the Aceh Basin can be categorized as "repeaters" (those that correlate with at least two other waveforms) or "non repeaters". The percent of repeating events (relative to all Aceh Basin events) increases with time. Following the mainshock only about 5% of Aceh Basin aftershocks were repeaters, while by the end of 2008, approximately 20% of the aftershocks could be classified as repeating event. As discussed below, the repeating events show two interesting characteristics – first, they tend to repeat less frequently with time, and second, they show amplitude variations that indicate an overall decrease of moment with repeated occurrence. We begin with a discussion of the temporal patterns, and follow with a discussion of amplitude variations.

Repeating Earthquake Recurrence Temporal Behavior

The increase in recurrence time from one event to another follows a logarithmic pattern, similar to that commonly observed for postseismic relaxation (e.g. Scholz, 2002; Segall, 2010). Not surprisingly it is clear that the repeating aftershocks beneath the Aceh Basin are being driven by post-seismic deformation occurring in the deep regions of the megathrust. Post seismic deformation is generally observed through surface deformation and has been attributed to three

basic processes, poroelastic deformation near the fault, which is believed to decay quickly with time, afterslip along the fault or its downdip extensions, or viscoelastic deformation of the lithosphere beneath the fault.

The simplest opinion of the repeating events is that of an asperity, surrounded by aseismically creeping region that repeatedly loads the enveloped seismogenic region to failure, which has been considered by a number of earlier investigators (e.g. Vidale et al, 1994; Schaff and Beroza 1998; Peng et al., 2005). Igarishi et al. (2003) classified seismic repeating events into two categories, continuous, which have a uniform mechanism and a uniform recurrence interval, and burst repeaters, which differ in that they are generally a response to deformation that occurs following a larger event (a mainshock). Burst repeaters in general may have a mechanism that differs from the mainshock, but generally have a uniform mechanism in the repeating sequence. More importantly, burst repeaters exhibit a variable recurrence interval (Figure 3-2). The repeaters beneath the Aceh Basin have a uniform mechanism and systematically varying occurrence intervals.

We view them as small regions that are repeatedly loaded by surrounding aseismic creep and slip when the load they support overcomes the frictional strength of the asperity. In that sense they can provide valuable information on the loading rates adjacent to the fault zone. Unlike surface observations, that integrate the effects of postseismic deformation over large regions, the repeating earthquakes provide a more localized measure. The numerical calculations of Malservisi et al. (2005) for a locked asperity surrounded by a creeping zone suggest that the area of the boundary loading the asperity is on the order of one to two widths of the asperity, so these moderate-size repeating events beneath the Aceh Basin provide an estimate of the loading rate or creep over a few kilometers spatial scale.

The observed event recurrence patterns are shown in Figure 3-3. For clusters A, B, F, and G, a linear relationship between the logarithm of recurrence time and event occurrence is clear.

Cluster C shows an initial linear relationship that eventually levels as the recurrence interval appears to reach a steady-state value of about 300 days. Cluster E shows a complicated behavior with three events separated by roughly 15 days, then about three events separated by about 300 days. Cluster D shows a roughly logarithmic increase in recurrence time, but with only four events and three recurrence intervals, a more complex structure may not be obvious. Clusters C, E, and D are located in the same general region, deep within the seismogenic zone near the north end of the basin. The complexity in the local loading rates likely reflects a more regional evolution of the postseismic relaxation in the area. The transition to a more uniform loading rate near clusters C and E occurs some time after about 250 days.

We can map the recurrence to a cumulative slip as a function of time since the mainshock if we assumed a simple mechanical model for the repeating earthquake source. If we assume that the strong-correlation of the waveforms indicates that the rupture area remains roughly fixed, then the variation in seismic moment suggests that the slip in each event varies. To use the information to estimate the slip in each event, we also must assume a stress drop to estimate a rupture area. We performed calculations with stress drop values of 1, 3, and 10 MPa, and we used a shear modulus of 40 GPa, which corresponds to a P-wave speed of about 6.7 km/s and a density of 2,700 kg/m^3. With these assumptions we can estimate the cumulative slip curves for each cluster and a 10 MPa stress drop are shown in Figure 3-4. Since the estimated slip values for these size events is on the order of 10 cm, the total seismogenic slip observed on the asperities is roughly 0.5 meters in all cases. Our estimates are substantially less than the post seismic slip modeled by Chlieh et al. (2007), who estimated a few meters of afterslip along the plate boundary beneath the Aceh Basin. One could account for this deficit (increase the amount of slip on an asperity for an event of a given magnitude) by increasing the stress drop or by decreasing the shear modulus. To accommodate 5 m of slip beneath the Aceh Basin (a modest estimation) we would need to increase the stress drop to a value of ~250 MPa or decrease the shear modulus to 1.5 GPa, neither

of which is likely. Either we are seeing a much more localized feature in a broad regional signal, the surface-observations are overestimating the afterslip, or the asperities are accumulating much more slip aseismically than they release seismically.

Repeating Earthquake Amplitude Behavior

Teleseisimic P waveforms recorded at KURK for events in cluster G show a moderate overall decrease in amplitude with event (Figure 3-5). This pattern is prevalent throughout all the clusters and observable directly in the teleseismic waveforms (Appendix B contains a plot of all the teleseismic waveforms for each cluster). We performed a systematic comparison of cluster G teleseismic P waveforms for (KURK, WMQ, and BJT). The observed amplitudes correspond to signals with frequencies in the 1 to 2 Hz band. They differ from station to station because of differences in radiation pattern, geometric spreading, and attenuation along the paths, and perhaps differences in directivity (if they are observable). We can equalize all these effects by normalizing the signals at each station using signals from a reference event. We can also compare the long-period moments estimated for events as part of the GCMT procedure by normalizing the seismic moment for the same event. The comparison shows that the short-period (1-2 Hz) observations and the long-period (0.025 Hz) GCMT observations are generally consistent. Thus no changes in the source from event to event are perceptible for periods longer than about 1-2 Hz. The same was true in the regional signals from PSI, which included slightly higher frequencies and both P and S waves. This is consistent to first order with our assumption that the area of each rupture did not change.

We show the observed P wave amplitudes as a function of time since the mainshock for each cluster in Figure 3-6. For simplicity, we normalized each amplitude to that of the first event in the cluster. With the exception of cluster D, all clusters show a decrease in relative amplitude

(and hence seismic moment) with time since the mainshock (Figure 3-7). Several clusters initially show an increase, but the overall trend is generally to decrease moment with repeated occurrence of earthquakes on the asperities. The pattern is intriguing, since for most of the earthquakes the recurrence interval is either remaining nearly constant or increasing with time after the mainshock. The expected result for an unchanging asperity is an increase in moment with time.

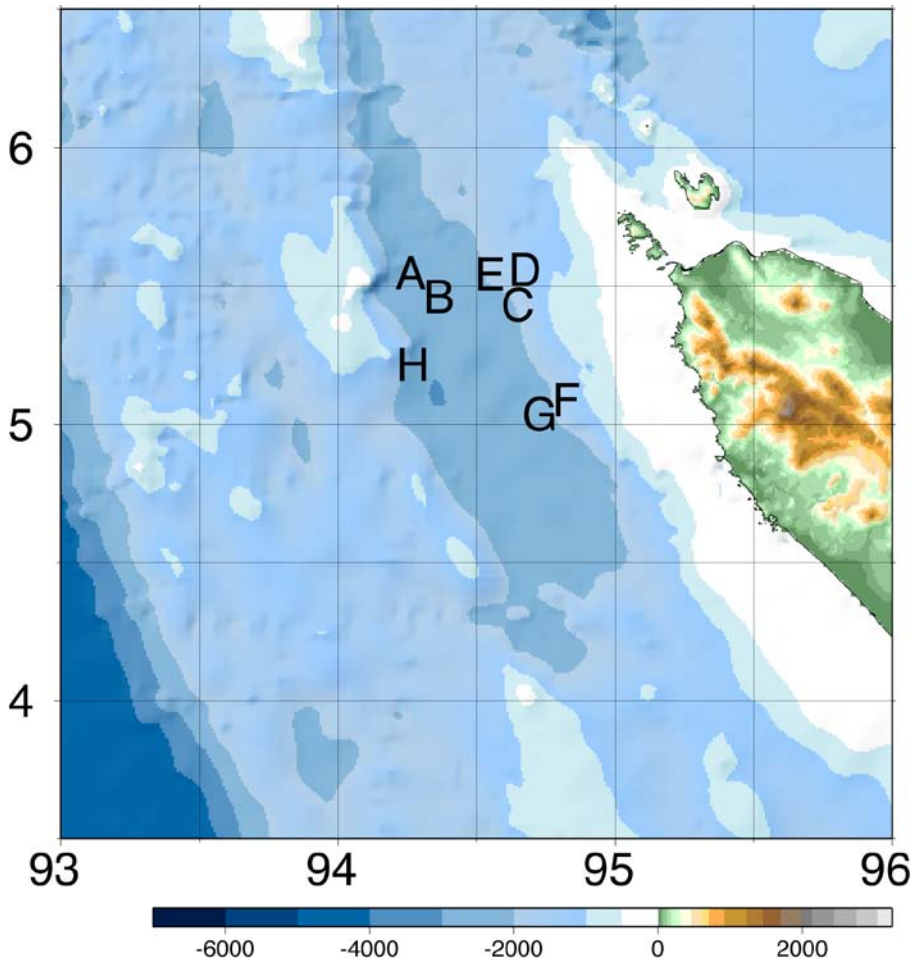

Figure **3-1**: Locations of the eight indentified clusters (A-H) of repeating events beneath the Aceh Basin. Cluster locations are the mean of EHB locations for every event in the cluster. Clusters A, B, and H are located up dip of the others, and clusters C, D, E and G, F are located near the base of the inferred seismogenic zone.

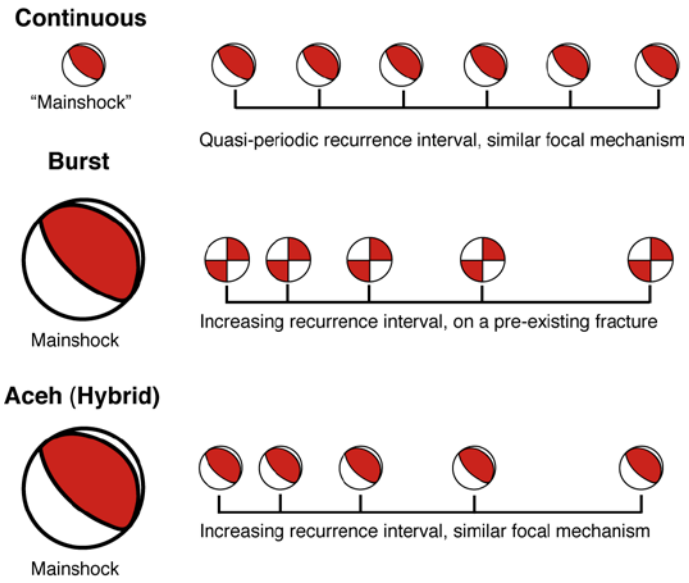

Figure **3-2**: A summary of repeating earthquake styles based on the categorization of Igarishi et al. (2003). Continuous type events have regular recurrence intervals and a similar estimating the plate (or fault) motion rate. Burst type events occur with increasing recurrence intervals and generally nucleate on pre-existing fractures. The Aceh events are unique in that they have a similar focal mechanism (like continuous type events) but have increasing recurrence intervals (like burst type events).

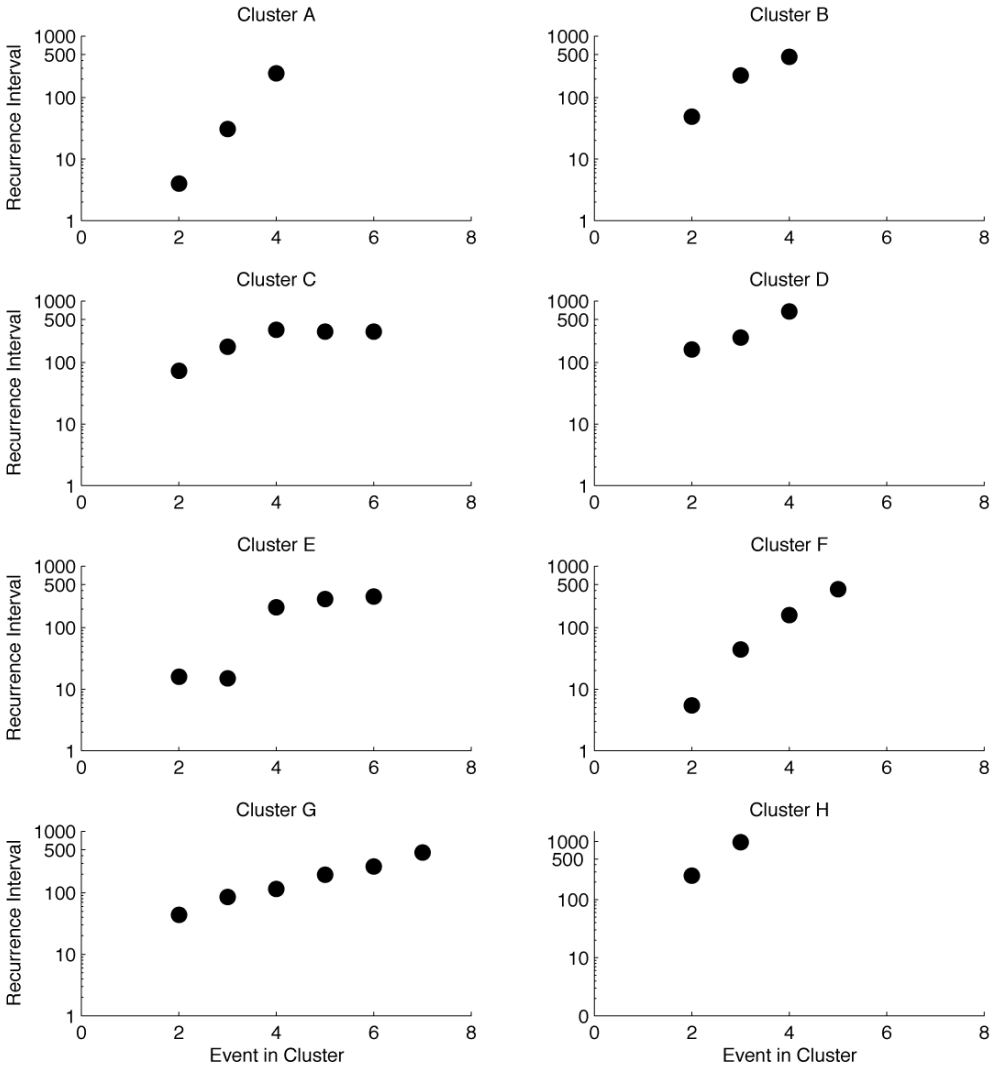

Figure **3-3**: Recurrence time trends for repeating clusters. Most clusters show an increase in recurrence time while others develop a quasi-periodic recurrence time.

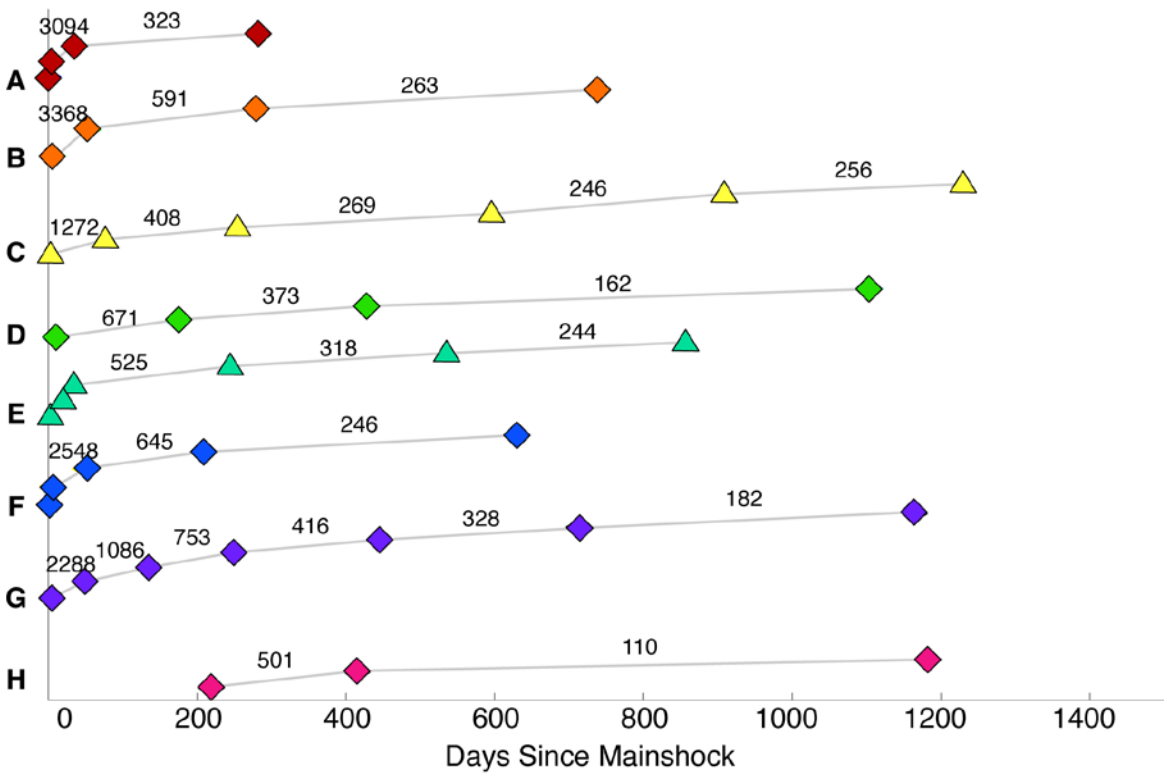

Figure **3-4**: The slip on each cluster since the mainshock as estimated by an assumed shear modulus of 40 GPa and an area calculated from using a constant stress drop of 10 MPa. Most clusters show about 0.5-1 m of slip. We show two behavior types, one with increasing recurrence interval, (diamonds) the other with a developing quasi-periodic trend (triangles). Numbers between events show the slip rate for a given cluster for that recurrence interval in mm/yr.

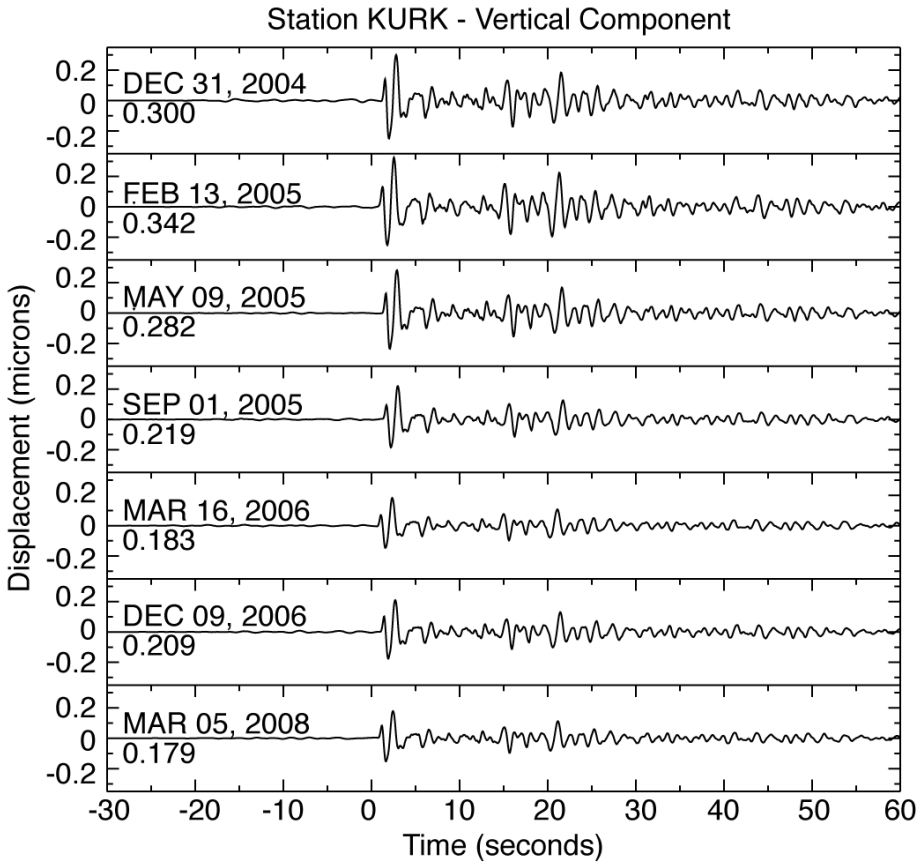

Figure **3-5**: An example of the vertical component of a filtered waveform cluster (Cluster G) as recorded at station KURK. Waveforms are cut 10 seconds before the direct P-wave arrival and 60 seconds. The date of the event is shown above each waveform, below the date is the maximum amplitude in microns.

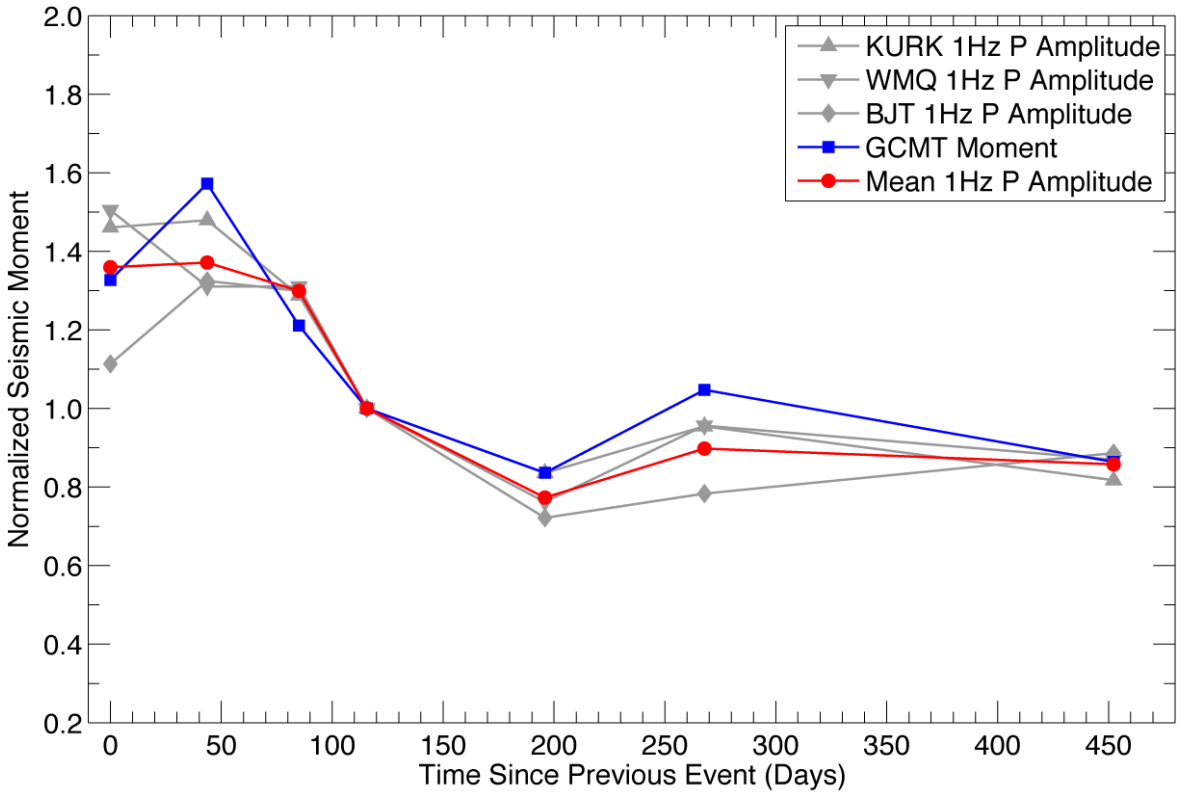

Figure **3-6**: Normalized amplitudes for cluster G from observed P waves and the GCMT catalog. Gray lines identify the observed P waveform peak amplitudes, the red line is the average of the values from the three stations for each event. The blue line is a plot of the normalized GCMT seismic moments. All curves were normalized using the values for the fourth event in the sequence.

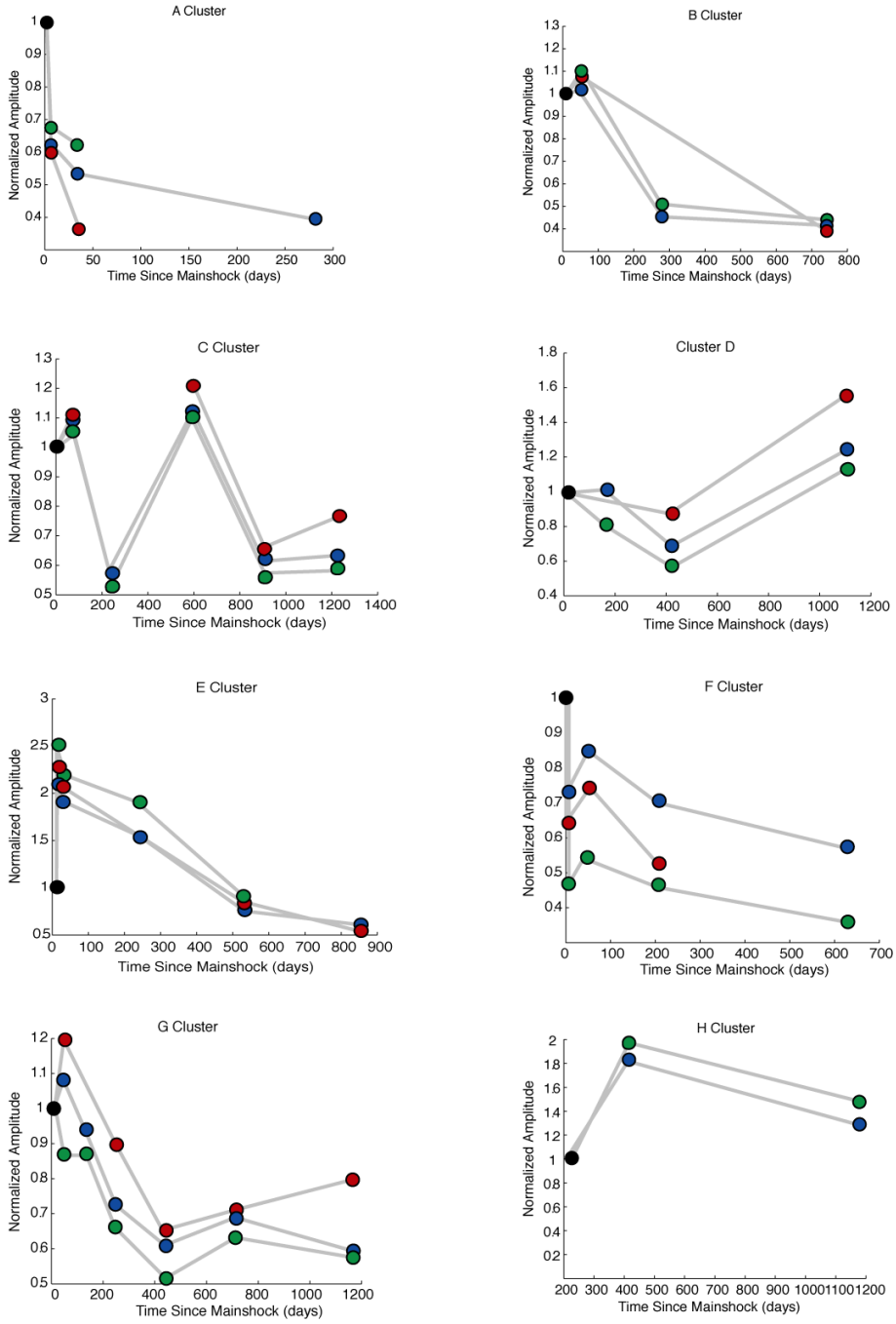

Figure **3-7**: A summary of normalized amplitudes for each cluster following the mainshock. Amplitudes recorded at BJT are red, KURK blue, and WMQ green. Most show a systematic decrease, which we attribute to a fault strength change, while smaller variations may indicate slight changes in focal mechanism (rake).

Chapter 4

Discussions and Conclusions

The observed repeating event patterns can be explained in a number of ways. The temporal behavior generally follows the expected patterns – a logarithmic variation in recurrence interval. Two of the three clusters deep beneath the northern boundary of the Aceh Basin show varying responses – Cluster E experiences an increase in recurrence interval after two events, suggesting a step like change in loading rate – but and the onset of a steady decrease in seismic moment that indicates a systematic physical change in a weaker asperity (either a reduction in strength or area). Nearby cluster C shows a leveling off of the recurrence interval after two events, and a variable seismic moment, that ultimately results in a weaker asperity.

Until now we have continued under the assumption that the asperity stress drop lies in the range from 1 to 10 MPa. Each stress drop corresponds to a particular fault area, which when combined with the seismic moment allows us to estimate the earthquake slip. We can test the observed fault slips for consistency with the "brittle creep" afterslip model of Perfettini and Avouc (2004a, 2004b). In the model, the slip as a function of time, *U(t)*, on the creeping fault follows a relatively simple form given by:

$$U(t) = V_0 t_r \ln\left[1 + \frac{V_+}{V_0}\left(\exp(t/t_r) - 1\right)\right] \tag{4.1}$$

Where t is time, V_0 is the background plate motion (assumed to be 63 mm/yr); t_r is a relaxation time for the creep process, V_+ is the initial creep rate immediately following the mainshock that drives the postseismic response. We can fit the equation to our cumulative slip estimates for our range of stress drops – an example is shown in Figure 3-8. The values for V+ and tr in the 10 MPa model are 11 m/yr and 252 days respectively. Chleih et al (2007) estimated similar fits to

surface GPS observations and found a slightly lower (92 day) relaxation time. The afterslip model clearly favors a high, though not unreasonable stress drop for the events. Similar calculations for each cluster show that in general all the events are consistent with the afterslip model and all are also consistent with the high stress drop, although some are also consistent with lower stress drop models (Appendix C).

We are not the first to observed a decrease in seismic moment with increasing recurrence time in repeating earthquake sequences. Peng et al (2005) observed similar results in aftershocks of the 1984 Morgan Hill earthquake. A number of factors could produce the decrease in moment with repeated events. For example, if the asperity retains a roughness component at these depths, the roughness could be reduced by successive events as geometric features are broken during the high stress drop events. Although we have interpreted the decrease as a reduction in the intrinsic strength (and hence a reduction in slip), a decrease in area caused by accumulating slip, increase temperature, or fluids could also reduce the amplitude of seismic waves radiating from the source region. We seek to determine a mechanism for moment decrease examining a compositional change or fault strength change.

Fault weakening could be accommodated compositionally by the negative healing properties of talc (C. Marone, personal communication). The conditions that produce zero to negative fault healing rates are observed in laboratory measurements in some phyllosilicates. Materials such as talc do not show typical fault healing rates as suggested in Marone, 1998. The widespread presence of talc in a subduction zone is possible due to the presence of siliceous material in the subducting sediments. The down-dip limit of the seismogenic zone is believed to be controlled by either a thermal limit or the depth of serpentinization (e.g. Moore et al., 1997). The isotherms corresponding to the depths of Aceh Basin aftershocks are in the range that would imply the plate boundary rheology is controlled by the downgoing quartz-feldspathic sediments (Chlieh et al., 2007). Serpentinite generally indicates aseismic behavior, but under certain

conditions such as temperatures higher than ~200° C (Moore et al., 1997) or high strain rates (Hyndman, et al. 1997) it can exhibit stable sliding.

The subducting oceanic plate carries with it water, which interacts with the overlying mantle wedge (Figure 3-9). Assuming the fluids in these reactions are derived from the subducting slab, we obtain the following reactions: Equation 4.2 and once olivine is exhausted, Equation 4.3 (Bailey and Holloway, 2000).

$$3\,Olivine + 2H_2O + 5\,Silica = 2\,Talc \tag{4.2}$$

$$3\,Orthopyroxene + H_2O + Silicia_{(aq)} = Talc \tag{4.3}$$

The megathrust would have significantly affected the region, opening more fractures throughout the rupture area. These fractures could aid in fluid flow to the mantle wedge, increasing the production of phyllosilicates from the above reactions.

We can also account for a change in fault strength by changing parameters associated with the formula for seismic moment. Until this point, we have assumed the area of the asperities is constant; we can examine a change in the area using the corner frequency of the earthquake spectra. The expected change in corner frequency for a 50% reduction in size (as observed in cluster G) would produce a 0.2 Hz shift. This change is too minute to be observable in our spectra (Figure 2-7). Although we are unable to provide direct evidence, we expect the area may change slightly.

Another possibility, transient embrittlement, was mentioned by Peng et al. (2005) to explain the trend seen in a study of repeating earthquakes on the Calaveras fault following the 1984 M_w 6.2 Morgan Hill earthquake. The study of the Calaveras fault showed the aftershock productivity falling off as an expected 1/time relation. Many clusters demonstrate a direct relationship between recurrence time and moment release; however, other clusters showed an inverse relation. The authors propose the Morgan Hill mainshock acted to increase the strain rate

in the region, allowing for a process of transient embrittlement, strengthening the surrounding fault area. This is supported by the proximity of the negative or constant healing clusters to areas near the mainshock. The process of transient embrittlement changes the strength of the fault, allowing for a larger moment release that will lessen with time as the strain rate also decreases.

The clusters beneath the Aceh Basin loosely relate to the Morgan Hill aftershocks observed by Peng, et al. (2005). Although the Aceh aftershocks are low-angle thrust events and they show an increasing recurrence interval, yet a decreasing moment. In spite of this similarity, there does not appear to be a break in cluster behaviors at a certain depth, as observed in the Calaveras study.

Transient embrittlement is a measure of the change of a-b parameter from velocity strengthening (positive) to velocity weakening (negative). This can be accomplished by a change in velocity or a change in the critical slip distance. An increase in shear strain lowers the critical slip distance (D_c) in lab experiments (Marone and Kilgore, 1993) for D_c values on the order of 10^{-5} m. This change can be determined experiments; however, we qualify the impression of transient embrittlement by the perceived effect on seismicity.

We favor a mechanism that incorporates an area decrease into the transient embrittlement hypothesis. The 2004 earthquake provided an increase in strain rate to the Sunda region. This increase in strain rate embrittled aseismic regions on the fault, allowing them to fail seismically, effectively increasing their area. As the initial increase in strain rate decayed with time, smaller areas of the asperity were able to fail seismically, decreasing the total available rupture area. This change in area is responsible for the observed decrease in peak P-wave amplitude (seismic moment). The model suggests with the decrease in strain rate (and associated decrease in area) that cluster activity will decrease below our threshold of observation. With the roughly logarithmic recurrence interval of our repeating clusters, we would predict some clusters (A, B, and F, Figure 3-4) to have another event. It is possible that these asperities are no longer

supported by the strain rate necessary for failures that produce detectable and correlatable sized events (~M_w< 4.8).

The idea of a transient embrittlement induced by the mainshock is further supported by the lack of correlating events prior to the 2004 earthquake. Of the roughly 60 recorded moderate-size events from the time of instrumentation (Table 2-1) to the 2004 earthquake, none correlate with any established cluster or doublet, even at a lowered threshold of 0.90 correlation. This evidence corroborates the idea the mainshock in 2004 played a major role in increasing the stain rate of the region. Additionally, our preserved decay of cluster activity might be a sign of a decaying strain rate.

Summary and Conclusions

The asperities beneath the Aceh Basin are ~1-3 km in radius and produce moderate size events. At a given asperity, we observe an expected logarithmic increase in recurrence interval, as would be consistent with an afterslip model. Although the recurrence intervals continue to increase, most clusters release progressively smaller moments, contrary to basic understanding of rock mechanics.

From a seismological perspective, we have shown that moderate-size repeating earthquakes are clearly identifiable with teleseismic and regional seismic data. Thus, opportunities exist to study repeating events on remote fault systems. Although the teleseismic have limited high-frequency content, they appear capable of constraining locations of moderate-size events to less than a kilometer.

The observations also clearly show that the isolated asperities deep in the seismogenic zone evolve rapidly (at least perceptively) over a few seismic cycles. Whether the evolution is an

erosion of the asperity or a change in intrinsic asperity strength remains an open question. The decrease in moment of about 25-50% suggests that the process occurs very fast. Perhaps future experimental work, or observations recorded closer that have a wider bandwidth from and event such as the 2010 Chile earthquake will provide the resolution needed to distinguish between the models.

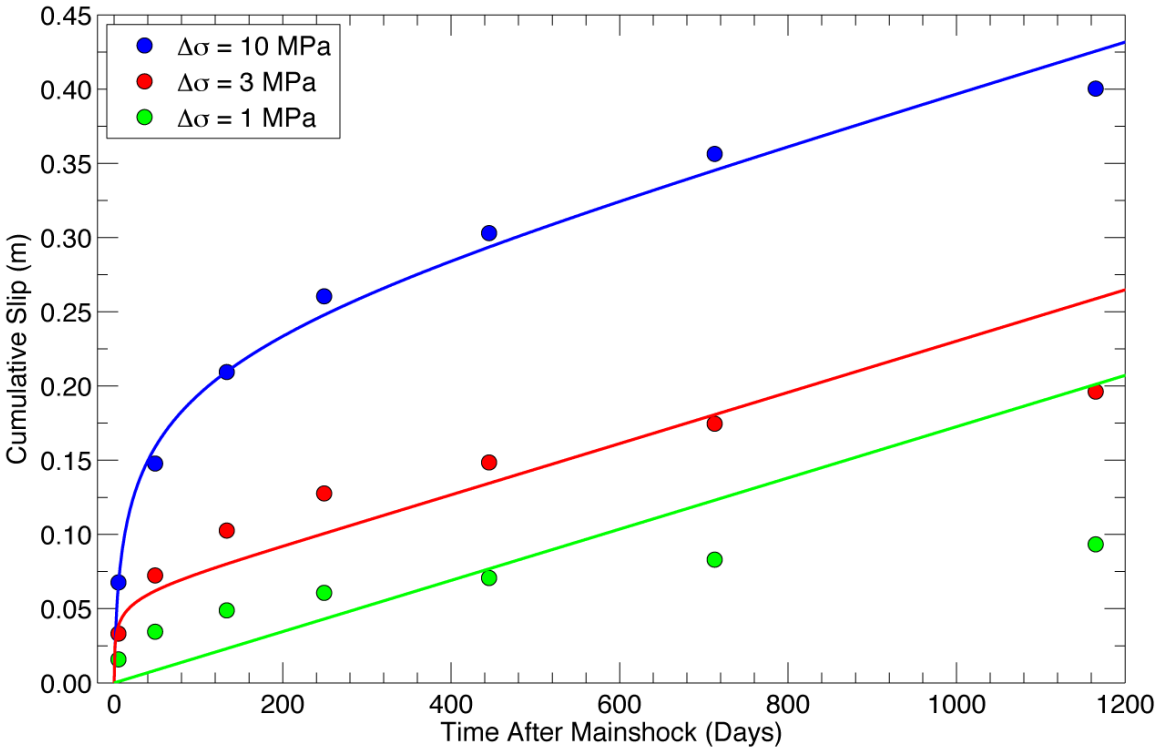

Figure **4-1**: Sample fit of the afterslip model of Perfettini and Avouac (2004a, 2004b) to the cumulative slip curves. Only the high stress-drop candidate fits the observations

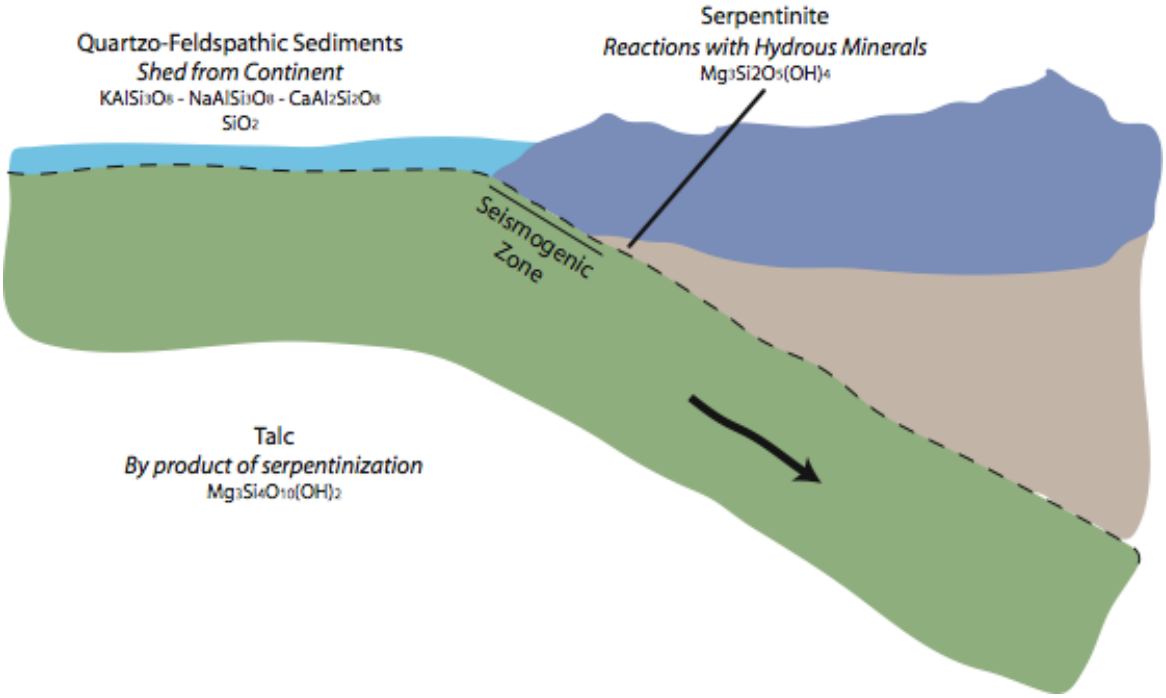

Figure **4-2**: A schematic diagram explaining talc producing reactions as they might occur in a subduction zone. Quartzo-feldspathic sediments are shed from the continent and carried down with the subducting oceanic plate. Hydrous minerals allow for the serpentinization of the overlying mantle. The reactions between the down-going sediments and serpentinized mantle can produce phyllosilicates, such as talc

References

Ammon, C. J., C. Ji, H.K. Thio, D. Robinson, S. Ni, V. Hjorleifsdottir, H. Kanamori, T. Lay, S. Das, D. Helmberger, G. Ichinose, J. Polet, and D. Wald (2005). Rupture process of the 2004 Sumatra-Andaman earthquake, *Science* **308,** 1133-1139.

Araki, E., M. Shinohara, K. Obana, T. Yamada, Y. Kaneda, T. Kanazawa, and K. Suyehiro (2006). Aftershock distribution of the 26 December 2004 Sumatra-Andaman earthquake from ocean bottom seismographic observation, *Earth Planets Space*, **58**, 113-119.

Bailey, E. and J.R. Holloway (2000). Experimental determination of elastic properties of talc to 800 degrees C, 0.5 GPa; calculations on the effect of hydrated peridotite, and implications for cold subduction zones, *Earth and Planetary Science Letters*, **183**, 487-498.

Bakun, W.H. and McEvilly, T.V. (1984). Recurrence models and Parkfield, California, earthquakes, *Journal of Geophysical Research*, 89 (B5), 3051-3058.

Barrett, S. A., Teleseismic Relocation of Aftershock Events beneath the Aceh Basin, Northern Sumatra, B. S. Thesis, Department of Geosciences, The Pennsylvania State University, University Park, PA, 2009.

Berglar, K., Gaedicke, C., Lutz, R., Franke, D., and Y.S. Djajadihardja (2008). Neogene subsidence and stratigraphy of the Simeulue forearc basin, Northwest Sumatra, *Marine Geology*, **253**, 1-13.

Bilek, S.L, Satake, K., and K. Sieh (2007). Introduction to the special issue on the 2004 Sumatra-Andaman earthquake and the Indian Ocean tsunami, *Bulletin of the Seismological Society of America*, **97**, (1A), S1-S5.

Bilham, R., Engdahl, R., Feldl, N., Satyabala, S. P., (2005). Partial and complete rupture of the Indo-Andaman plate boundary 1847-2004, *Seism. Res. Letters*, **76**: 299-311.

Bock, Y., L. Prawirodirdjo, J. F. Genrich, C. W. Stevens, R. McCaffrey, C. Subarya, S. S. O. Puntodewo, and E. Calais (2003). Crustal motion in Indonesia from Global Positioning System measurements, *Journal of Geophysical Research,* **108** (B8), 2367.

Cande, S.C., and D.V. Kent (1995). Revised calibration of the geomagnetic polarity timescale for the Late Cretaceous and Cenozoic, *Journal of Geophysical Research*, **100**, (B4), 6093-6095.

Chen, T. and N. Lapusta (2009). Scaling of small repeating earthquakes explained by interaction of seismic and aseismic slip in a rate and state fault model, *Journal of Geophysical Research,* **114,** B01311.

Chlieh, M., Avouac, J.P., Hjorleifsdottir, V., Song, T.A., Ji, C., Sieh, K., Sladen, A., Hebert, H., Prawirodirdjo, L., Bock, Y. and J. Galetzka (2007). Coseismic slip and afterslip of the Great M_w 9.15 Sumatra-Andaman Earthquake of 2004, *Bulletin of the Seismological Society of America*, **97**, (1A), S152-S173.

DeMets, C., Gordon, R.G., and Argus, D.F., (2010). Geologically current plate motions, *Geophysical Journal International*, **181**, 1-80.

DeMets, C., Gordon, R.G., Argus, D.F., and S. Setin (1990). Current plate motions. *Geophysical Journal International* **101,** 425-478.

Engdahl, R., A. Villasenor, H.R. DeShon, and C.H. Thurber (2007). Teleseismic relocation and assessment of seismicity (1918-2005) in the region of the 2004 M_w 9.0 Sumatra-Andaman and 2005 M_w 8.6 Nias Island Great Earthquakes, *Bulletin of the Seismological Society of America,* **97,** (1A), S43-S61.

Hayes, G. and D. Wald, (2009). Developing framework to constrain the geometry of the seismic rupture plane on subduction interfaces a priori - a probabilistic approach, *Geophysics Journal International,* **176**, (52) 951-964.

Hyndman, R.D., M. Yamano, D.A. Oleskevich, (1997). The seismogenic zone of subduction thrust faults. *Island Arc*, **6** (3), 244-260.

Igarashi, T., T. Matsuzawa and A. Hasegawa (2003). Repeating earthquakes and interplate aseismic slip in the northeastern Japan subduction zone, *Journal of Geophysical Research,* **108,** (B5) 2249-2258.

Kanamori, H. and D.L. Anderson (1975). Theoretical Basis of Some Empirical Relations in Seismology, *Bulletin of the Seismological Society of America*, **65**, (5) 1073-1095.

Katili, J., (1975). Volcanism and plate tectonics in the Indonesian island arcs, *Tectonophysics*, **26**, 165-188.

Katili, J., (1973). Geochronology of West Indonesia and its implications on plate tectonics, *Tectonophysics*, **19**, 195-212.

Kimura, H., K. Kasahara, T. Igarashi, and N. Hirata. (2006). Repeating earthquake activities associated with the Philippine Sea plate subduction in the Kanto district, central Japan: A new plate configuration revealed by interplate aseismic slips, *Tectonophysics* **417,** 101-118.

Konca, A.O., J. Avouac, A. Sladen, A.J. Meltzner, K. Sieh, P. Fang, Z. Li, J. Galetzka, J. Genrich, M. Chlieh, D.H. Natawidjaja, Y. Bock, E.J. Fielding, C. Ji, and D. Helmberger (2008). Partial rupture of a locked patch of the Sumatra megathrust during the 2007 earthquake sequence *Nature* **456,** 631-634.

Konca, A.O., Hjorleifsdottir, V., Song, T.A., Avouac, J.P., Helmberger, D.V., Ji, C., Sieh, K., Briggs, R. and A. Meltzner (2007). Rupture kinematics of the 2005 M_w 8.6 Nias-Simeulue earthquake from the join inversion of seismic and geodetic data, *Bulletin of the Seismological Society of America*, **97**, (1A), S307-S322.

Lay, T., H. Kanamori, C. Ammon, M. Nettles, S. Ward, R.Aster, S. Beck, S. Bilek, M. Brudzinski, R. Butler, H. DeShon, G. Ekstrom, K. Satake, and S. Sipkin (2005). The Great Sumatra-Andaman earthquake of 26 December 2004, *Science* **308,** 1127-1132.

Maceira, M., C. A. Rowe, G. Beroza, and D. Anderson (2010), Identification of low-frequency earthquakes in non-volcanic tremor using the subspace detector method, *Geophysical Research Letters*, **37**, L06303, doi:10.1029/2009GL041876.

Malservisi, R., K. P. Furlong, and C. Gans (2005). Microseismicity and creeping faults: Hints from modeling the Hayward fault, California (USA). *Earth Planet Sci Lett.*, **234** (3-4), 421-435

Marone, C. (1998). Laboratory-derived friction laws and their application to seismic faulting, *Annual Review of Earth and Planetary Sciences*, **26**, 643-696.

Marone, C. and Kilgore, B. (1993). Scaling of the critical slip distance for seismic faulting with shear strain in the fault zone, *Nature*, **362**, 618-621.

Megawati, K. and T.C. Pan (2009). Regional seismic hazard posed by the Mentawai segment of the Sumatran megathrust, *Bulletin of the Seismological Society of America*, **99**, (2A), 566-584.

Molnar, P. and P. Tapponnier (1975). Cenozoic tectonics of Asia: effects of a continental collision, *Science* **189**, 419-426.

Moore, D. E., Lockner, D.A., Shengli, M., Summers, R., and J.D. Byerlee (1997). Strengths of serpentinite gouges at elevated temperatures, *Journal of Geophysical Research*, **102**, (14), 14,787-14,801.

Mosher, D.C., J.A. Austin Jr., D. Fisher, and S.P.S. Gulick (2008). Deformation of the northern Sumatra accretionary prism from high-resolution seismic reflection profiles and ROV observations, *Marine Geology*, **252**, (3-4), 89-99.

Nadeau, R.M. and L.R. Johnson (1998). Seismological studies at Parkfield VI: Moment release rates and estimates of source parameters for small repeating earthquakes, *Bulletin of the Seismological Society of America*, **88,** (3) 790-814.

Nadeau, R.M. and T.V. McEvilly (1999). Fault slip rates at depth from recurrence intervals of repeating microearthquakes, *Science*, **285**, 718-721.

Natawidjaja, D.H., Sieh, K., Chlieh, M., Galetzka, J., Suwargardi, B.W., Cheng, H., Edwards, R.L., Avouac, J.P., and S.N. Ward (2006). Source parameters of the great Sumatran megathrust earthquakes of 1797 and 1833 inferred from coral microatlls, *Journal of Geophysical Research,* **111**, (B6), 37.

Owens, T.J., Crotwell, H.P, Groves, C. and P. Oliver-Paul (2004). SOD: Standing Order for Data, *Seismological Research Letters*, **75**, 515-520.

Perfettini, H., and J.-P. Avouac (2004a). Postseismic relaxation driven by brittle creep: a possible mechanism to reconcile geodetic measurements and the decay rate of aftershocks, application to the Chi-Chi earthquake, Taiwan, *J. Geophys. Res.***109 ,** B02304, doi10.1029/2003JB002488 .

Perfettini, H., and J.-P. Avouac (2004b). Stress transfer and strain rate variations during the seismic cycle, *J. Geophys. Res.***109 ,** B06402, doi 10.1029/2003JB00291.

Reid, H.F. (1910). *The California Earthquake of April 18, 1906, Report of the State Earthquake Investigation Commission, V. II.* Carnegie Institution, Washington, D.C. 192.

Scholz, C.H., *The Mechanics of Earthquakes and Faulting*, 2nd edition, Cambridge, 2002.

Scotese, C.R.,L.M. Gahagan, R.L. Larson (1988). Plate tectonic reconstruction of the Cretaceous and Cenozoic ocean basins, *Tectonophysics*, **155**, 27-48.

Seeber, L., C. Mueller, T. Fujiwara, K. Arai, W. Soh, Y.S. Djajadihardja, and M.H. Cormier (2007). Accretion, mass wasting, and partitioned strain over the 26 Dec 2004 M_w 9.2 rupture offshore Aceh, northern Sumatra, *Earth and Planetary Science Letters*, **263,** 16-31.

Shimazaki, K. and T. Nakata (1980). Time-predictable recurrence model for large earthquakes, *Geophysical Research Letters*, **7**, 279*-82.

Sieh, K, Natawidjaja, D.H., Meltzner, A.J., Shen, C., Cheng, H., Li, K., Suwargadi, B.W., Galetzka, J., Philibosian, B., and R.L. Lawrence (2008). Earthquake supercycles inferred from sea-level changes recorded in the corals of west Sumatra, *Science*, **322**, (5908), 1674-1678.

Socquet, A., C. Vigny, N. Chamot-Rooke, W. Simons, C. Rangin, and B. Ambrosius (2006). India and Sunda plates motion and deformation along their boundary in Myanmar determined by GPS, *Journal of Geophysical Research*, **111**, B05406.

Susilohadi, S., C. Gaedicke, and A. Ehrhardt (2005). Neogene structures and sedimentation history along the Sunda forearc basins off southwest Sumatra and southwest Java. Marine Geology **219**, 133-154.

Templeton, D.C., Nadeau, R.M., and R. Burgmann (2008). Behavior of Repeating Earthquake Sequences in Central California and the Implications for Subsurface Fault Creep, *Bulletin of the Seismological Society of America*, **98**, (1) 52-65.

Vita-Finzi, C (2007). Neotectonics and the 2004 and 2005 earthquake sequences at Sumatra, *Marine Geology*, **248**, 47-52.

Appendix A: GMT Focal Mechanisms of Aceh Events

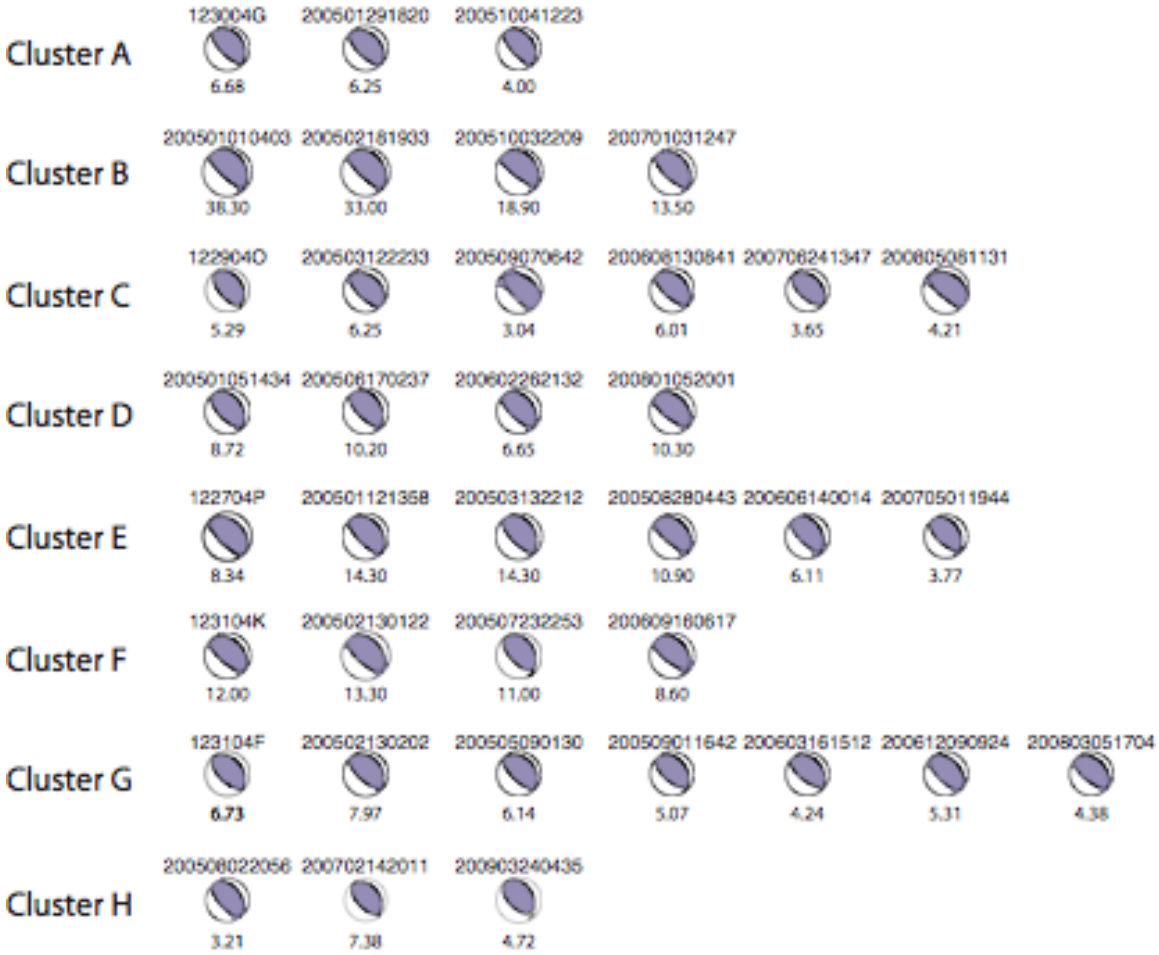

GCMT focal mechanism for each clustering event. The event name (date) appears above the focal mechanism. The moment (scaled by 10^{23} dyne cm) is listed below the focal mechanism. We believe the slight variation in the focal mechanism is within the margin of error.

Appendix B: Cluster Waveforms

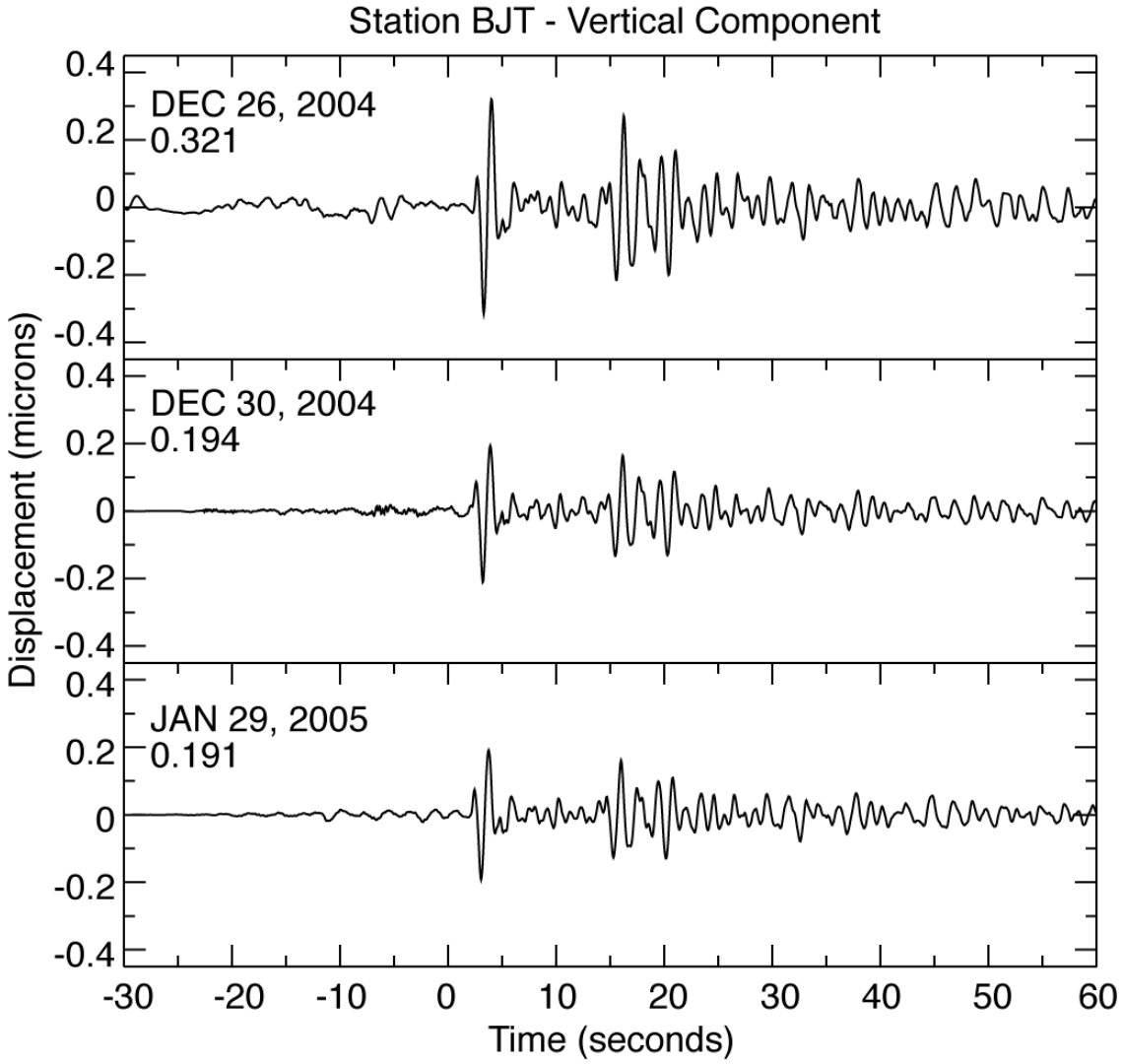

Waveforms of the vertical component for Cluster A as recorded at station BJT. Waveforms show displacement (in microns) from 30 seconds prior to the arrival of the P-wave to 60 seconds following. The date of the event is shown in the upper left corner of each waveform. The peak P-wave amplitude is recorded below the date.

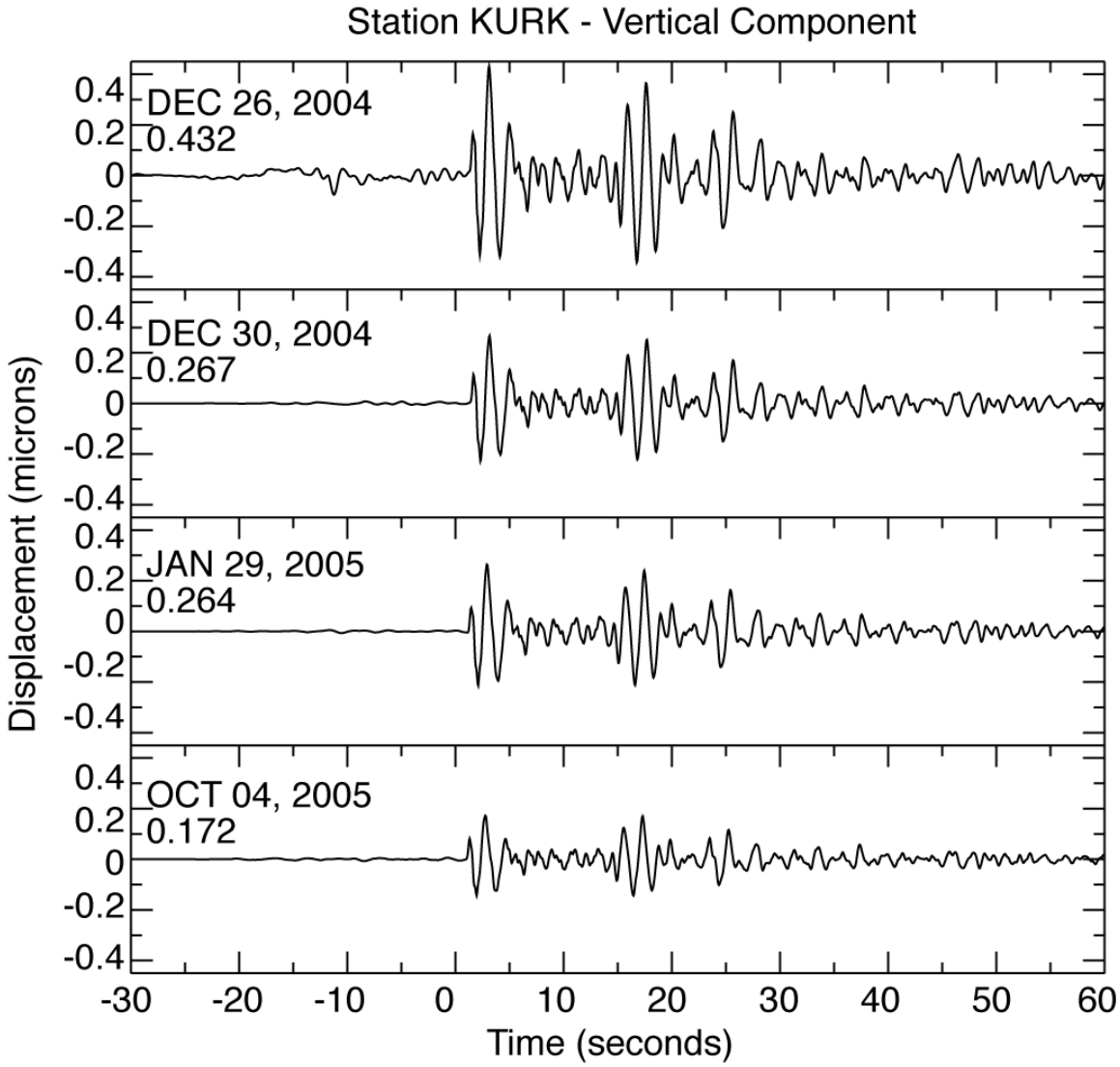

Waveforms of the vertical component for Cluster A as recorded at station KURK. Waveforms show displacement (in microns) from 30 seconds prior to the arrival of the P-wave to 60 seconds following. The date of the event is shown in the upper left corner of each waveform. The peak P-wave amplitude is recorded below the date.

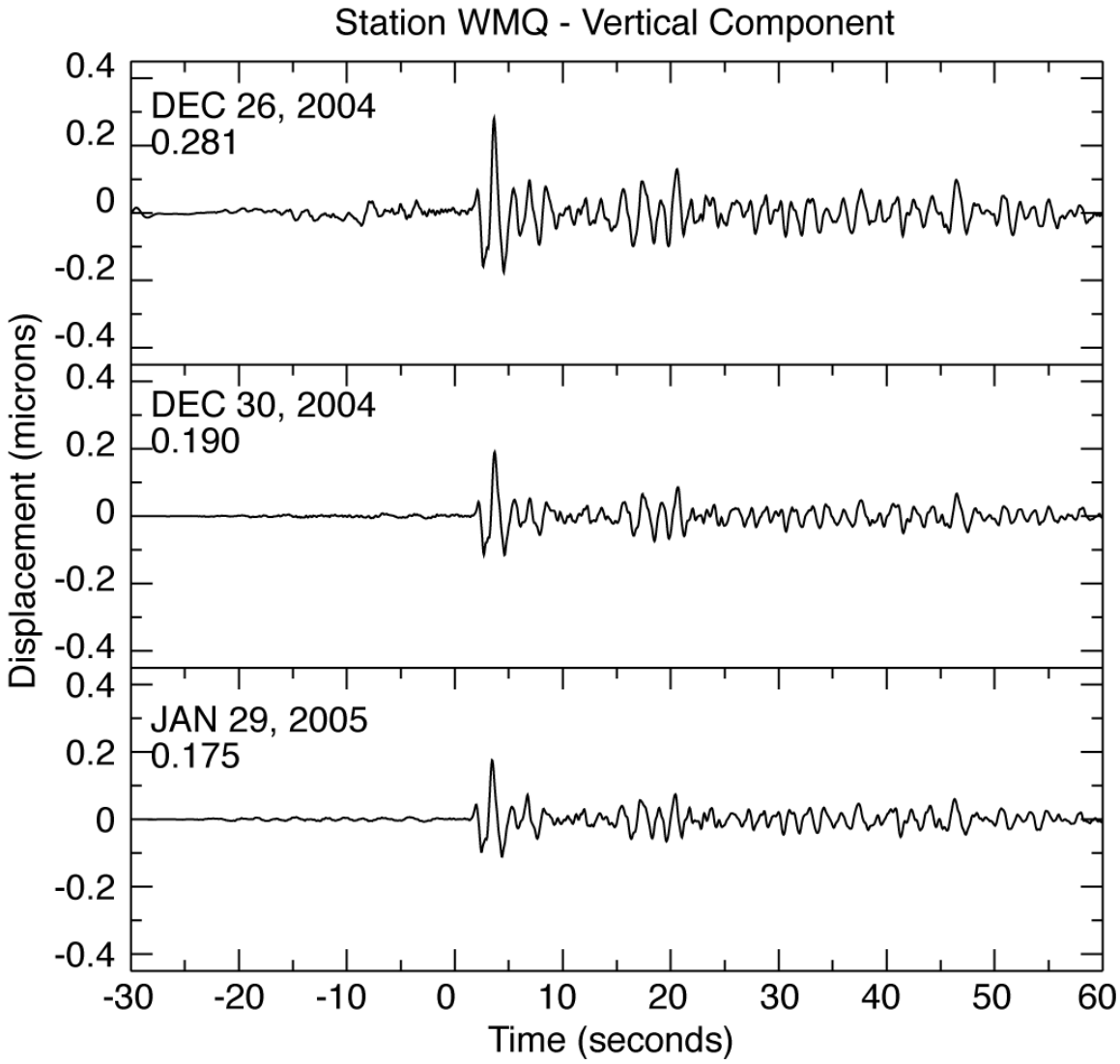

Waveforms of the vertical component for Cluster A as recorded at station WMQ. Waveforms show displacement (in microns) from 30 seconds prior to the arrival of the P-wave to 60 seconds following. The date of the event is shown in the upper left corner of each waveform. The peak P-wave amplitude is recorded below the date.

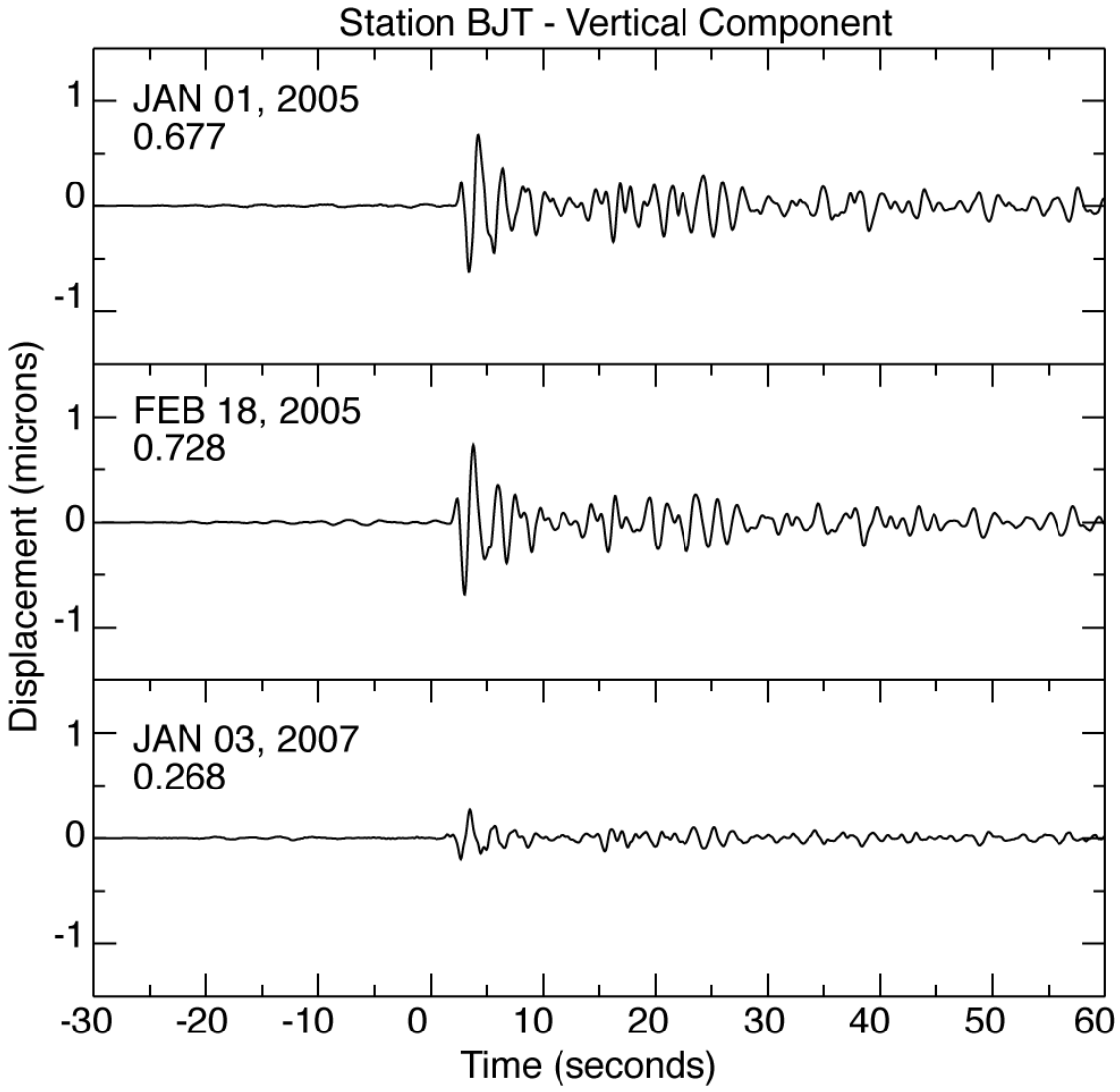

Waveforms of the vertical component for Cluster B as recorded at station BJT. Waveforms show displacement (in microns) from 30 seconds prior to the arrival of the P-wave to 60 seconds following. The date of the event is shown in the upper left corner of each waveform. The peak P-wave amplitude is recorded below the date.

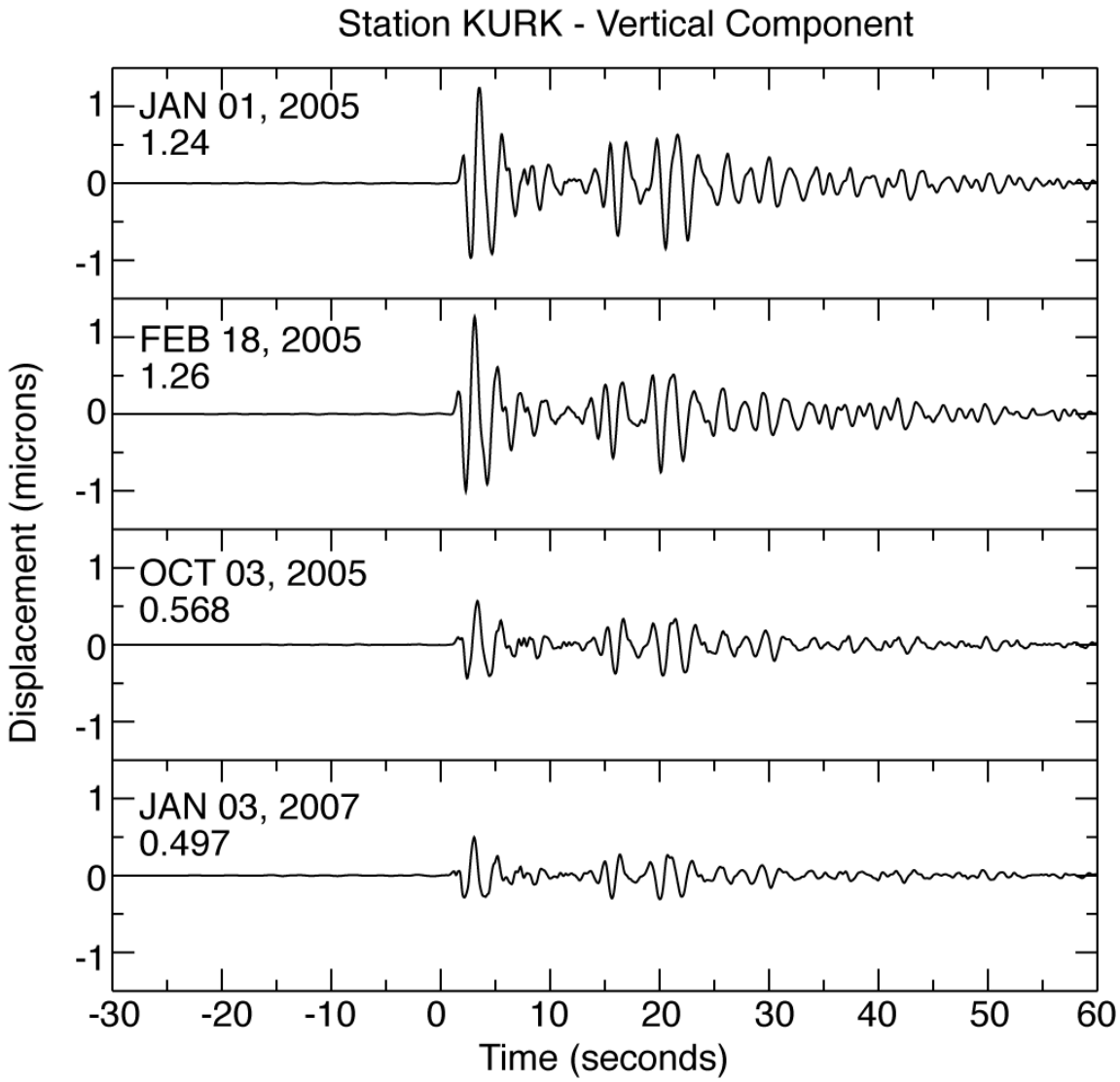

Waveforms of the vertical component for Cluster B as recorded at station KURK. Waveforms show displacement (in microns) from 30 seconds prior to the arrival of the P-wave to 60 seconds following. The date of the event is shown in the upper left corner of each waveform. The peak P-wave amplitude is recorded below the date.

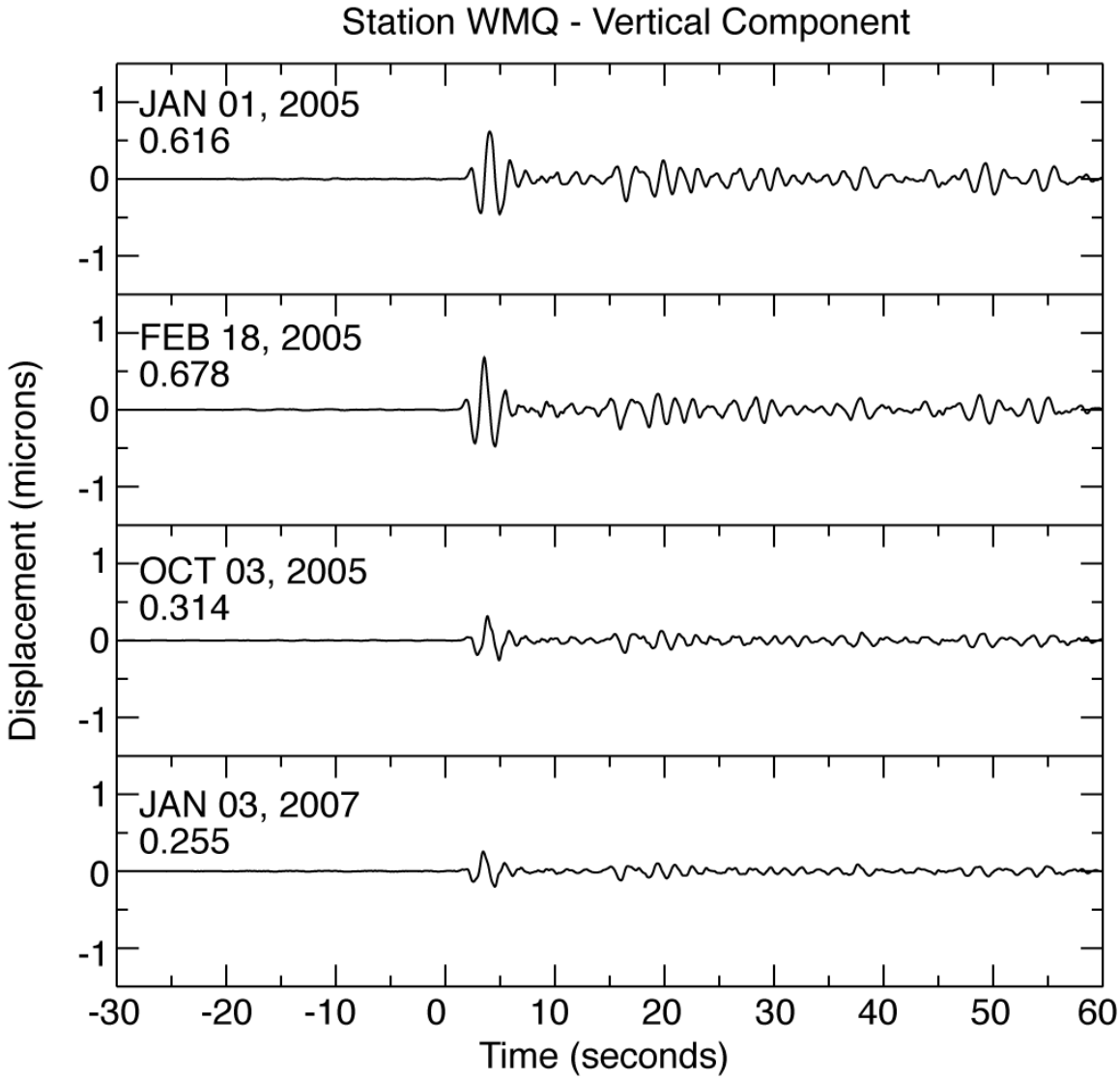

Waveforms of the vertical component for Cluster B as recorded at station WMQ. Waveforms show displacement (in microns) from 30 seconds prior to the arrival of the P-wave to 60 seconds following. The date of the event is shown in the upper left corner of each waveform. The peak P-wave amplitude is recorded below the date.

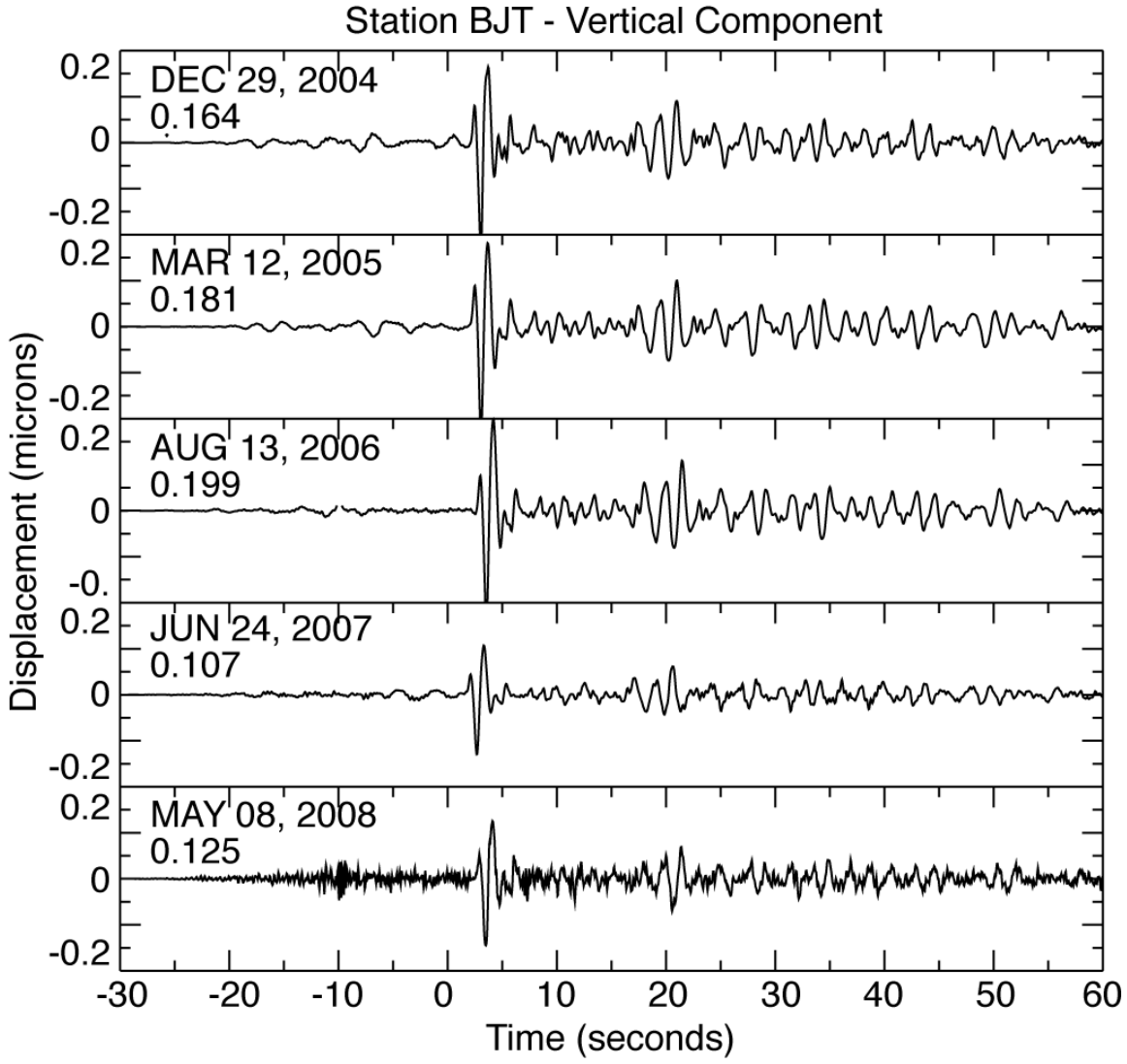

Waveforms of the vertical component for Cluster C as recorded at station BJT. Waveforms show displacement (in microns) from 30 seconds prior to the arrival of the P-wave to 60 seconds following. The date of the event is shown in the upper left corner of each waveform. The peak P-wave amplitude is recorded below the date.

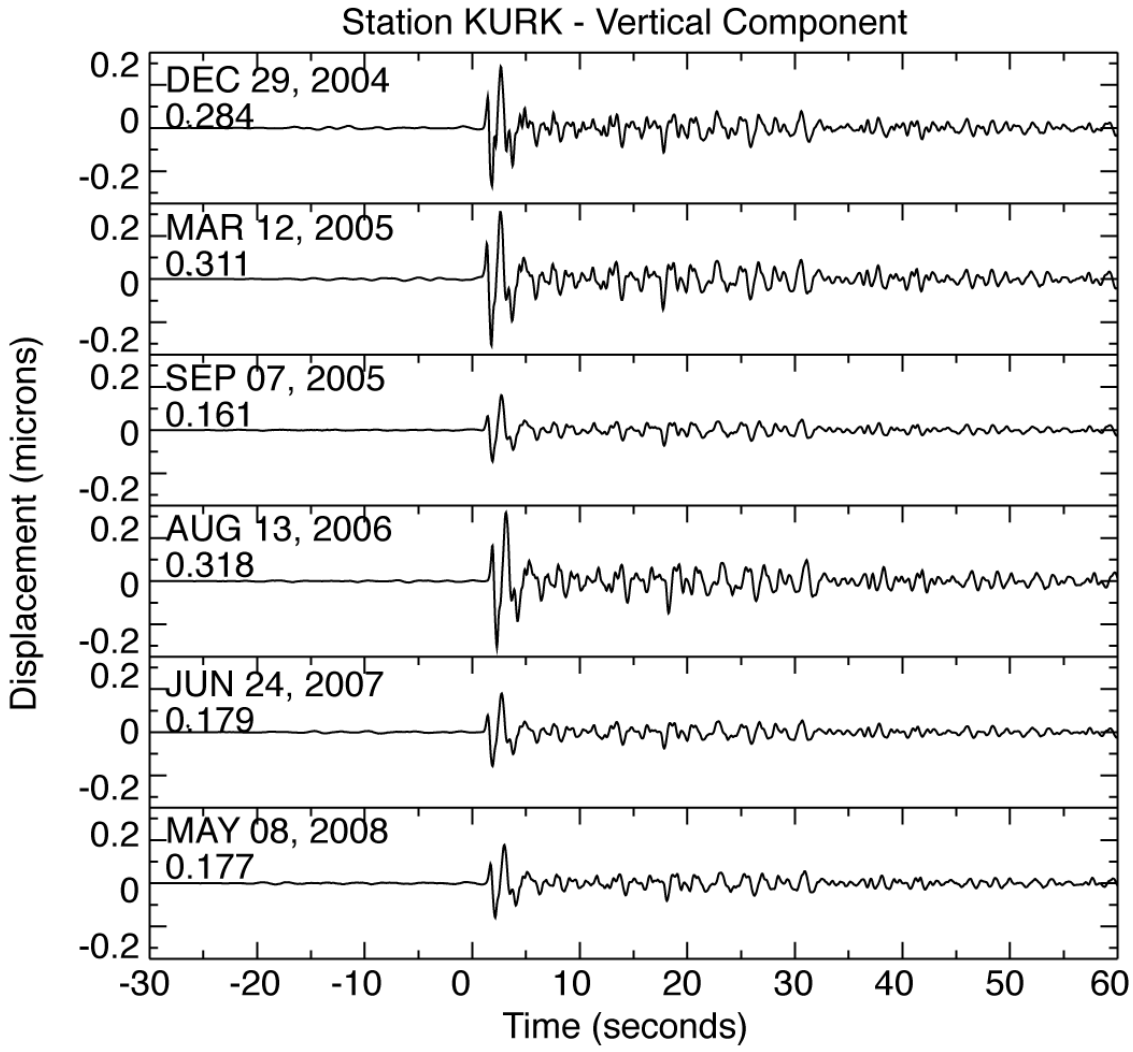

Waveforms of the vertical component for Cluster C as recorded at station KURK. Waveforms show displacement (in microns) from 30 seconds prior to the arrival of the P-wave to 60 seconds following. The date of the event is shown in the upper left corner of each waveform. The peak P-wave amplitude is recorded below the date.

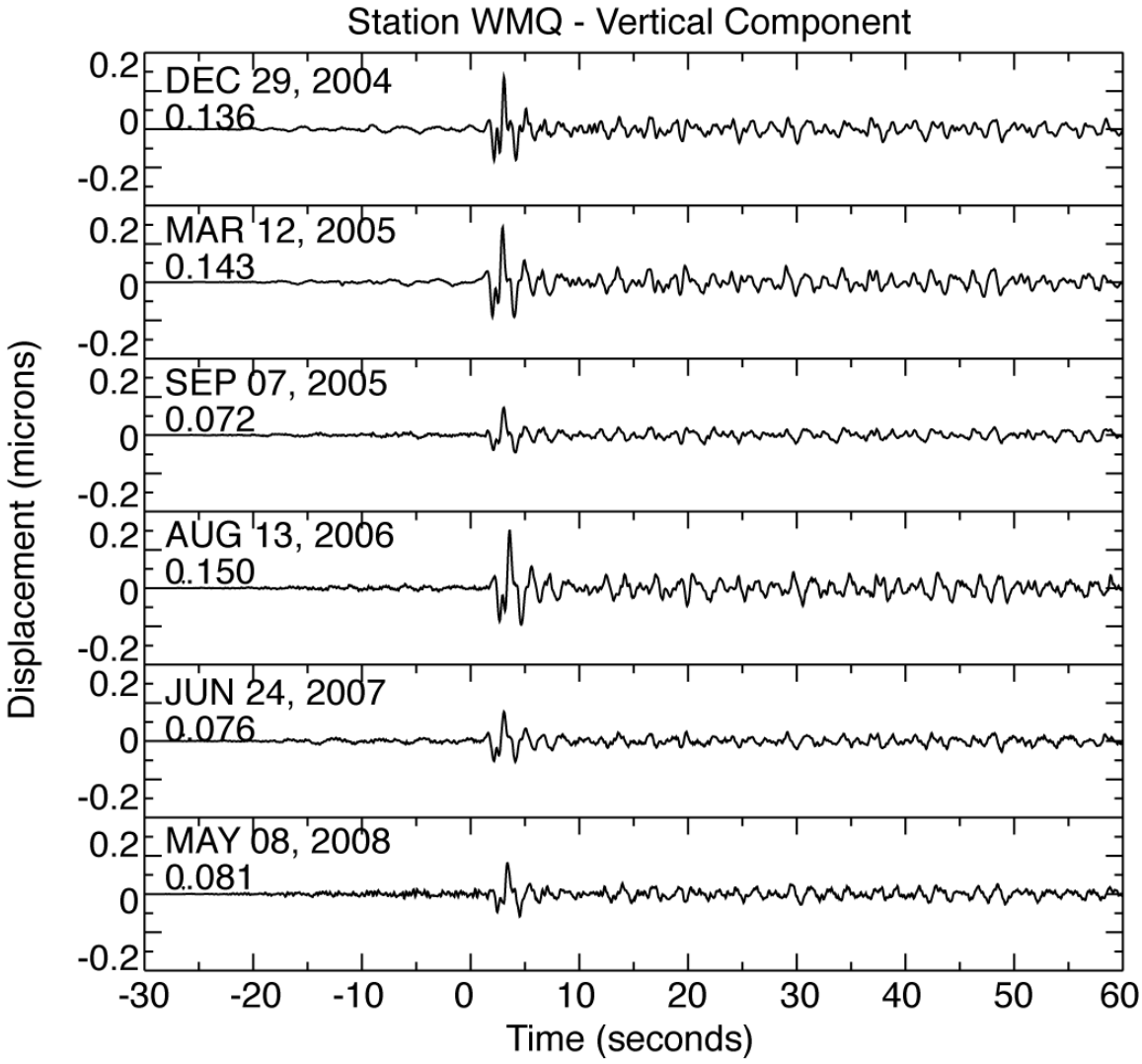

Waveforms of the vertical component for Cluster C as recorded at station WMQ. Waveforms show displacement (in microns) from 30 seconds prior to the arrival of the P-wave to 60 seconds following. The date of the event is shown in the upper left corner of each waveform. The peak P-wave amplitude is recorded below the date.

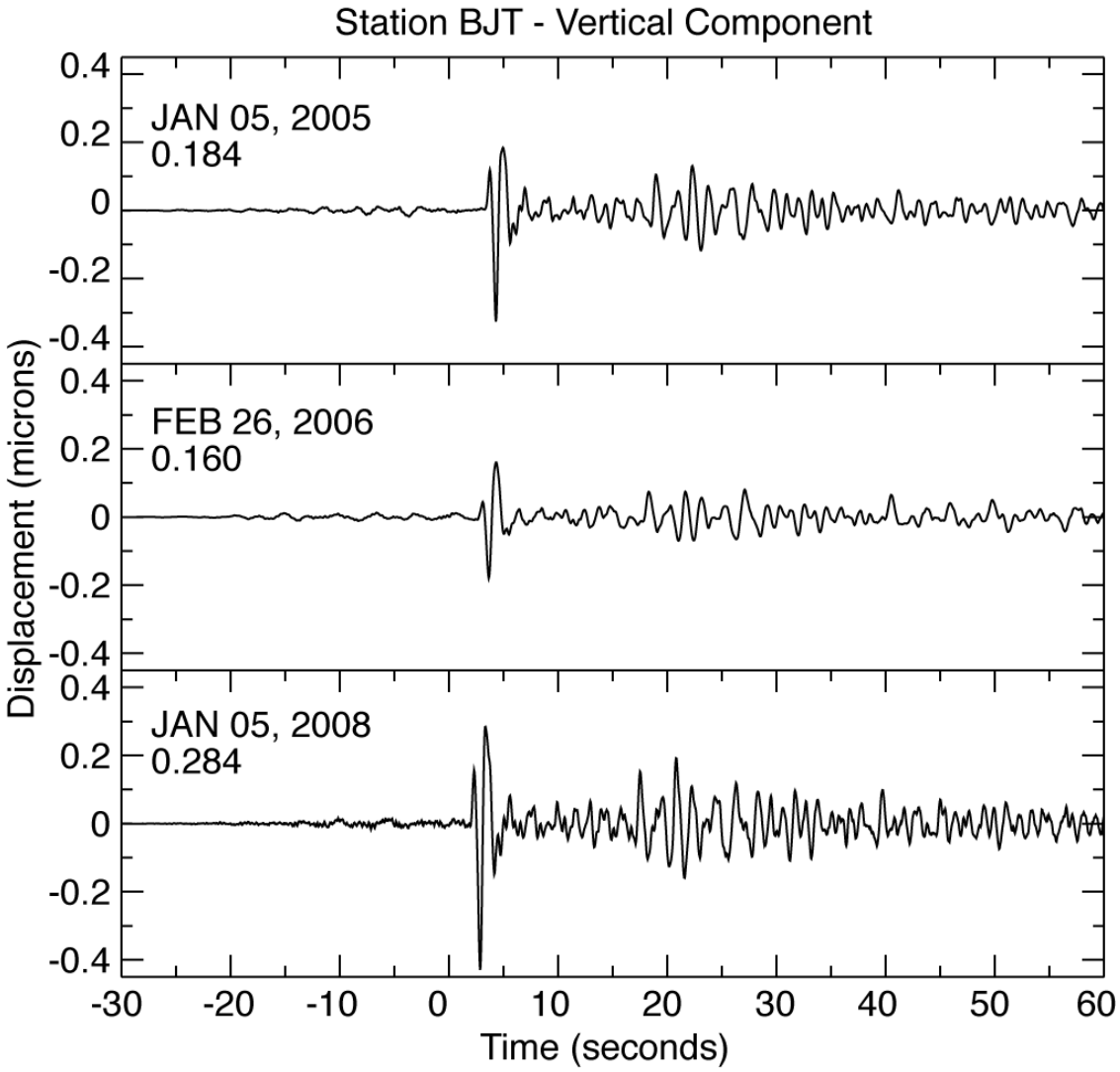

Waveforms of the vertical component for Cluster D as recorded at station BJT. Waveforms show displacement (in microns) from 30 seconds prior to the arrival of the P-wave to 60 seconds following. The date of the event is shown in the upper left corner of each waveform. The peak P-wave amplitude is recorded below the date.

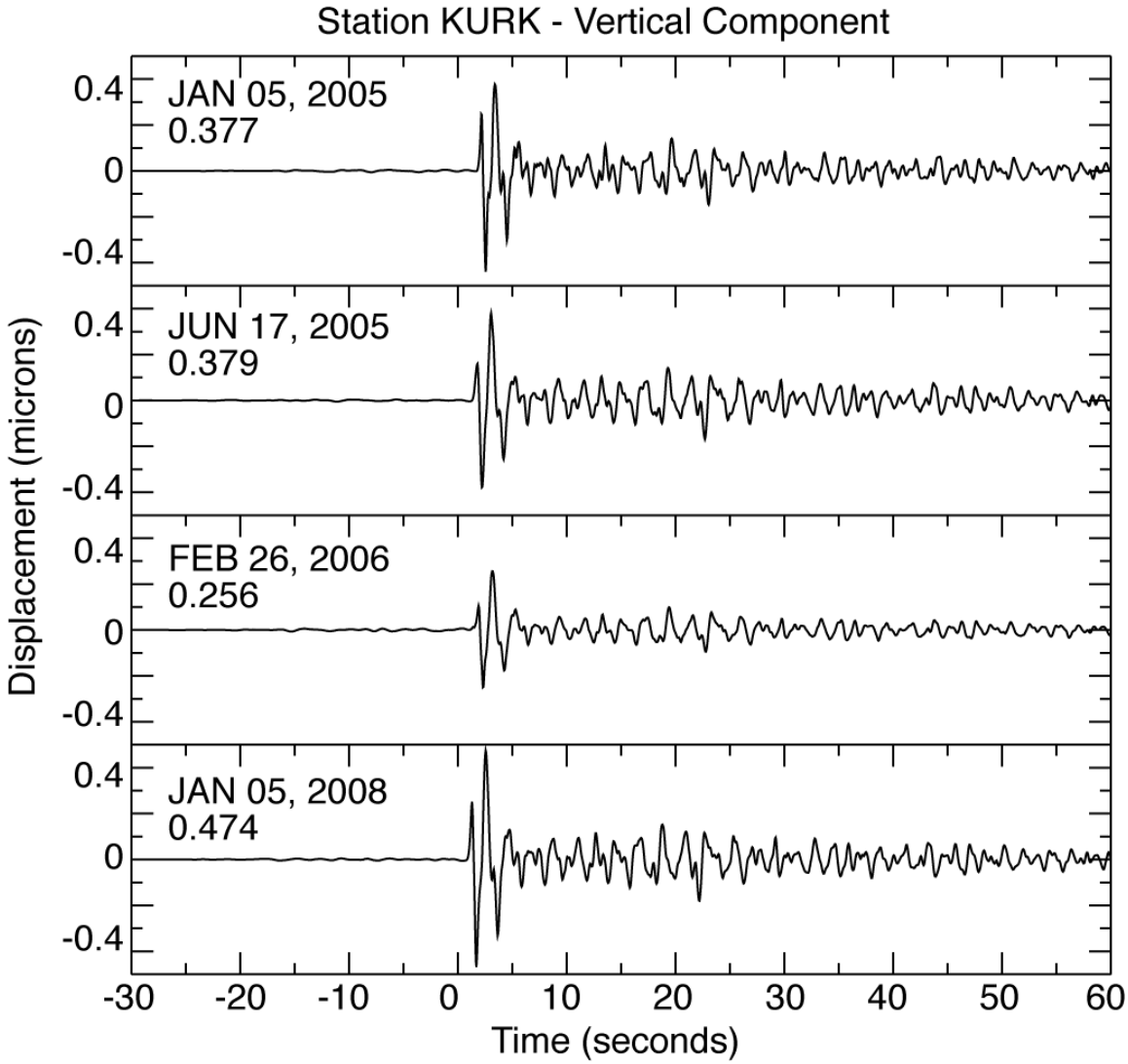

Waveforms of the vertical component for Cluster D as recorded at station KURK. Waveforms show displacement (in microns) from 30 seconds prior to the arrival of the P-wave to 60 seconds following. The date of the event is shown in the upper left corner of each waveform. The peak P-wave amplitude is recorded below the date.

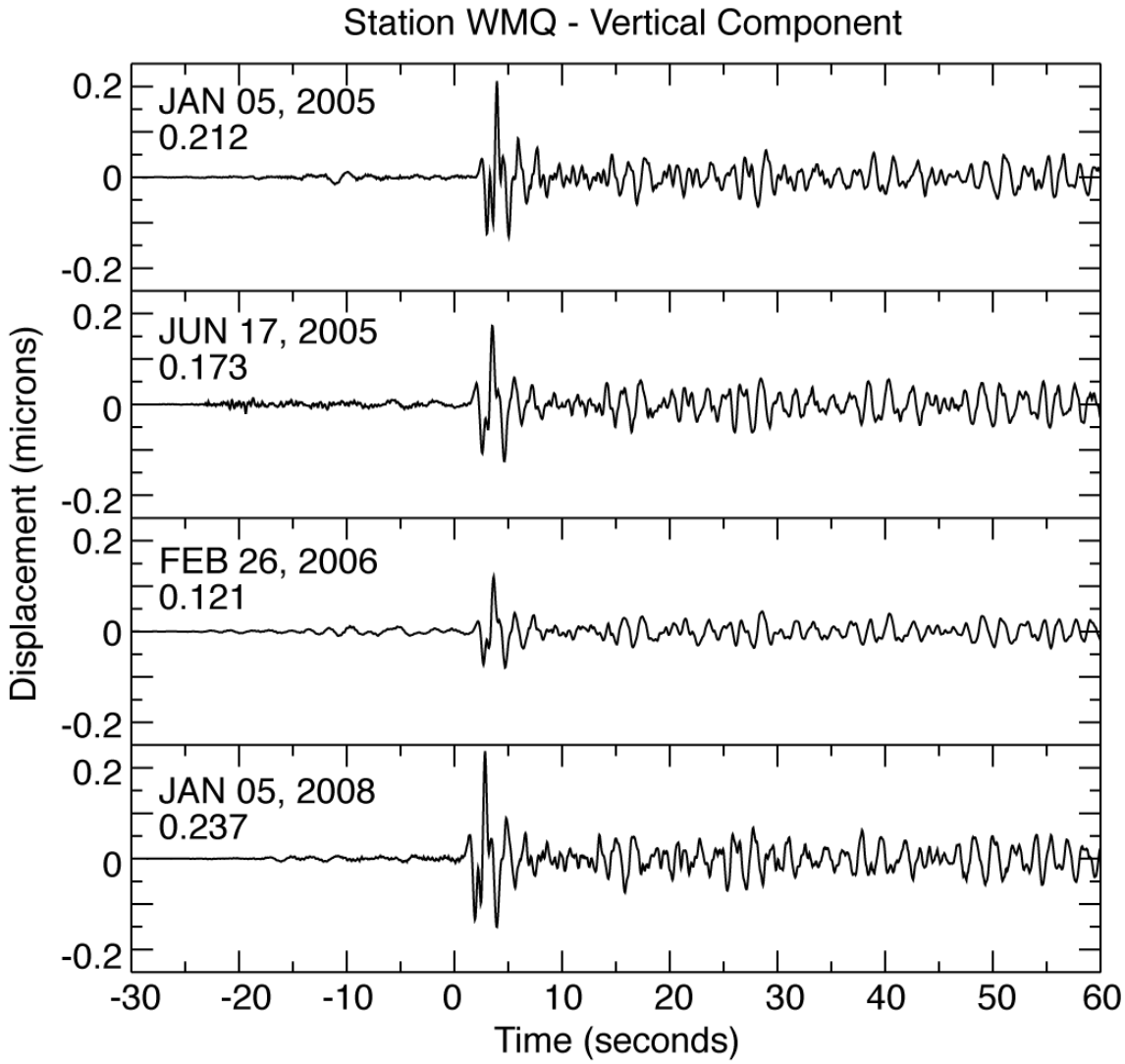

Waveforms of the vertical component for Cluster D as recorded at station WMQ. Waveforms show displacement (in microns) from 30 seconds prior to the arrival of the P-wave to 60 seconds following. The date of the event is shown in the upper left corner of each waveform. The peak P-wave amplitude is recorded below the date.

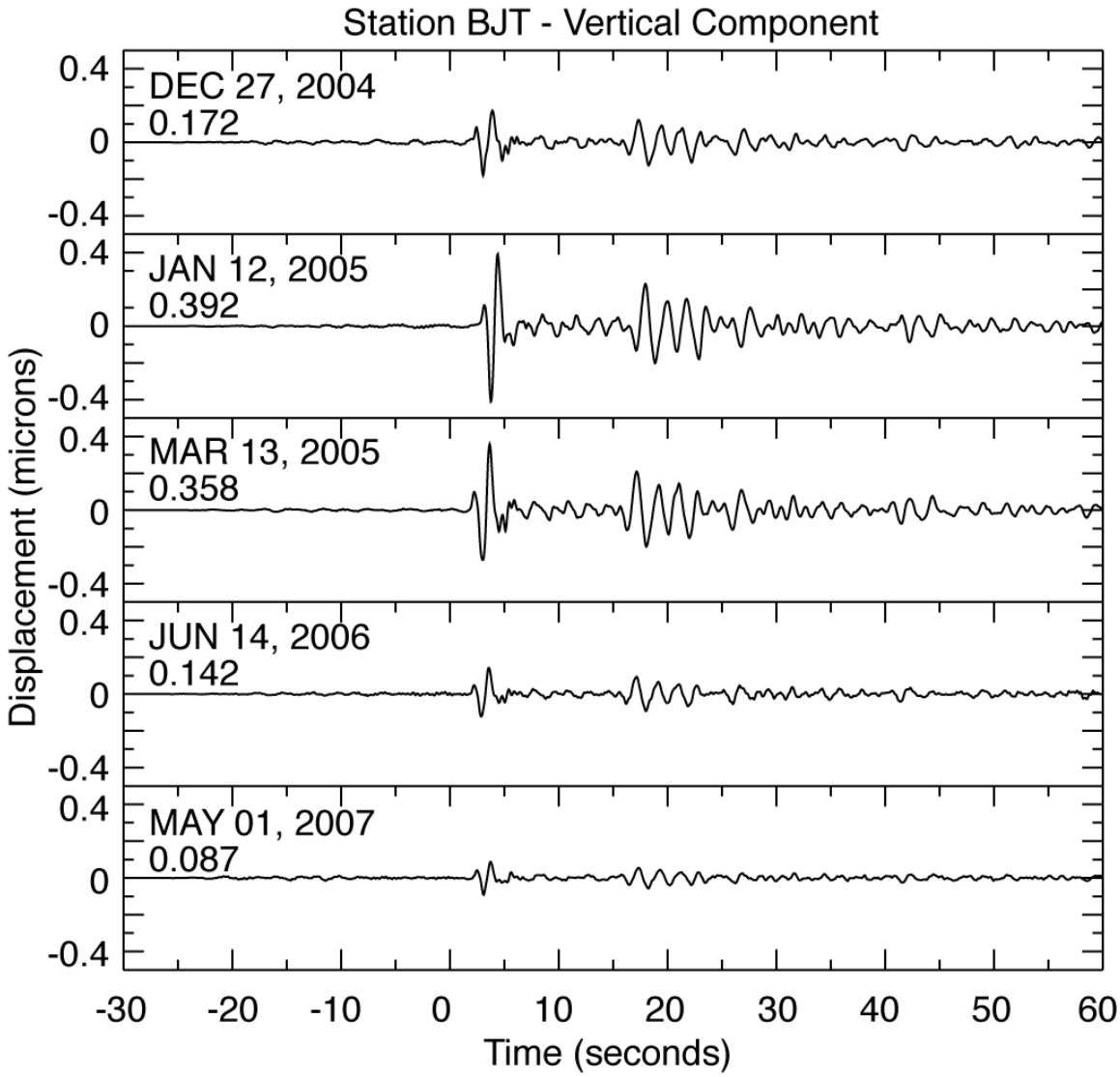

Waveforms of the vertical component for Cluster E as recorded at station BJT. Waveforms show displacement (in microns) from 30 seconds prior to the arrival of the P-wave to 60 seconds following. The date of the event is shown in the upper left corner of each waveform. The peak P-wave amplitude is recorded below the date.

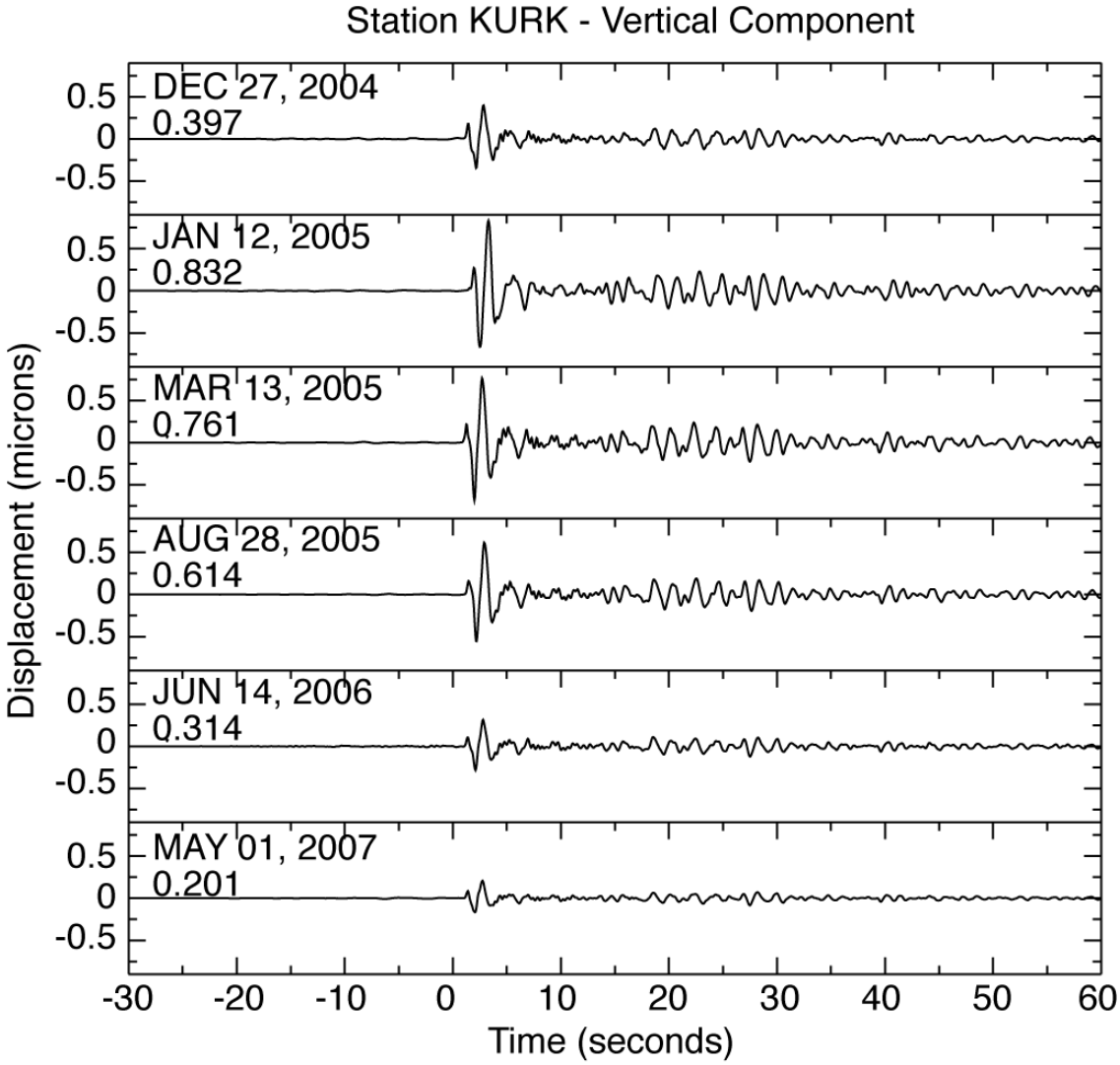

Waveforms of the vertical component for Cluster E as recorded at station KURK. Waveforms show displacement (in microns) from 30 seconds prior to the arrival of the P-wave to 60 seconds following. The date of the event is shown in the upper left corner of each waveform. The peak P-wave amplitude is recorded below the date.

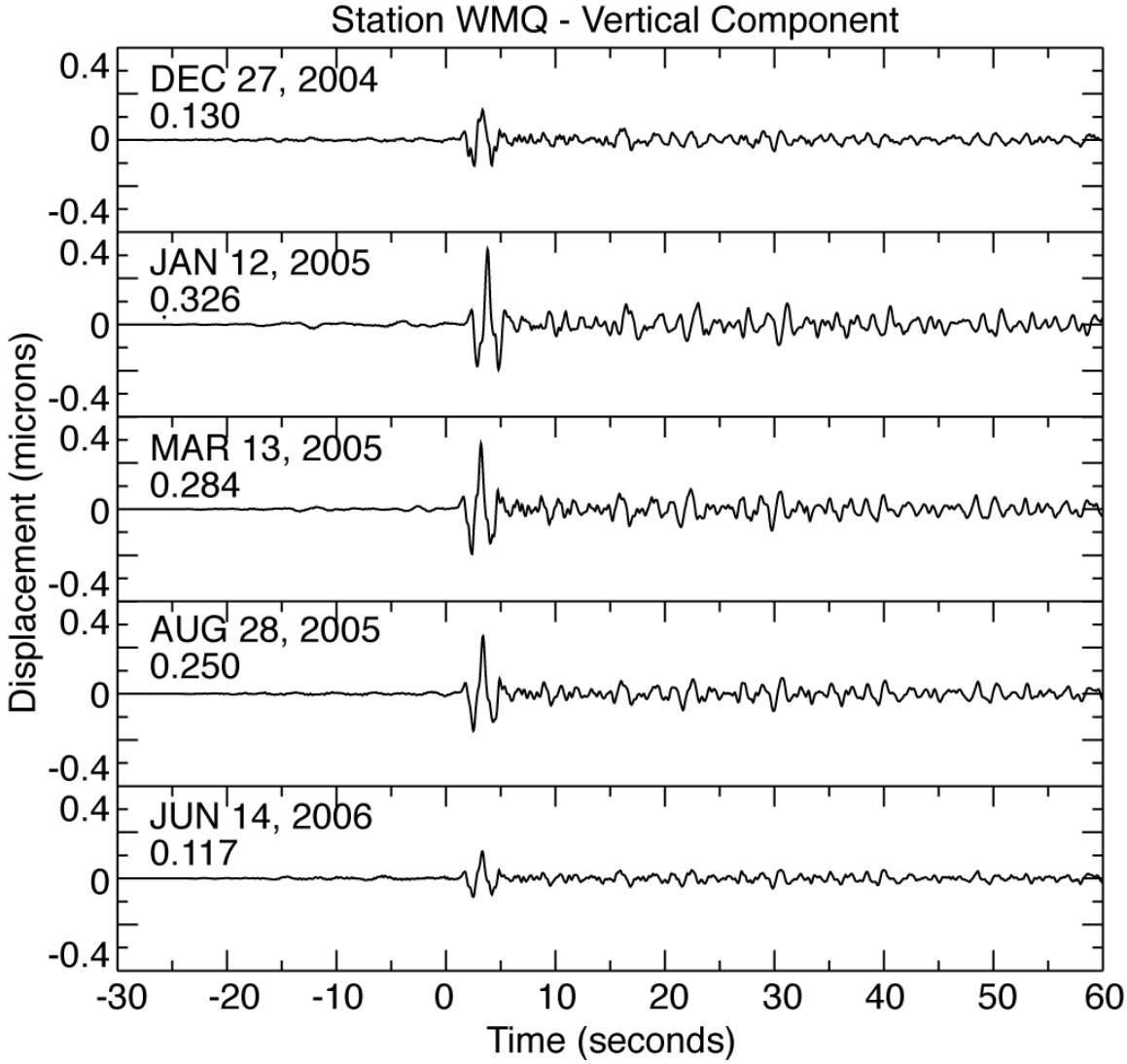

Waveforms of the vertical component for Cluster E as recorded at station WMQ. Waveforms show displacement (in microns) from 30 seconds prior to the arrival of the P-wave to 60 seconds following. The date of the event is shown in the upper left corner of each waveform. The peak P-wave amplitude is recorded below the date.

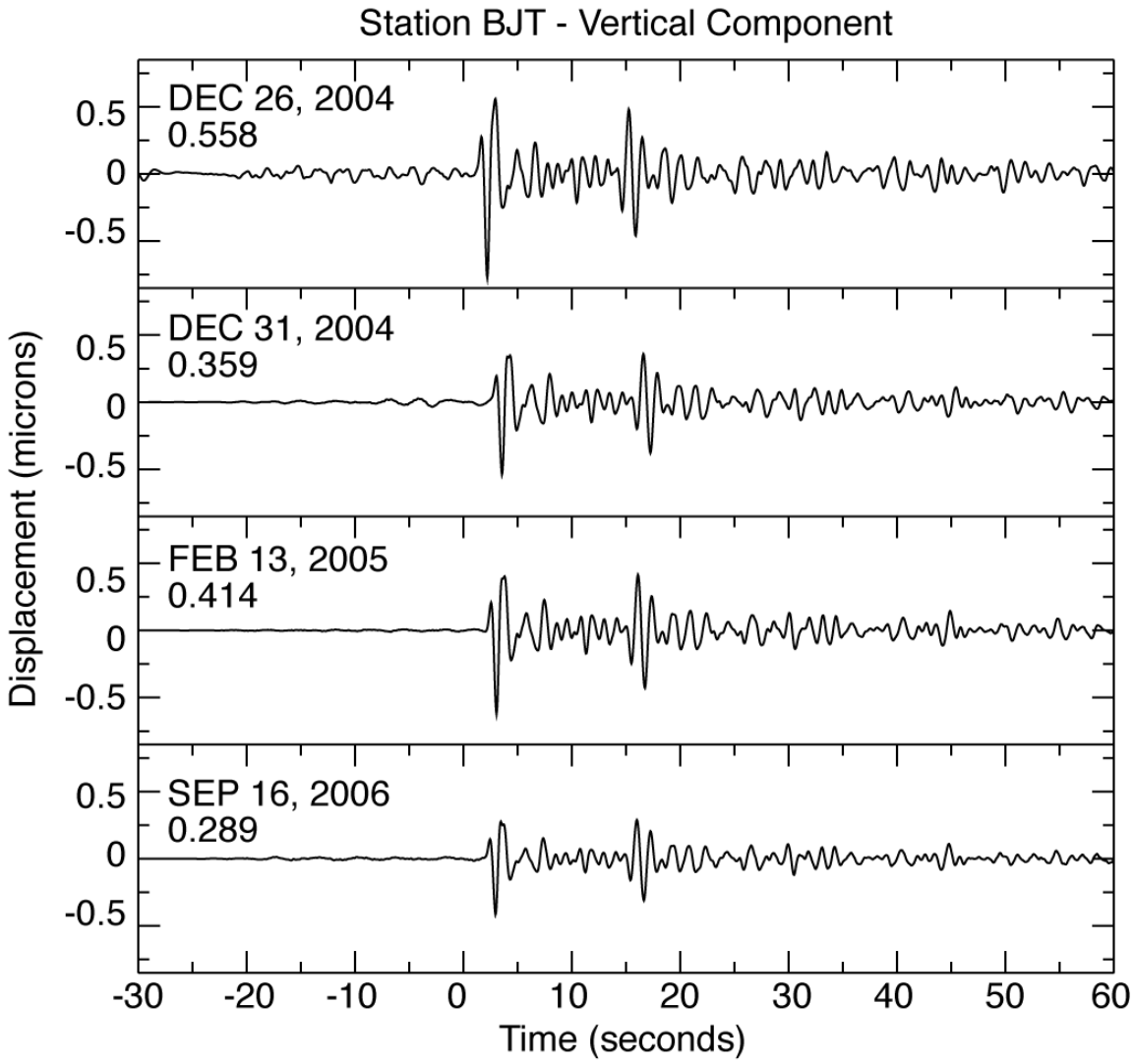

Waveforms of the vertical component for Cluster F as recorded at station BJT. Waveforms show displacement (in microns) from 30 seconds prior to the arrival of the P-wave to 60 seconds following. The date of the event is shown in the upper left corner of each waveform. The peak P-wave amplitude is recorded below the date.

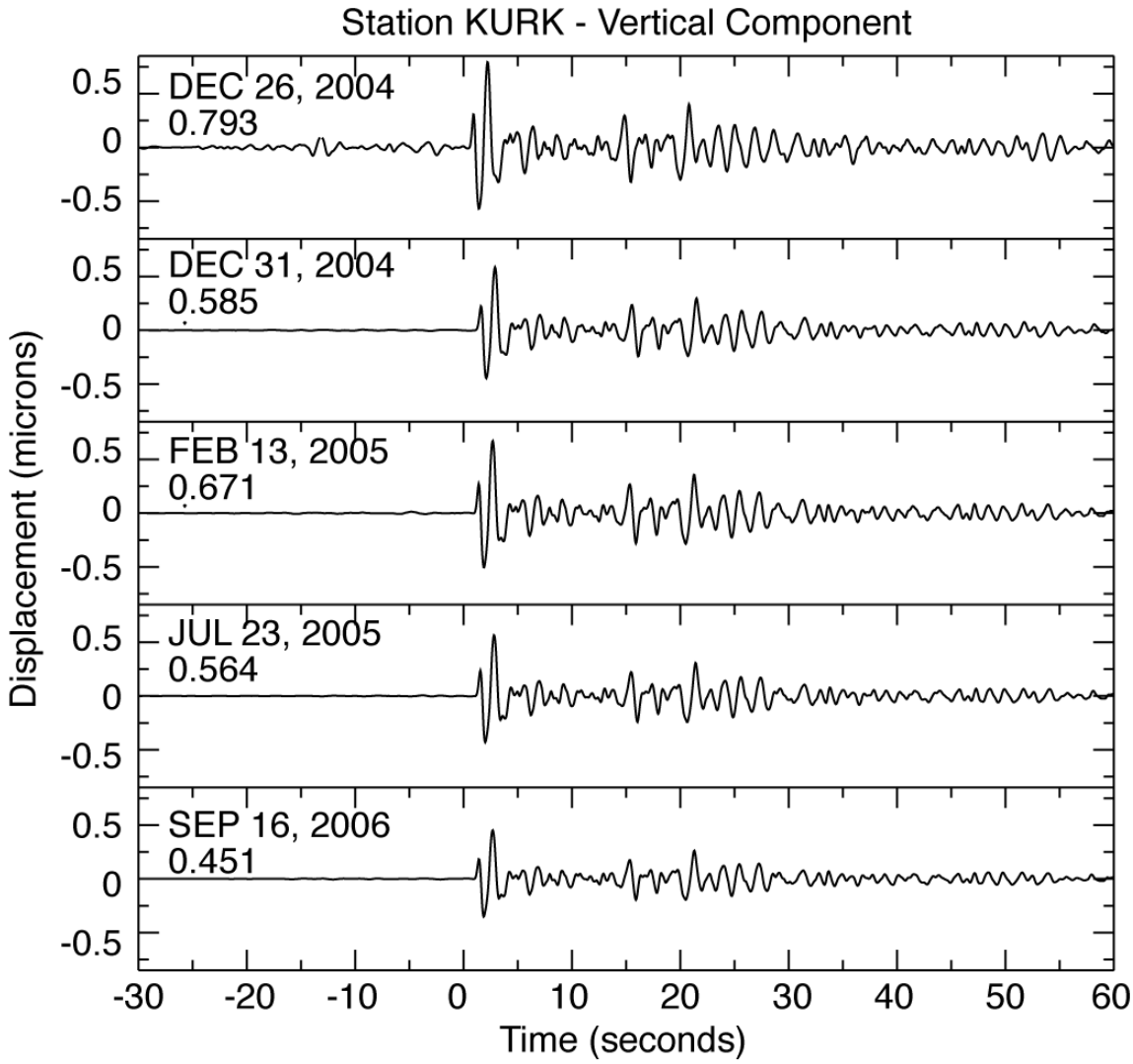

Waveforms of the vertical component for Cluster F as recorded at station KURK. Waveforms show displacement (in microns) from 30 seconds prior to the arrival of the P-wave to 60 seconds following. The date of the event is shown in the upper left corner of each waveform. The peak P-wave amplitude is recorded below the date.

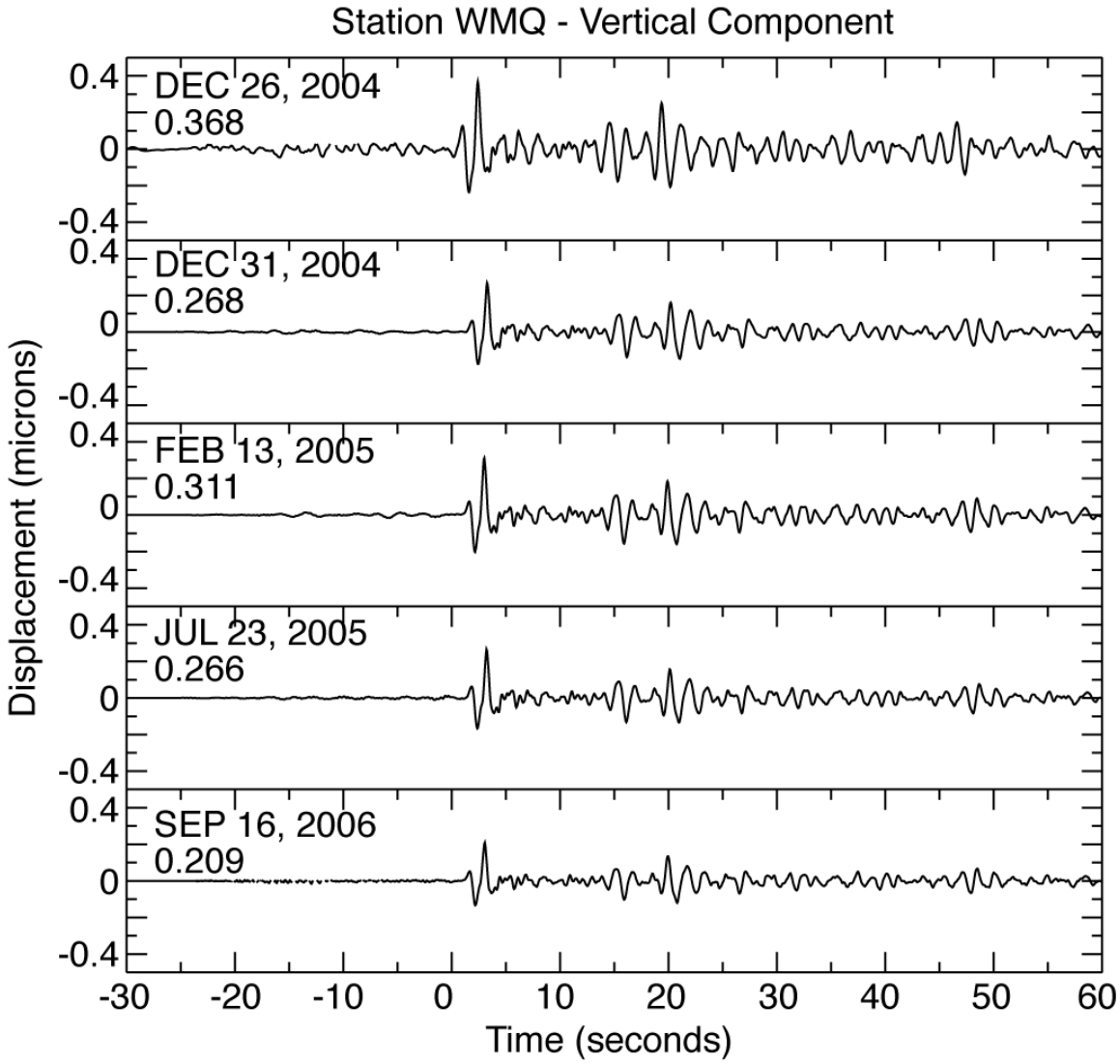

Waveforms of the vertical component for Cluster F as recorded at station WMQ. Waveforms show displacement (in microns) from 30 seconds prior to the arrival of the P-wave to 60 seconds following. The date of the event is shown in the upper left corner of each waveform. The peak P-wave amplitude is recorded below the date.

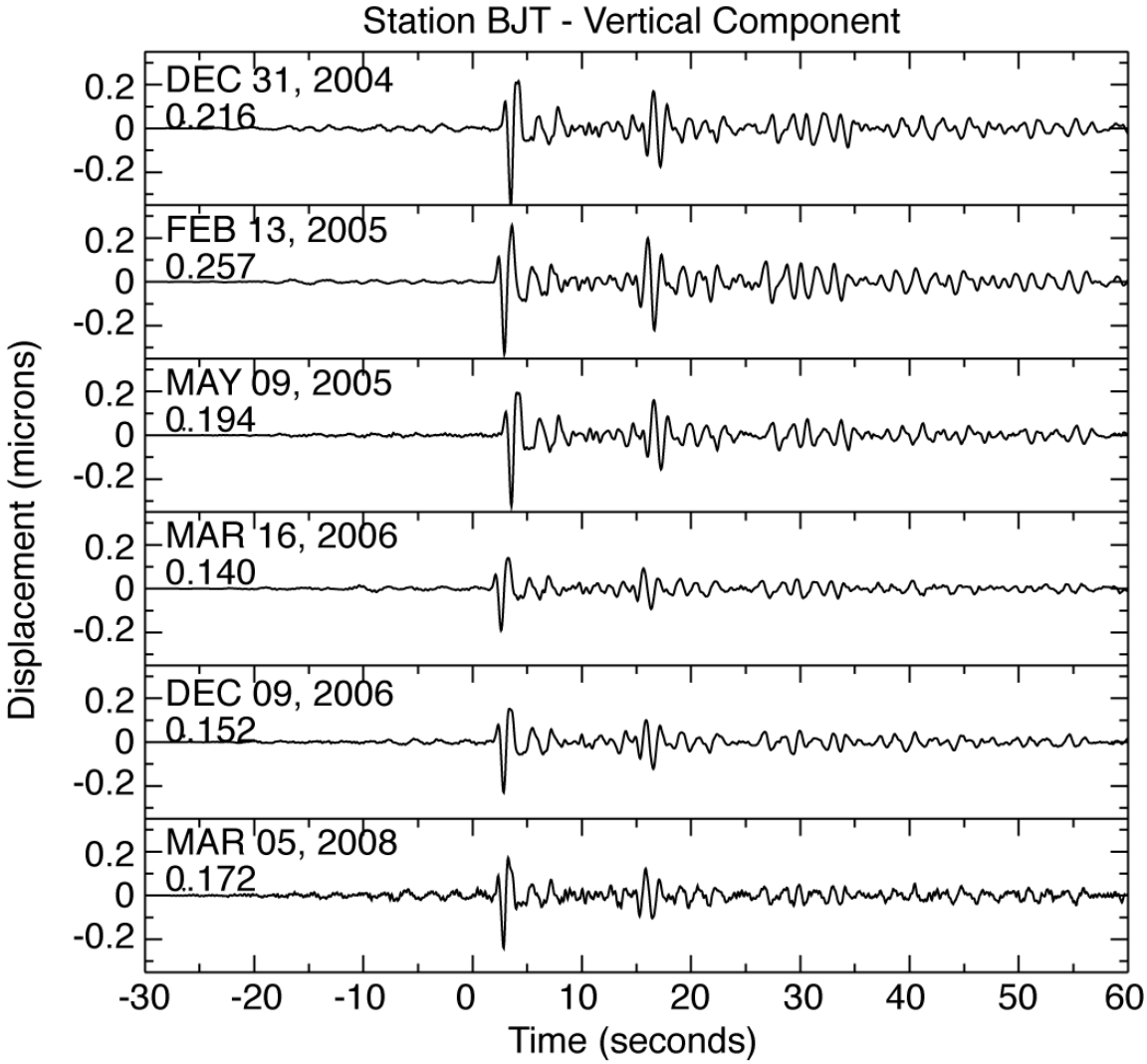

Waveforms of the vertical component for Cluster G as recorded at station BJT. Waveforms show displacement (in microns) from 30 seconds prior to the arrival of the P-wave to 60 seconds following. The date of the event is shown in the upper left corner of each waveform. The peak P-wave amplitude is recorded below the date.

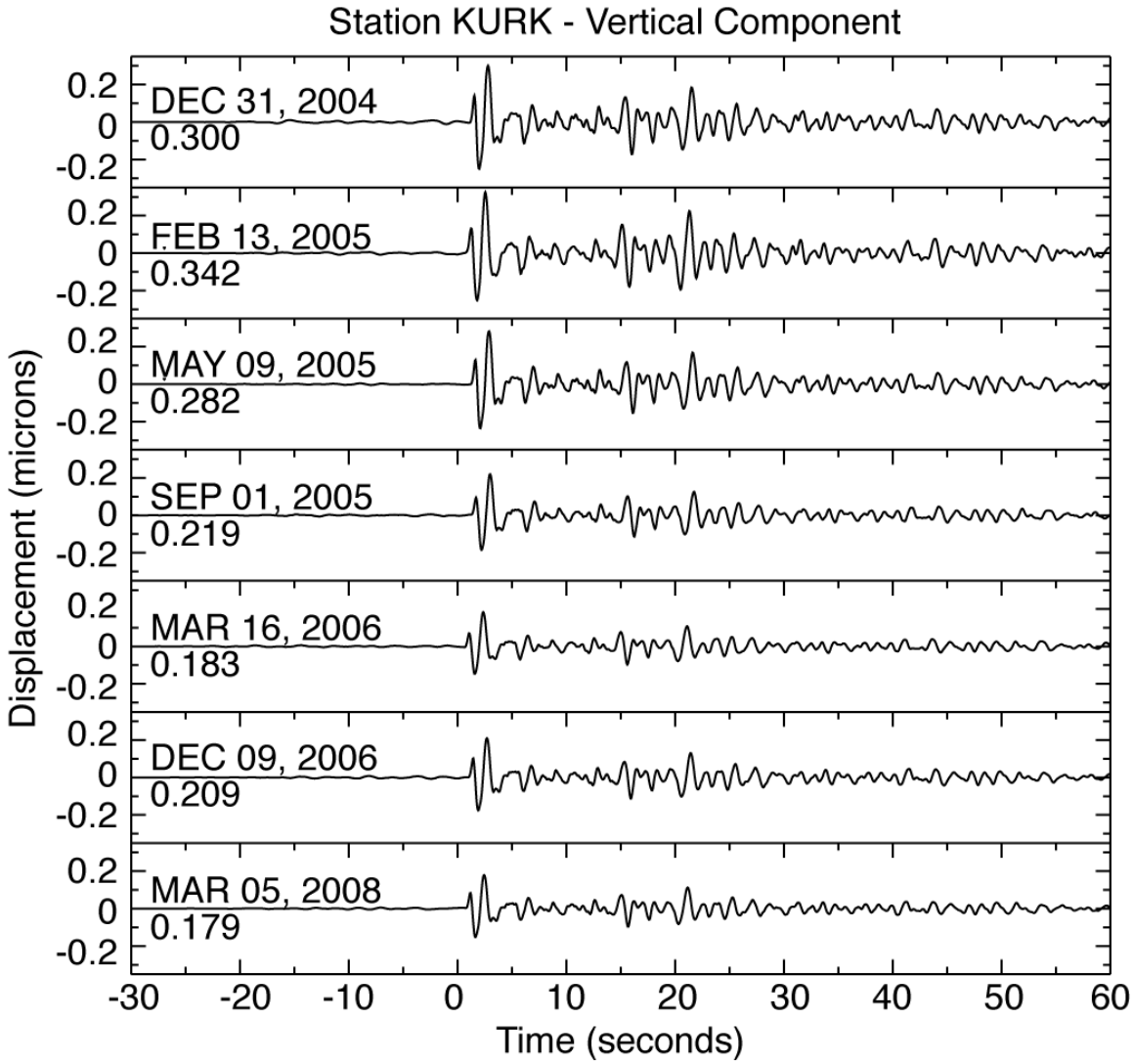

Waveforms of the vertical component for Cluster G as recorded at station KURK. Waveforms show displacement (in microns) from 30 seconds prior to the arrival of the P-wave to 60 seconds following. The date of the event is shown in the upper left corner of each waveform. The peak P-wave amplitude is recorded below the date.

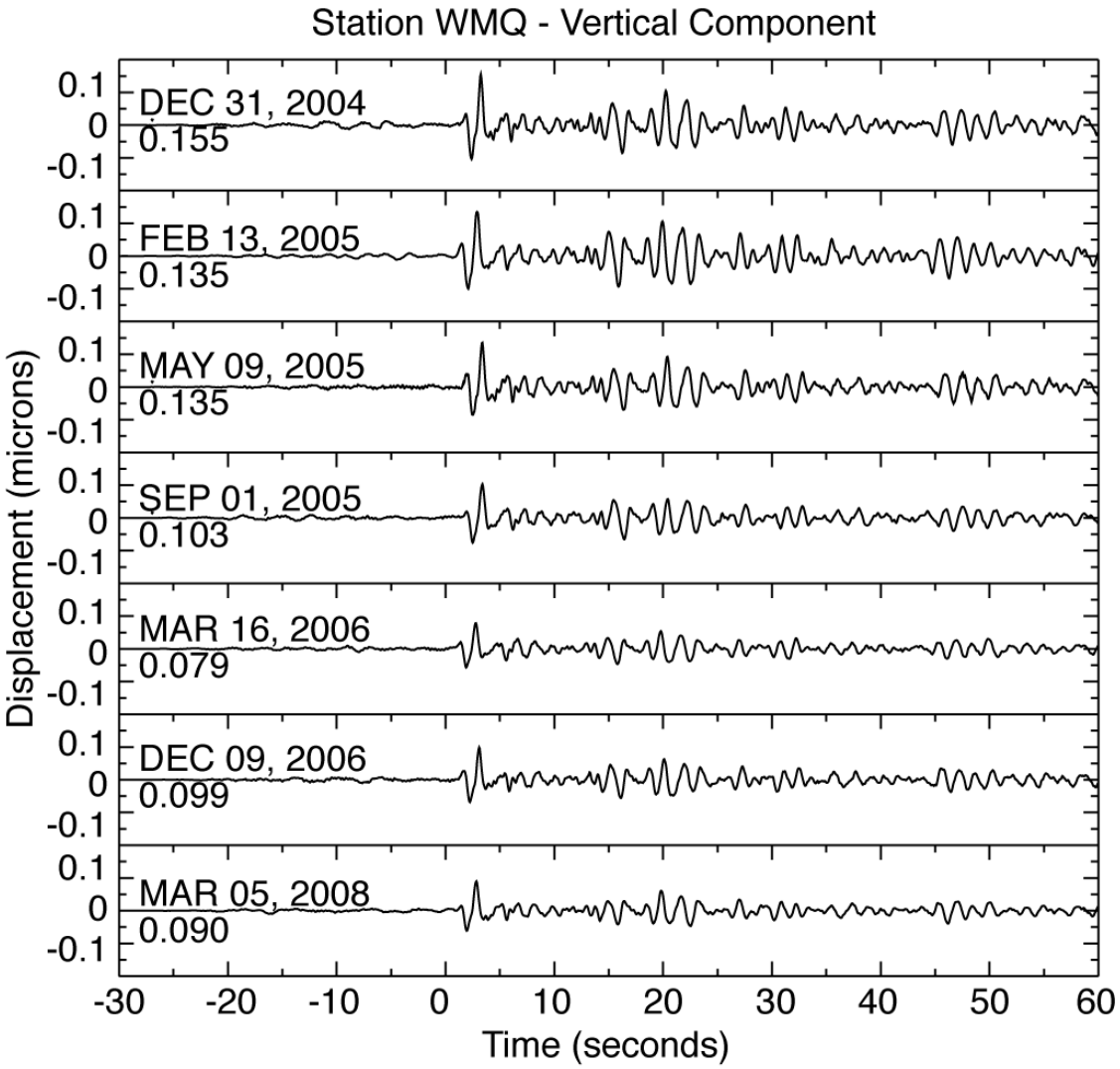

Waveforms of the vertical component for Cluster G as recorded at station WMQ. Waveforms show displacement (in microns) from 30 seconds prior to the arrival of the P-wave to 60 seconds following. The date of the event is shown in the upper left corner of each waveform. The peak P-wave amplitude is recorded below the date.

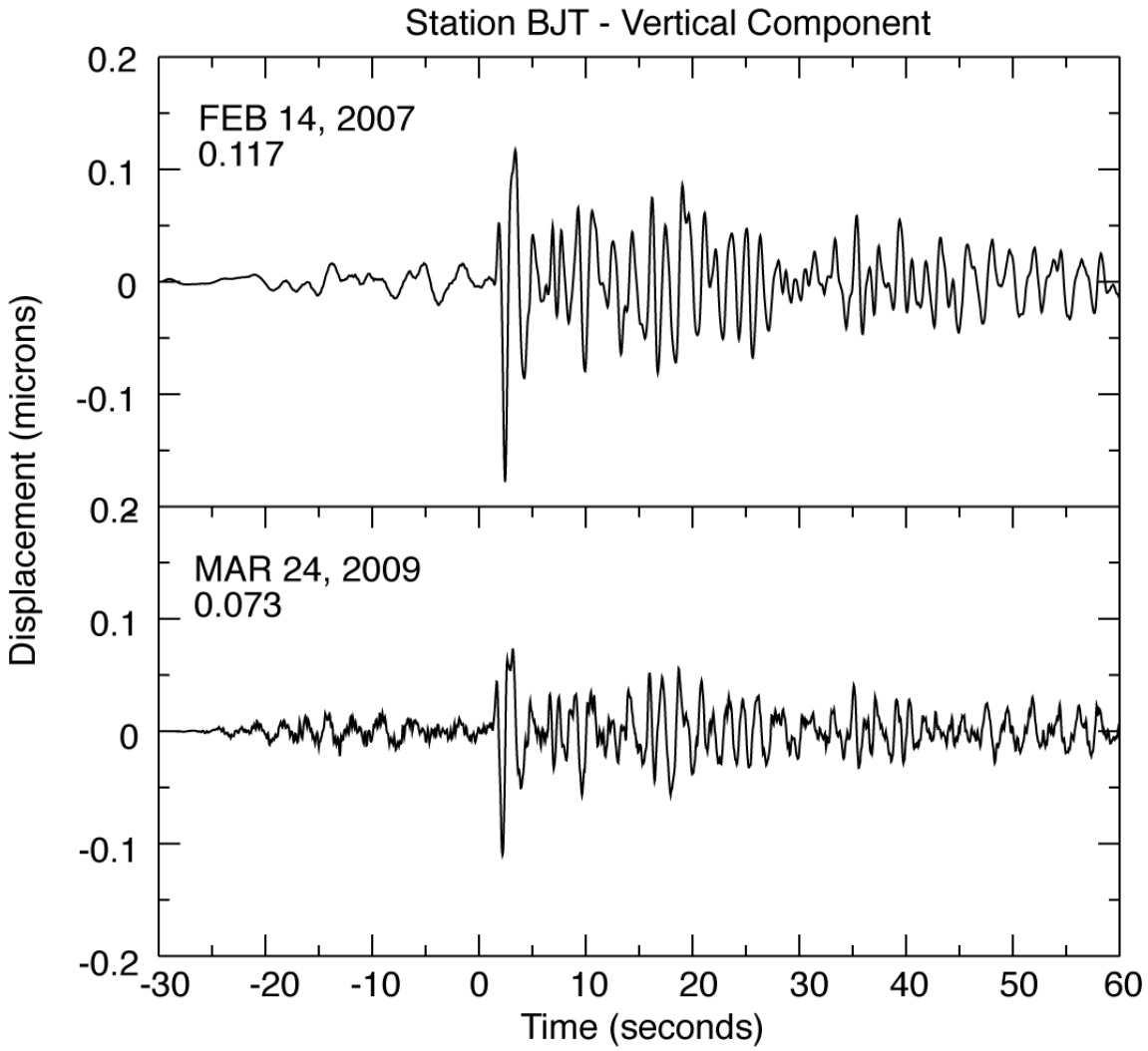

Waveforms of the vertical component for Cluster H as recorded at station BJT. Waveforms show displacement (in microns) from 30 seconds prior to the arrival of the P-wave to 60 seconds following. The date of the event is shown in the upper left corner of each waveform. The peak P-wave amplitude is recorded below the date.

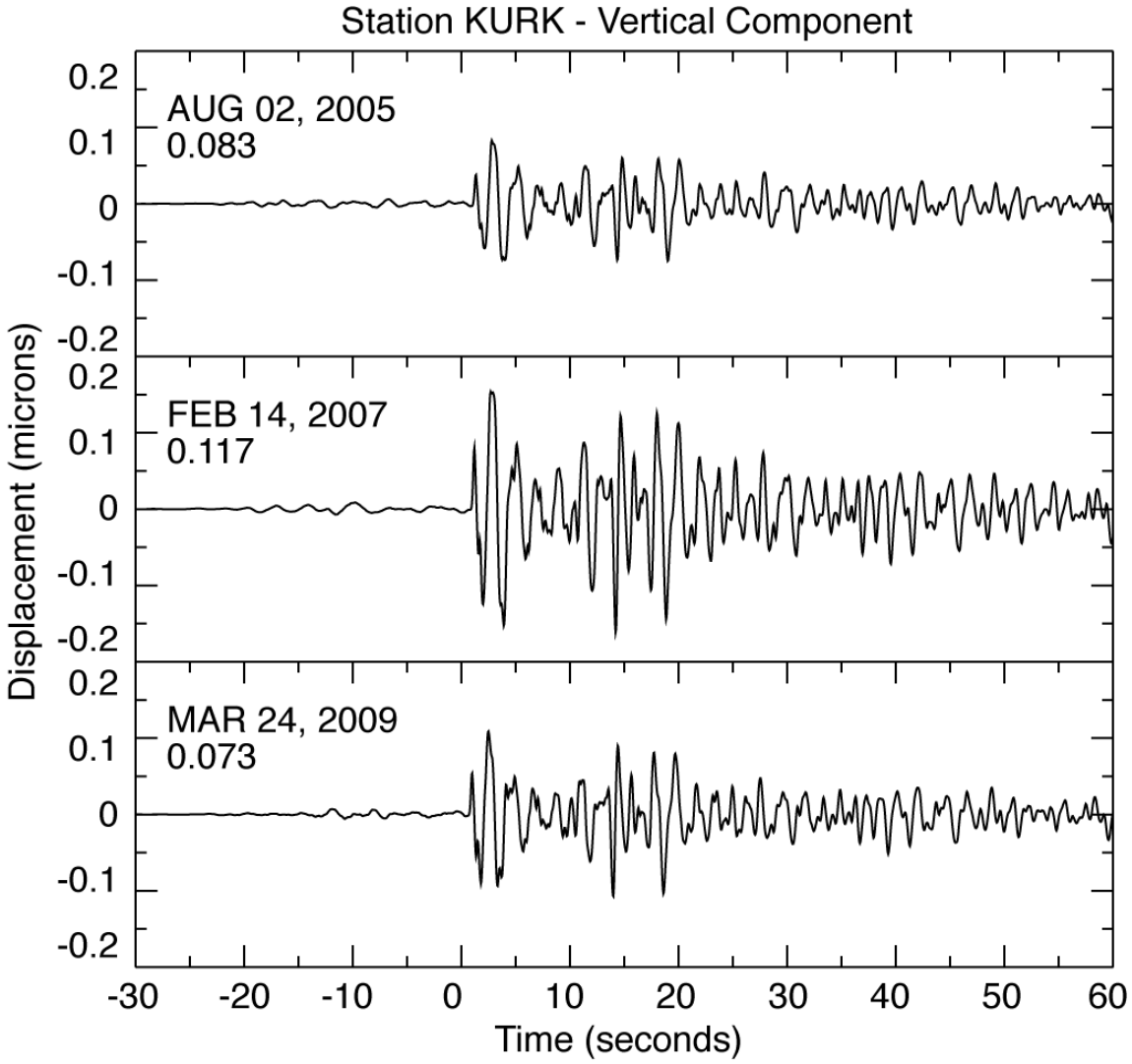

Waveforms of the vertical component for Cluster H as recorded at station KURK. Waveforms show displacement (in microns) from 30 seconds prior to the arrival of the P-wave to 60 seconds following. The date of the event is shown in the upper left corner of each waveform. The peak P-wave amplitude is recorded below the date.

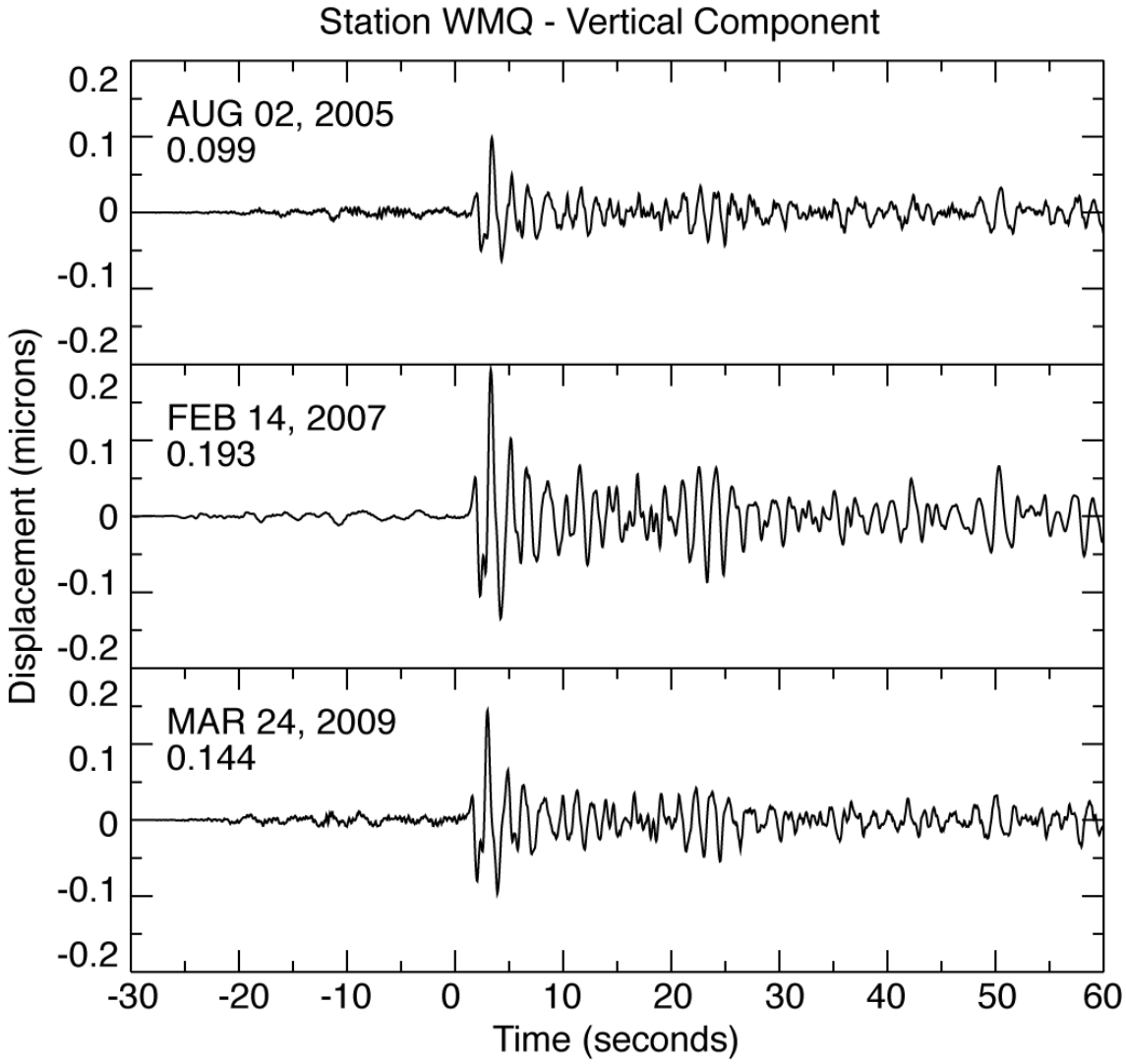

Waveforms of the vertical component for Cluster H as recorded at station WMQ. Waveforms show displacement (in microns) from 30 seconds prior to the arrival of the P-wave to 60 seconds following. The date of the event is shown in the upper left corner of each waveform. The peak P-wave amplitude is recorded below the date.

Appendix C: Summary of Slip Model Results

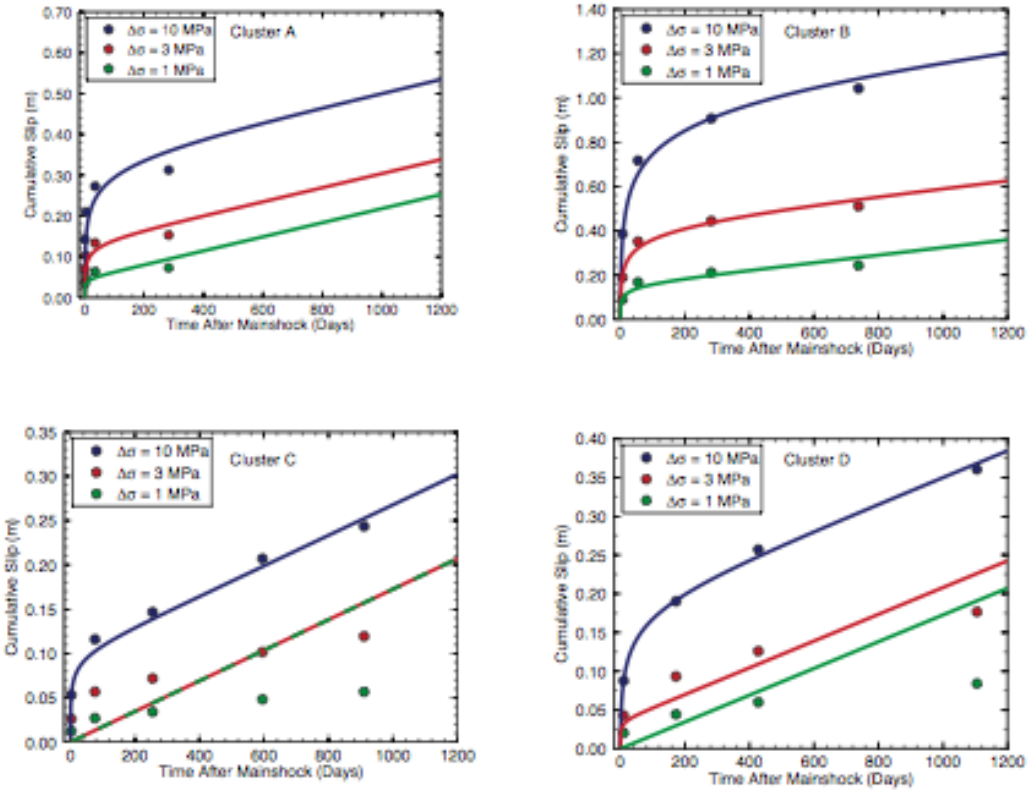

A summary of slip modeling results for clusters A, B, C, and D. We vary the relaxation time (t_r) and velocity (V_+) to model the results of a 1 MPa, 3 MPa, and 10 MPa stress drop to fit the calculated slip. The majority of clusters show the best fit for a large stress drop.

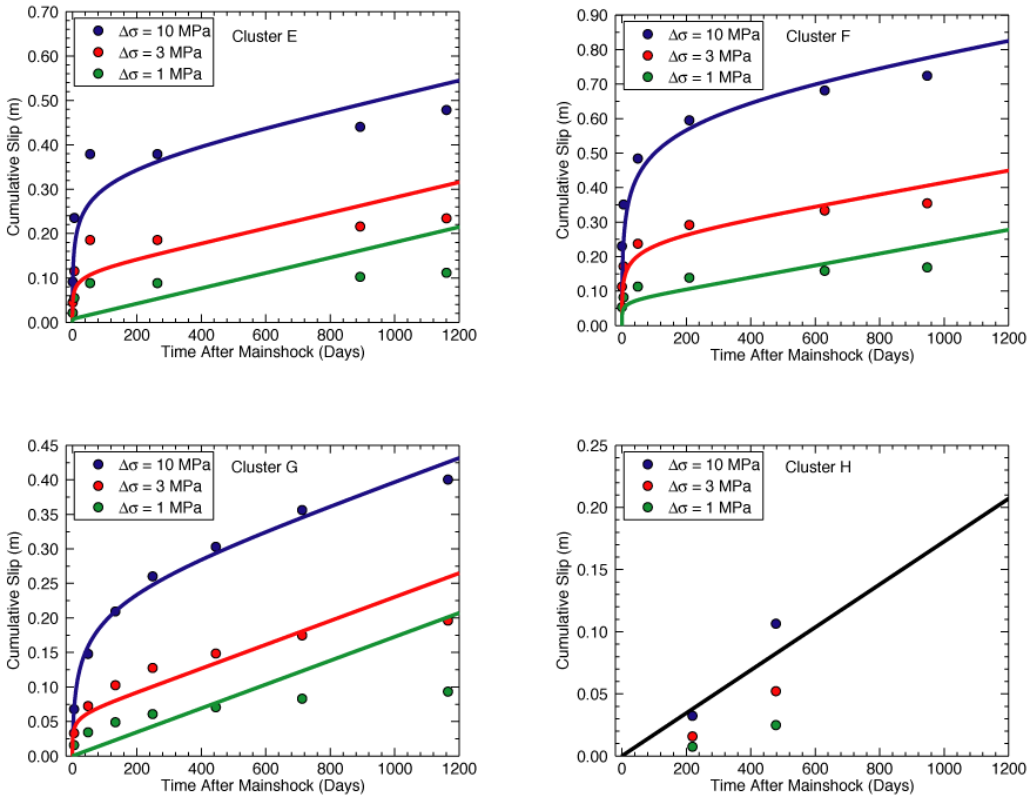

A summary of slip modeling results for clusters E, F, G, and H. We vary the relaxation time (t_r) and velocity (V_+) to model the results of a 1 MPa, 3 MPa, and 10 MPa stress drop to fit the calculated slip. The majority of clusters show the best fit for a large stress drop.